Forschungszentrum Jülich
in der Helmholtz-Gemeinschaft

Self-assembly and Local Functionality at Au/Electrolyte Interfaces: An in situ Scanning Tunneling Microscopy Approach

Zhihai Li

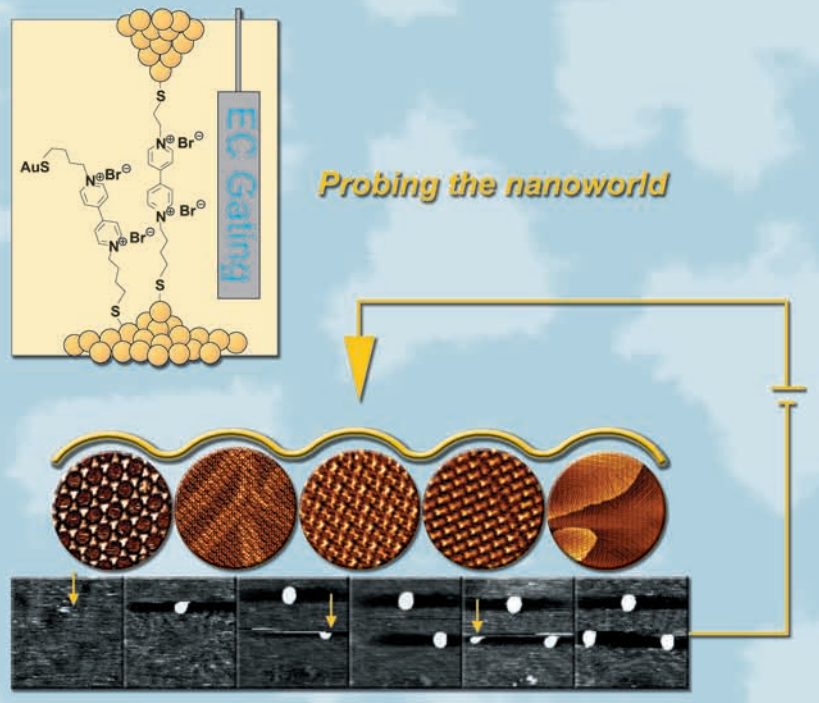

Informationstechnik
Information Technology

Schriften des Forschungszentrums Jülich
Reihe Informationstechnik / Information Technology Band / Volume 16

Forschungszentrum Jülich GmbH
Institut für Bio- und Nanotechnologie (IBN)
Grenz- und Oberflächen (IBN-3)

Self-assembly and Local Functionality at Au/Electrolyte Interfaces: An in situ Scanning Tunneling Microscopy Approach

Zhihai Li

Schriften des Forschungszentrums Jülich
Reihe Informationstechnik / Information Technology Band / Volume 16

ISSN 1433-5514 ISBN 978-3-89336-482-4

Bibliographic information published by the Deutsche Nationalbibliothek.
The Deutsche Nationalbibliothek lists this publication in the Deutsche Nationalbibliografie; detailed bibliographic data are available in the Internet at http://dnb.d-nb.de.

Publisher and Distributor:	Forschungszentrum Jülich GmbH Zentralbibliothek, Verlag D-52425 Jülich Telefon (02461) 61-5368 · Telefax (02461) 61-6103 e-mail: zb-publikation@fz-juelich.de Internet: http://www.fz-juelich.de/zb
Cover Design:	Grafische Medien, Forschungszentrum Jülich GmbH
Printer:	Grafische Medien, Forschungszentrum Jülich GmbH
Copyright:	Forschungszentrum Jülich 2007

Schriften des Forschungszentrums Jülich
Reihe Informationstechnik / Information Technology Band / Volume 16

D 82 (Diss., Aachen, RWTH, 2007)

ISSN 1433-5514
ISBN 978-3-89336-482-4

The complete volume is freely available on the Internet on the Jülicher Open Access Server (JUWEL) at http://www.fz-juelich.de/zb/juwel

This dissertation is dedicated to my affectionate mom, Gui-xiang Feng,
who left us on 10 January 2007…

Abstract

The integration of molecular structures in electronic circuits is currently an active field of fundamental research inspired by the visionary concepts of molecule-based electronics. The bottom-up approach, based on the self-assembly of functional molecular building blocks into more complex architectures, represents an attractive alternative to silicon-based nanoelectronics. Basic concepts and strategies of two-dimensional self-assembly and electron transport in tailored nanostructures can be also addressed and explored at electrified solid/liquid interfaces employing the electrolyte as an “electrochemical gate”.

In this dissertation, we applied electrochemical Scanning Tunneling Microscopy and Spectroscopy (STM and STS) in combination with Cyclic Voltammetry (CV) and Surface Enhanced Infrared Reflection Absorption Spectroscopy (SEIRAS) to investigated the two-dimensional (2D) assembly of aromatic carboxylic acids triggered by directional hydrogen bond and substrate–adsorbate coordination, and structure as well as electron transfer properties of redox-active thioalkylviologen derivatives at electrified gold/aqueous electrolyte interfaces.

First, the steady state and kinetic processes of self-assembled adlayers of carboxylic acids were investigated on Au(111)/electrolyte interfaces. The target molecules include trimesic acid (TMA), isophthalic acid (IA), terephthalic acid (TA) and benzoic acid (BA). Five distinctly different 2D self-assembled nanostructures of TMA were created by tuning the applied electrode potential. The properties of these adlayers have been elucidated at the molecular level by in situ STM. Four different ordered adlayers of planar-oriented molecules, which are labeled as honeycomb structures, a ribbon-type phase, a herringbone-type phase and hydrogen-bonded dimers were found in the potential range $-0.250\ V \leq E \leq 0.400\ V$, i.e. at an uncharged or slightly negatively charged Au(111) electrode. The structure transitions are in all cases triggered by increasing the electrode potential.

Further increase of the electrode potential to positive charge densities, i.e. $E > 0.400\ V$, causes an orientation change from planar to upright. An initially disordered

phase transforms into an ordered, stripe-like chemisorbed adlayer of perpendicularly oriented TMA molecules. The structure models were proposed on the basis of the analysis of the STM contrast images, the comparison with crystallographic data and molecular modeling. The steady state investigations were combined with time-resolved studies revealing molecular-level details of the potential-induced phase transitions between the various types of molecular adlayers.

The work on supramolecular nanostructures of self-assembled carboxylic acids has been extended to the TMA-related molecules IA, TA and BA. These molecules are constituted of a central phenyl ring and a different number of carboxylic acid groups. These comparative studies revealed the structure-determining role of intermolecular hydrogen bond. IA and TA form hydrogen-bonded zigzag and one-dimensional linear tapes characterized by a central hydrogen-bonded dimer motif of the carboxylic groups. BA assembles into molecular tetramers. All three molecules exhibit a potential-induced structure transition at a positively charged electrode, where the molecular orientation changes from planar to vertical or tilted. This conclusion is supported by complementary infrared spectroscopic investigations.

The second part of the work is focused on the self-assembly and redox-properties of immobilized adlayers of various viologen derivatives (N-alkyl-N'-(n-thioalkyl)-4,4'-bipyridinium bromide (HS-nVn-H) and N,N'-bis(n-thioalkyl)-4,4'-bipyridinium bromide (HS-nVn-SH), n = 5, 6, 7, 8, 10) on Au(111)-(1x1) electrodes. The fabricated adlayers exhibit two characteristic one-electron redox processes ($V^{2+} \leftrightarrow V^{\bullet+}$, $V^{\bullet+} \leftrightarrow V^{0}$), which were characterized by cyclic voltammetry. In situ STM has been employed to investigate the structural details of the monomolecular redox-active, viologen-based adlayers, and three types of viologen adlayers were discovered for all target molecules: a low-coverage disordered and an ordered striped phase of flat-oriented molecules as well as a high-coverage monolayer of tilted molecules. The unit cells of the different molecular adlayers are rectangular with a constant short distance of 0.5 nm and a long distance increasing 0.2885 nm per CH_2-unit. The organic adlayers appear to be in registry with the substrate surface.

An in situ STM configuration was employed to explore electron transport properties of single molecular junctions Au(T) │ HS-nVn-SH(HS-nVn-H) │ Au(S). The observed sigmoidal potential dependence of the molecular conductance, measured at

variable substrate potential E_S and at small and constant bias voltage ($E_T - E_S$), was attributed to electronic structure changes of the viologen moiety during the one-electron reduction/re-oxidation process $V^{2+} \leftrightarrow V^{\bullet+}$. The tunneling experiment (current–overpotential spectroscopy) in STM-based junctions Au(S)-S-6V6-H ┃ Au(T) revealed current–voltage curves with a maximum located at the equilibrium potential of the redox-process $V^{2+} \leftrightarrow V^{\bullet+}$. The second type of tunneling experiment (tunneling current–bias spectroscopy) showed a diode-like tunneling response with an on/off ratio ≥ 70. The tunneling resonance characteristics of the viologen-modified junction were tentatively attributed to a sequential two-step electron transfer mechanism.

Abstrakt

Die Integration molekularer Strukturen in elektronische Schaltkreise, inspiriert durch die visionären Konzepte einer Molekül-basierenden Elektronik, ist ein aktives Gebiet der modernen Grundlagenforschung. Bottom-up Konzepte basierend auf der Selbstorganisation funktionaler molekularer Bausteine in komplexere Architekturen, repräsentieren eine attraktive Alternative zu einer Silizium - basierenden Nano-elektronik. Grundlegende Konzepte und Strategien der zweidimensionalen Selbst-organisation sowie des Ladungstransportes in maßgeschneiderten Nanostrukturen können auch an elektrochemischen fest/flüssig Grenzflächen adressiert werden. Von besonderem Interesse ist in dieser Konfiguration die Rolle des Elektrolyten als „electrochemical gate".

In der vorliegenden Dissertationsschrift werden funktionale Adsorbatschichten an einer Au(111)/Elektrolyt Grenzfläche mittels in-situ Rastertunnelmikroskopie (RTM) und –spektroskopie (RTS) in Kombination mit zyklischer Voltammetrie und oberflächenverstärkter Infrarotspektroskopie (SEIRAS) studiert. Ein erstes Themengebiet beinhaltet Untersuchungen zur zweidimensionalen Selbstorganisation aromatischer Carbonsäuren mit Fokus auf die Interaktion direktionaler Wasserstoffbrückenbindungen und Substrat - Adsorbat Koordination. Ein zweites Themengebiet beinhaltet experimentelle Arbeiten zum Ladungstransport mit redoxaktiven Thioalkylviologen - Derivaten.

Die „steady state" und dynamischen Eigenschaften von selbstorganisierten Adsorbatschichten von Carbonsäuren wurden an der Grenzfläche Au(111)/wässriger Elektrolyt studiert. Die Targetmoleküle waren Trimesinsäure (TMA), Isophthalsäure (IB), Terephthalsäure (TA) und Benzoesäure (BA). TMA Moleküle organisieren sich auf einer Au(111) - Oberfläche, abhängig vom angelegten Elektrodenpotential, in fünf unterschiedlichen, 2D - geordneten Adsorbatschichten. Die Eigenschaften dieser Adsorbatschichten wurden mittels in situ RTM mit molekularer Auflösung charakterisiert. Im Potentialbereich $-0.250\ V \leq E \leq 0.400\ V$, d.h. an einer ungeladenen bzw. schwach negativ geladenen Goldoberfläche, konnten vier 2D - geordnete Schichten planar orientierter Moleküle gefunden werden, welche in der vorliegenden

Arbeit als Honigwabenstruktur, Bänderstruktur, Herringgrätenstruktur bzw. zweidimensionale Wasserstoffbrücken - verbrückte Dimerstruktur bezeichnet werden.

Die Erhöhung des Elektrodenpotentials zu positiven Ladungsdichten, d.h. E > 0.400 V, führt zu einem Orientierungswechsel von planar zu senkrecht. Eine zunächst ungeordnete Metastruktur transferiert in eine geordnete chemisorbierte Streifenstruktur senkrecht orientierter TMA - Moleküle. Die vorgeschlagenen Strukturmodelle basieren auf einer Analyse der RTM Kontrastpattern, dem Vergleich mit kristallographischen Daten und molekularen Modellrechnungen. Die Geichgewichtsuntersuchungen wurden mit zeitaufgelösten Studien kombiniert, um molekulare Details von potential-indizierten Phasenübergängen zwischen den unterschiedlichen molekularen Adsorbatschichten zu erkunden.

Die Forschungsarbeiten zur Selbstorganisation von TMA wurden mit komplementäre Untersuchungen mit IA, TA und BA kombiniert. Diese Moleküle bestehen aus einem zentralen Phenylring, welcher mit einer unterschiedlichen Zahl von Carboxylgruppen substituiert ist. Die vergleichenden Untersuchungen mit aromatischen Carbonsäuren demonstrieren die strukturbestimmende Rolle intermolekularer Wasserstoffbrücken. IA und TA assemblieren in einer flachen Orientierung unter Herausbildung von Wasserstoffbrücken – verbrückten Zigzag- und Bänderstrukturen. Ein Dimer - Motif wurde als zentrales Strukturelement identifiziert. BA assembliert in molekularen Tetramereinheiten. Alle drei Moleküle ändern ihre Orientierung von planar zu senkrecht bzw. verkippt durch Adjustieren des Elektrodenpotentials zu positiven Ladungsdichten. Diese Interpretation wird durch komplementäre infrarotspektroskopische Untersuchungen unterstützt.

Der zweite Teil der vorliegenden Dissertationsschrift fokussiert auf Arbeiten zur Selbstorganisation und zu den Redoxeigenschaften von Adsorbatschichten der Viologenderivate N-Alkyl-N'-(n-Thioalkyl)-4,4'-Bipyridin Bromid (HS-nVn-H) und N,N'-Di-(n-Thioalkyl)-4,4'-Bipyridin Bromid (HS-nVn-SH), n = 5, 6, 7, 8, 10) an Au(111)-(1x1) Elektroden. Die hergestellten Adsorbatschichten zeigen zwei charakteristische Einelektronen – Redoxreaktionen ($V^{2+} \leftrightarrow V^{\bullet+}$, $V^{\bullet+} \leftrightarrow V^{0}$), welche mittels zyklischer Voltammetrie charakterisiert wurden. Strukturelle Details der erzeugten Adsorbatschichten wurden in in-situ RTM Experimente aufgeklärt. Drei Strukturen wurden identifiziert, eine ungeordnete und eine geordnete Streifenstruktur

bestehend aus planar orientierten Viologenderivaten bei kleinen Bedeckungsgraden, sowie eine dichtgepackte Adsorbatschicht gekippter Moleküle bei hohen Bedeckungsgraden. Die Einheitszellen der geordneten Adsorbatschichten bei kleinen Bedeckungsgraden sind rechteckig mit einer kurzen Distanzlänge von 0.5 nm und einer langen Distanzlänge, welche mit 0.2885 nm per CH_2 – Einheit variiert. Bei hohen Bedeckungsgraden konnte für die Monothiolviologene eine ($\sqrt{7}$ x $\sqrt{7}$) Struktur identifiziert werden. Die geordneten Adsorbatschichten sind kommensurabel zum Au(111) Substratgitter.

Die Elektronentransporteigenschaften von Au(T)│HS-nVn-SH(HS-nVn-H)│Au(S) - Brücken wurden mittels in-situ RTS studiert. Die Leitfähigkeit von Einzelmolekülbrücken zeigte bei konstanter Bias-Spannung eine sigmoide Abhängigkeit vom Substratpotential. Dieses Resultat kann auf die Änderungen der elektronischen Struktur der Viologengruppe als Folge des Redoxprozesses $V^{2+} \leftrightarrow V^{\bullet+}$ zurückgeführt werden. Experimente mit Monothiol - modifizierten Substraten (oder RTM - Spitzen) Au(S)-S-6V6-H│Au(T) zeigen bei konstanter Biasspannung ein Maximum in der Tunnelstrom – Potential Charakteristik, welches in der Nähe des Gleichgewichtspotentials für den Redoxprozess $V^{2+} \leftrightarrow V^{\bullet+}$ lokalisiert ist. Durch Variation der Biasspannung wird eine Dioden-analoge Charaktersitik erhalten. Das Verstärkungsverhältnis erreicht Werte bis zu 70. Die experimentell beobachteten Tunnelcharakteristika werden tentativ mit einem sequentiellen Zweistufen - Elektronentransportmechanismus beschrieben.

Contents

Chapter 1. Introduction

1.1 Nanoelectronics

1.1.1 General

Silicon-based electronics have seen a sustained exponential decrease in size and cost and a similar increase in performance and level of integration over the last thirty years [1]. The integration density of the circuits has doubled every 12 to 18 months: this observation is known as Moore's law [1] illustrated in Fig. 1-1.

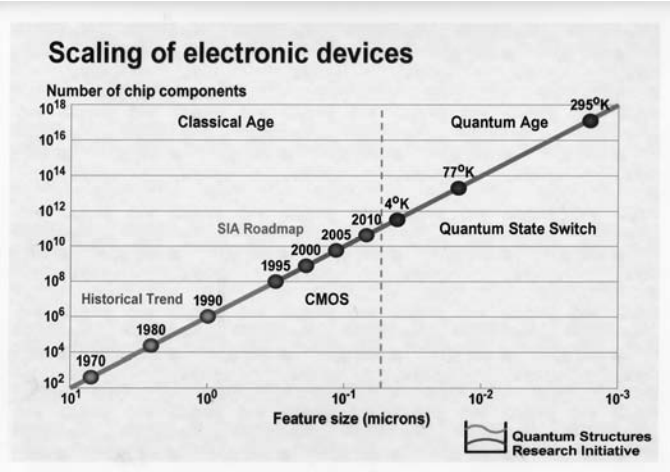

Fig. 1-1: Moore's law: The trend predicts an exponential decrease in size with an increase in the number of chip components per area [2].

As the miniaturization of electronic components approaches the nanometer scale, new concepts to tailor structure and fabrication strategies are essential to overcome the fundamental physical and economic limitations of conventional inorganic silicon-based technologies [3]. Bottom-up methods and the use of well-defined nanoscale building blocks, such as tailored molecules or quantum dots [4] to build complex functional objects, represent an attractive alternative. The bottom-up approach is complementary to traditional top-down materials processing, such as microfabrication techniques based on various lithographic approaches, and it makes use of self-

assembly processes for ordering of supramolecular or solid-state architectures from atomic to mesoscopic dimensions [5].

Currently, hybrid techniques are developing using both approaches, and many novel applications are likely to combine different fabrication concepts. Examples are illustrated in Fig. 1-2. The self-assembly of nanoscale building blocks, which may be represented even by single molecules, represents a particular promising approach to future nanoelectronics, which will be described next.

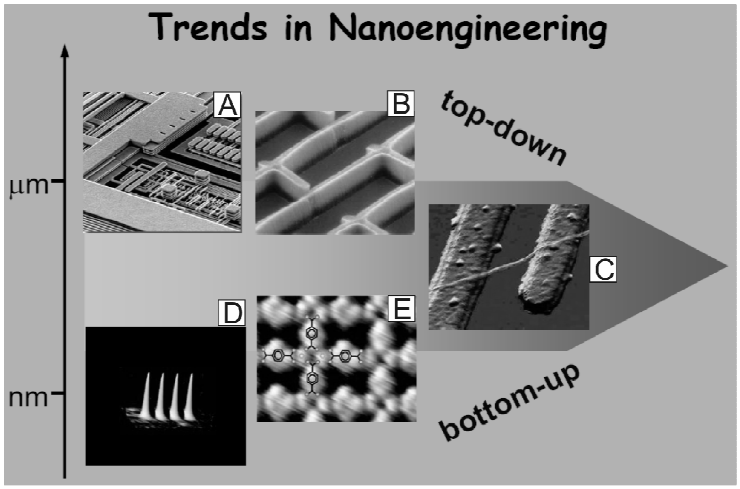

Fig. 1-2: Top-down and bottom-up approaches to create nanoscale structures [5]. (A) electron microscopy image of an electronic circuit prepared by the Damascen IBM copper plating process [6], (B) patterned films of carbon nanotubes obtained by microcontact printing and catalytic growth [7], (C) a single nanotube connecting two electrodes [8], (D) an array of individual CO atoms on Cu(100) as positioned with the tip of a scanning tunneling microscope at low temperatures, (E) 2D lattice of a network of Fe atoms coordinated with terephthalic acid linker molecules on Au(111) [5].

The bottom-up approach of constructing complex architectures is a widespread principle in nature. Examples are inorganic minerals, crystals, clays and the fascinating world of biology and living matter [9]. Building advanced materials via the bottom-up method, e.g. the control and modification of the fabrication processes, requires not only the understanding of the individual building blocks, but also a deep knowledge of the cooperative properties of individual construction units and bricks.

1.1.2 Self-assembly and supramolecular chemistry

Derived from concepts of supramolecular chemistry, self-assembly represents a promising bottom-up method to create molecule-based nanoscale entities. Jean-Marie Lehn, one of the pioneers in chemical self-assembly, described the supramolecular chemistry as "the chemistry of the intermolecular bonds", which involves recognition, transformation and translocation of information [10,11]. Self-assembly occurs when molecules interact with one another through a balance of attractive and repulsive interaction (Fig. 1-3) [10]. Intermolecular interactions in supramolecular chemistry, such as hydrogen bonds, van der Waals and Coulomb interactions, are generally weak and noncovalent. Supramolecular structures are the result of not only additive but rather of cooperative interactions. Their properties are determined by the complex interplay of the individual building blocks. The properties of the assembled architectures are not just the sum of the single component's properties [12].

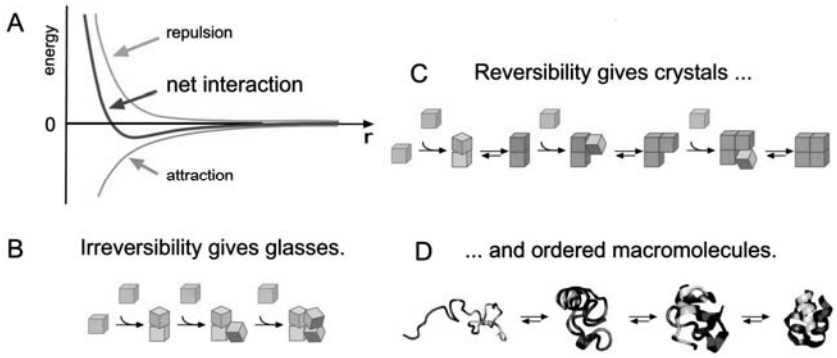

Fig. 1-3: Self-assembly occurs when there is a net attraction and an equilibrium separation between components [10].

1.1.3 STM and Nanoelectronics

The invention of the scanning tunneling microscope (STM) in 1981 by G. Binnig and H. Rohrer, followed by the development of the atomic force microscope (AFM) five years later, were crucial events in the history of nanoscience and nanotechnology [13]. STM may be regarded as a "nanoscale eye" and an "arm" for scientists to monitor and manipulate small entities such as atoms and molecules at surfaces and interfaces under a wide range of conditions in real space and in real time.

The STM has had a tremendous impact on the field of nanoscience and nanoelectronics during the past 25 years, especially in investigations of two-dimensional (2D) patterns, the manipulation of nanostructures up to the monitoring of interfacial reactions and molecular vibrations. Electron transport processes in nanoscale structures represent another fascinating field, which was, especially very recently, dramatically accelerated by new technical developments in scanning probe microscopy. The operating principle of a scanning tunneling microscopy and selected applications in nanosciences will be described in Chapter 2.

1.2 Self-Assembled Monolayers (SAMs)

1.2.1 General

Self-Assembled Monolayers (SAMs) of organic molecules are nanostructures. The properties of these SAMs can be tuned by the individual molecular building blocks as well as the substrate materials chosen. A “simple” SAM may be represented by an alkanthiol adlayer assembled on a gold substrate. This system comprises one of the most elementary forms of a nanometer-scale organic thin-film material [14]. Its thickness ranges typically between 1-3 nm. Fig. 1-4 shows a schematic diagram of a SAM [15].

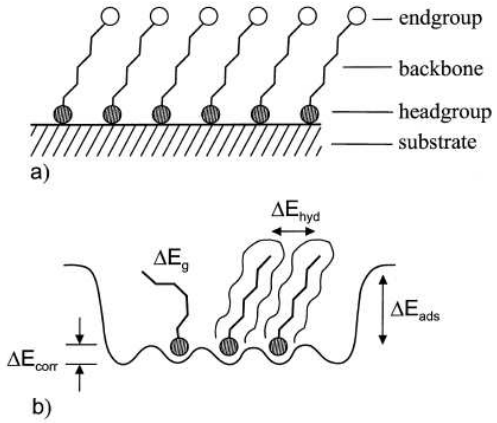

Fig. 1-4: (a) Schematic representation of an alkanethiol-based SAM. The shaded circles indicate chemisorbed headgroups. The open circles illustrate the endgroups. (b) Energy diagram. ΔE_{ads} represents the adsorption energy, ΔE_{corr} the corrugation of the substrate potential experienced by the molecule, ΔE_{hyd} represents van der Waals interactions within the (hydrocarbon) tails, and ΔE_g the energy of a typical (gauche) defect [15].

Understanding how molecular bricks self-assemble represents a key step for the design of (supra)-molecular devices based on bottom-up construction principles [16]. The interactions in supramolecular assemblies are typically noncovalent. They are weak and vary from less than 5 kJ mol^{-1} for van der Waals forces, 10 - 65 kJ mol^{-1} for hydrogen bonds, to 250 kJ mol^{-1} for coulomb interactions (Table 1-1) [17]. Among these interactions, hydrogen bonding is a particularly important building principle in the design of supramolecular materials and the engineering of nanostructures on surface. An example from our own work will be described in detail in Chapter 4 of this dissertation. In case of the 2D supramolecular self-assembly of molecules on surfaces one also needs to consider adsorbate–substrate interactions.

type of interaction or bonding	strength (kJ mol^{-1})
covalent bond	100−400
Coulomb	250
hydrogen bond	10−65
ion−dipole	50−200
dipole−dipole	5−50
cation−π	5−80
$\pi-\pi$	0−50
van der Waals forces	<5
hydrophobic effects	difficult to assess
metal−ligand	0−400

Table 1-1: Strength of typical non-covalent forces in supramolecular chemistry [17].

Self-assembly processes occur in many 2D and 3D systems [12,14,15,17,18]. However, in the following we will only focus on the 2D self-assembly of organic molecules on surfaces, which is directly relevant to our experimental studies on electrified solid/liquid interfaces.

1.2.2 Self-assembly of organic molecules

Several components and aspects directly related to SAMs of organic molecules will be discussed before we describe the different types of self-assembly. The formation of stable molecular adlayers requires a well-defined surface. Such a surface and the physical object supporting that surface are often referred to as the “substrate” [14]. Substrates range from polycrystalline metal films to well-defined single crystal surfaces depending on the anticipated applications and requirements. Often one uses noble metal crystals, such as single crystal gold electrodes [Au(111), Au(100) or

Au(110)], HOPG (highly oriented pyrolytic graphite) or thin metal films deposited on silicon or mica. SAMs can be prepared by adsorption of molecules from a liquid or from a gas phase.

SAM of covalently bonded thiol-terminated molecules

The early work on SAMs focused largely on organosulfur compounds, specifically alkanethiols assembled on gold substrates. This system developed as a model for organic monolayers and thin-film assembly [17]. Fig. 1-5 illustrates, as an example, a decanethiol SAM on Au(111). The dark pits in panel A represent vacancy islands, and the lines are domain boundaries. Panel B shows a high-resolution topographic image recorded after annealing the sample at 350 K for 4 hours. The temperature treatment increases the domain size and reduces the defect densities within the SAM [19].

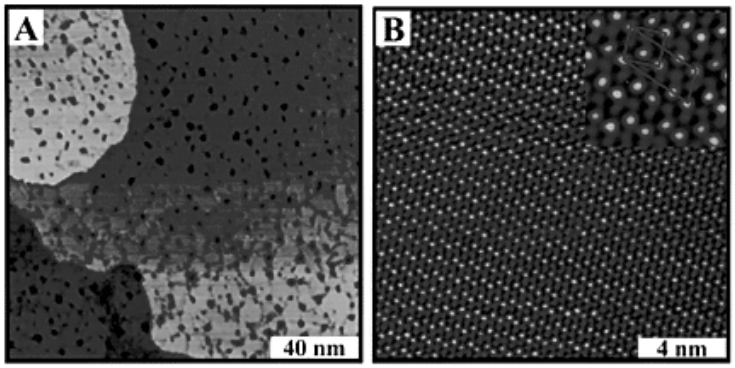

Fig. 1-5: Characteristic morphology of decanethiol SAMs on Au(111) [19].

The growth kinetics of SAMs have been studied using many "macroscopic" techniques, for instance second-harmonic generation (SHG, [20,21]), near edge x-ray absorption fine structure measurements (NEXAFS, [22]) and the quartz crystal microbalance (QCM, [23]). These studies found that the growth rate is proportional to the number of unoccupied adsorption sites, in agreement with simple first-order Langmuir adsorption kinetics [20, 21, 23].

$$\frac{d\theta}{dt} = -k(1-\theta) \qquad (1.1)$$

where θ is the occupied sites fraction, t is time, and k is a rate constant that contains the flux of the thiol molecules to the surface and the sticking coefficient. The rather fast adsorption process is followed by a second process, which may lead to a long-range ordered adlayer [20].

In addition to the spatially averaged information obtained by the above techniques, microscopic aspects and a detailed molecular-scale understanding of the mechanism of self-assembly were explored by scanning tunneling microscopy. Poirier et al. carried out pioneering experiments under ultrahigh-vacuum (UHV) conditions [20].

Fig. 1-6 schematically summarizes the proposed self-assembly mechanism of short-chain alkanethiols on a Au(111) surface. According to this mechanism, with increasing coverage, the thiol molecules sequentially form a lattice-gas phase, a low-density ("striped") solid phase, and a higher density solid phase [20].

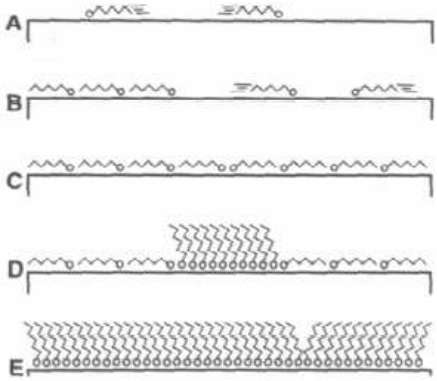

Fig. 1-6: Schematic representation of the different adsorption phases for the assembly of a short-chain alkanethiol on Au(111): (A) Thiols adopt the highly mobile lattice-gas phase at very low coverage. (B) Striped-phase islands nucleate heterogeneously and grow in equilibrium with a constant-pressure lattice gas. (C) Surface reaches saturation coverage of striped phase. (D) Surface undergoes lateral pressure-induced solid-solid phase transition by nucleation of high-density islands at striped-phase domain boundaries. (E) High-density islands grow at the expense of the striped phase until the surface reaches saturation [20].

Self assembly via non-covalent bonds

The second type of self-assembly is based on non-covalent intermolecular interactions. Tuning direction and strength of intermolecular and molecule-substrate interactions allow creating a variety of controlled nanoscale patterns.

Fig. 1-7 shows as an example systematically substituted porphyrine molecules on a reconstructed Au(111) surface. Changing the position of the CN-group, which provides a specific site for intermolecular hydrogen bonding, leads to a variety of molecular nanostructrues.

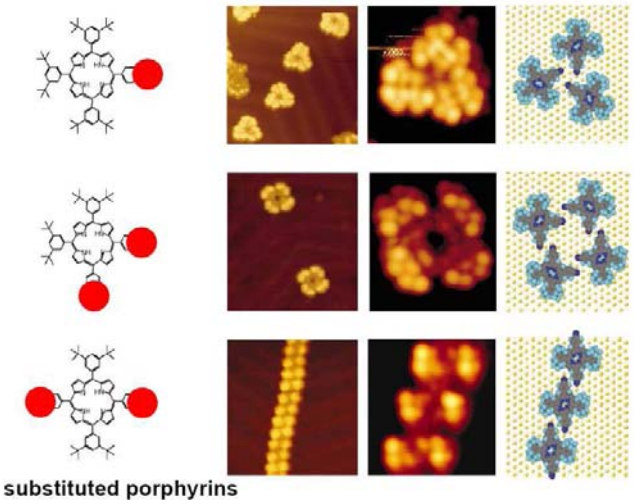

Fig. 1-7: Self-assembly of porphyrines on Au(111)-(px√3) through non-covalent interactions [5,24]. The red spots stand for the CN- group capable to form intermolecular hydrogen bonds.

In addition to monomolecular systems, multicomponent approaches have been developed to fabricate mixed adlayers with unique novel properties, through the use of host-guest or coordination systems [24].

1.2.3 2D supramolecular assembly on electrode/electrolyte interfaces

Self-assembly of organic molecules on electrode/electrolyte interfaces differs in general very much from those under ambient or ultrahigh vacuum (UHV) conditions [25]. Electrified surfaces and the electrochemical environment provide a unique setting to influence the ordering process and to tailor molecular structures.

In molecular electrochemistry, the electrode potential acts as an universal tuning source since the Fermi level, or the free energy of the surface system, is directly correlated to the electrochemical potential (Fig. 1-8) [27]. The electrode potential acts as a central tuning source for the assembly as well as to address nanostructures in an electrochemical environment.

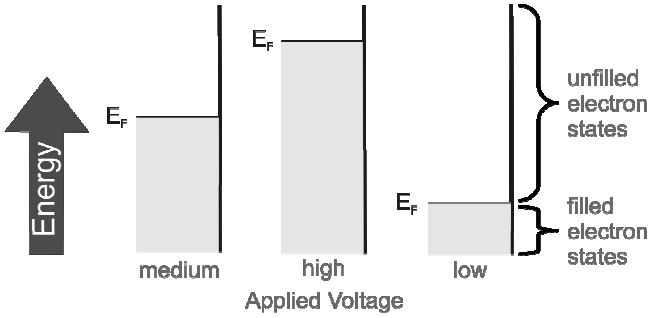

Fig. 1-8: Representation of the Fermi levels of electrodes for different polarization conditions [27].

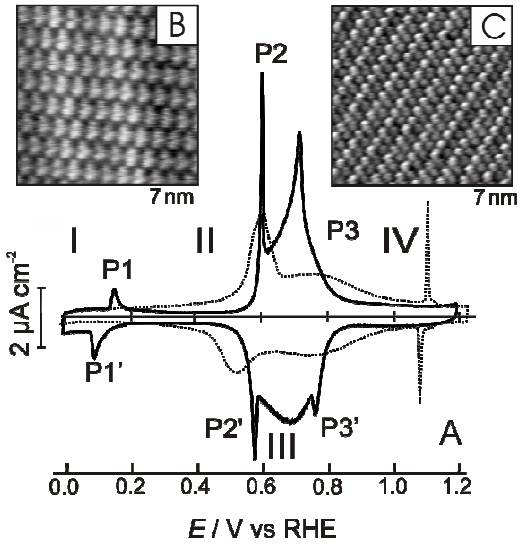

Fig. 1-9: Potential-induced adlayers of uracil molecules on Au(111). (A) cyclic voltammograms for Au(111) + 0.1 M H_2SO_4 in the absence (dotted line) and in the presence (solid line) of 12 mM uracil. (B) and (C) show STM images of flat-lying and vertical-oriented molecules [28].

The example illustrated in Fig. 1-9 shows that molecular orientation can be controlled at the electrode/electrolyte interface by the electrode potential [28]. At

negative potentials (potential region II), uracil molecules assemble on the surface in a planar configuration, but at positive potentials (potential region IV) in a vertical orientation. The main results of our own studies on potential-controlled molecular adlayers and structure transitions of carboxylic acids on single crystal gold electrodes will be presented in Chapter 4 of this dissertation.

1.3 Electron Transfer at the Nanoscale

A particular challenging and fascinating topic in nanoelectronics as well as in molecular-scale surface electrochemistry represents electron transport studies with nanostructures in various environments.

1.3.1 Electron transfer through SAM

The development of reliable methods to measure the electrical conductance of single molecules and tailored molecular assemblies at the nano-scale level represent key issues in a future molecular electronics [29]. SAM-based monolayer junction attracted great interests. They represent promising tutorial systems for exploring basic concepts [30].

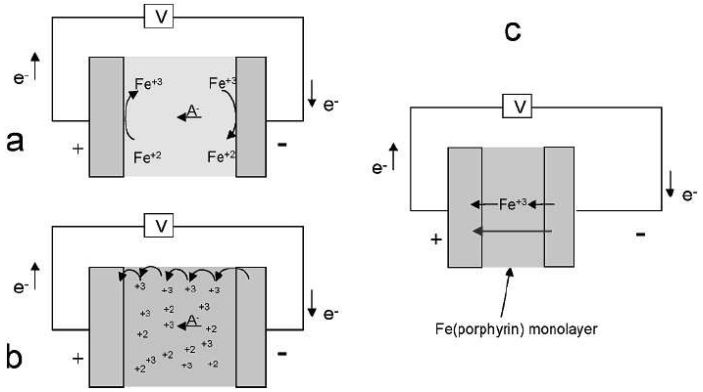

Fig. 1-10: Schematics of electron transfer processes in a conventional electrochemical cell (a), a redox polymer thin film (b) and a monolayer tunneling junction (c) [30].

Monolayer molecular junctions are historically related to both organic thin film devices and redox polymer films embedded between two conductors [30]. Fig. 1-10a shows a conventional electrochemical cell with a redox process (Fe^{2+}/Fe^{3+}) taking place on both electrodes, in which the electrolyte acts as ion carrier. The hopping of

charge occurs in redox-polymer films (Fig. 1-10b). In the tunneling junction (Fig. 1-10c), electrons may tunnel directly (red arrow in Fig. 1-10c), or through resonance levels of immobilized "redox molecules" [30].

1.3.2 Electron transfer in molecular junctions

Recently developed techniques demonstrated the creation of nanometer-sized molecular junctions enabling electron transport studies at the single molecular level. Selective approaches for fabricating nanogaps and nanojunctions bridged by single or small groups of molecules are illustrated in Fig. 1-11. Examples are mechanically controllable break junctions (MCJ) [31,32,33], electrochemically etched nano-gaps [34,35], mercury junctions [36], and scanning probe microscopy (SPM) based techniques [34,36,37,38] etc. The statistical analysis of the experimental data gives access to a wide range of single (molecular) junction properties.

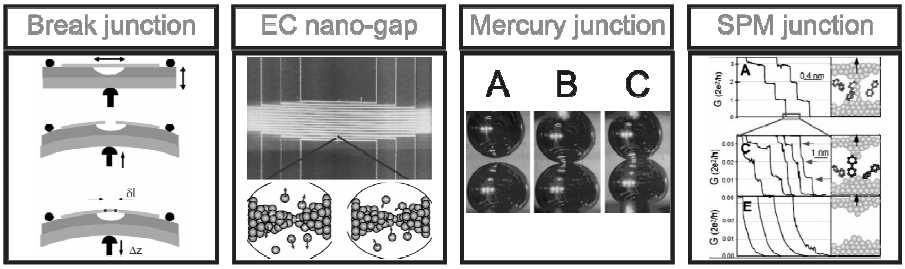

Fig. 1-11: Various techniques for investigating electron transport properties in metal | molecule | metal junctions composed of single or small groups of molecules.

ET through a nano-scale gap or molecular junctions may occur by coherent or incoherent tunneling. Coherent tunneling is based on the probability of an electron traversing a barrier of given width and height while maintaining the phase [30].

The rate of coherent tunneling decreases exponentially with the thickness of the barrier and is given, in a first approximation, by the Simmons relation (Equation 1.2) [30]:

$$J = \frac{q^2 V}{h^2 d}(2m\Phi)^{1/2} \exp\left[\frac{-4\pi d}{h}(2m\Phi)^{1/2}\right] \qquad (1.2)$$

in which J is the current density, q the electron charge, V the applied voltage. Φ and d are the barrier height and width, respectively. In case of a molecular junction, d is the

distance between two electrodes. Coherent tunneling is effective only for short distance, i.e. less than 2.5 nm [30].

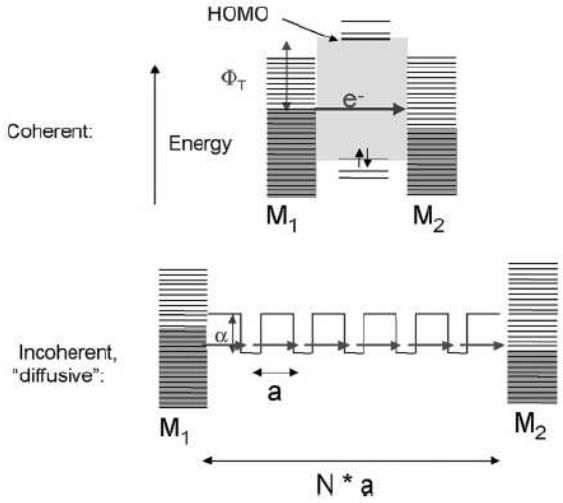

Fig. 1-12: Schematic diagram for coherent and incoherent tunneling. [30].

The tunneling over longer distances as well as through resonance states results in another type tunneling mechanism, called incoherent tunneling. The incoherent tunneling model [30,39,40] proposes that the electron tunnels coherently along a series of sites, which are separated by potential wells (Fig. 1-12)

Under electrochemical conditions, SAMs with functionalized molecules, such as organic molecules containing redox centers, can be specifically addressed by the electrode potential. The reference electrode acts via the electrolyte as a “gate electrode”. The gate thickness is determined by the electrochemical double layer, which extends typically to 1 – 3 nm giving rise to extremely high field strength of the order of 10^9 V m^{-1}. Tuning the redox states, i.e. the electronic state of tailored molecules incorporated in a molecular junction, enables exploring incoherent and resonance tunneling processes at electrified solid/liquid interfaces under room temperature conditions. Fig. 1-13 illustrates an example for a molecular junction formed between a gold STM-tip, a gold nanocluster attached to a redox-active viologen-dithiol and a gold substrate surface. Schiffrin et al. demonstrated that this configuration leads to molecular switching triggered by the injection of electrons [41].

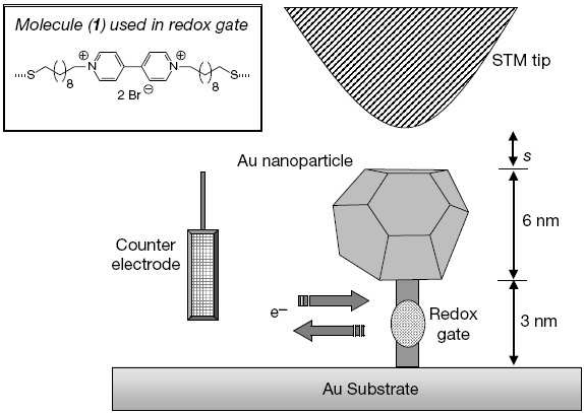

Fig. 1-13: Schematic representation of a nanoscale molecular switch realized in a vertical STM configuration [41].

In this dissertation, we will present in Chapter 5 results of the self-assembly and single molecular electron transport properties of functionalized alkylthiol-based viologens in an electrochemical environment.

1.4 Outline and Focus

The dissertation is organized as follow:

In Chapter 2, the principle of STM and EC-STM, their basic operation modes and selected applications will be introduced. The overview on experimental techniques will be complemented by a brief introduction into voltammetric techniques and Surface Enhanced Infrared Reflection Absorption Spectroscopy (SEIRAS).

Chapter 3 summarizes experimental procedures, such as details of electrode and solution preparation, STM tip fabrication and the specifics of the STS measurements employed in this dissertation.

A comprehensive study of the 2D assembly of aromatic carboxylic acids on Au(111) employing in situ STM in combination with cyclic voltammetry and SEIRAS will be presented in Chapter 4. We will focus on potential-induced steady state molecular structures as determined by intermolecular hydrogen bonds and substrate–adsorbate coordination, as well as on dynamic processes of structural transitions among the various adlayers. The target molecule is trimesic acid (TMA,

1,3,5-benzene-tricarboxylic acid). Comparative results will be also discussed for benzoic acid (BA), isophthalic acid (IA) and terephthalic acid (TA).

The knowledge obtained on the assembly of carboxylic acids on Au(111) electrodes is applied in Chapter 5 for exploring the assembly and single-molecule redox properties of tailored redox-active, thioalkyl-based viologen derivatives. The description of macroscale electrochemical properties is followed by in situ STM experiments characterizing steady state molecular adlayer structures. Subsequently, an approach to address electron transport in redox-active single molecular junction is presented.

Finally, we will summarize our studies in Chapter 6.

Chapter 2. Principles and Methods

2.1 Interfacial Electrochemistry

Interfacial electrochemistry may be described as the study of structures and processes at the interface between an electronic (the electrode) and an ionic (the electrolyte) conductor, or at the interface between two ionic conductors [42]. Electrochemical methods offer the ability to investigate complex structure and electron transfer processes at interfaces by monitoring current, charge or capacitance. In its simplest form, electrode reactions have been investigated in a two-electrode cell, which consists of a working electrode, a reference electrode, and the electrolyte as the conducting medium. The difference in electrical potential (E) between the two electrodes is called the cell potential, and is measured in volts (V). The value of the potential is a measure of the energy available to drive charge between the electrodes. Often, electrochemical experiments are carried out in a three-electrode configuration composed of a working electrode (WE), a reference electrode (RE), and a counter electrode (CE). The latter decouples the current flow across the working electrode and its potential control. An additional extension leads to a four-electrode configuration, which contains two working electrodes (WE1, WE2). The electrode potential of each is controlled with respect to the reference electrode (RE). This principle is applied in a 4-electrode potentiostat or bipotentiostat, which is used to control the potential of a substrate and a tip in an electrochemical STM experiment (cf. 2.2 EC-STM).

2.1.1 Electrode reactions

In interfacial electrochemistry all the reactions are considered to occur at or in the neighborhood of an electrode surface. An electrode reaction involves the transfer of electrons between the electrode and a species in solution or on the surface. When the transfer of electrons (Faraday-type reaction) takes place from the species to the electrode, the species is oxidized and the electrode reaction is an “anodic process”. On the other hand, when electrons are transferred from the electrode to the species, they are reduced and the reaction is a “cathodic process” (Fig. 2-1).

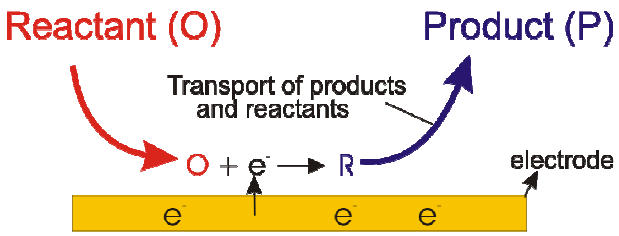

Fig. 2-1: A typical Faraday-type electrode reaction process involving the electron transfer between the electrode and the electrolyte solution [27].

2.1.2 Electrochemical double layer

At any metal electrode immersed in an electrolyte solution, a specific interfacial region is formed. This region is called the electrochemical double layer [43]. This region is very important because it is the place where gradients in electrical and chemical potentials constitute the driving force for electrochemical reaction and in which the charge transfer takes place [26]. Building up of the electrochemical double layer involves a charging or non-faradaic current.

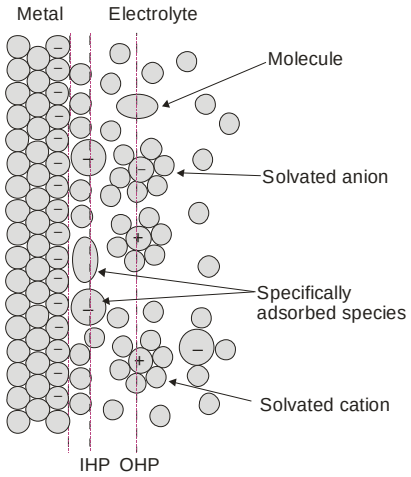

Fig. 2-2: Schematic diagram of the electrochemical double layer (EDL) formed at the metal/electrolyte interface.

The first concept of the double layer was proposed by Helmholtz [43] and further developed by Gouy and Chapman [44,45], Stern [45] Grahame [46], and more recently by Frumkin and Parsons. In a first approximation, the interfacial region is thought to be composed of a compact region, the so-called Helmholtz layer, and a

diffuse region, the so-called Gouy-region. The compact region is composed of the inner (IHP) and of the outer Helmholtz (OHP) plane (Fig. 2-2). The outer Helmholtz plane is defined by the distance of closest approach of solvated ions, typically cations, to the electrode. The positions of specifically or "contact" adsorbed ions (often anions) represent the inner Helmholtz plane [42]. The diffuse layer develops outside the OHP, in which the concentration of cations and ions decreases exponentially vs. the distance from the electrode surface. The extent of the diffuse layer depends on the ionic concentration in the electrolyte. A more detailed description of the various electrochemical double layer models can be found in reference [45].

2.1.3 Cyclic voltammetry

Voltammetry is one of the important techniques which electrochemists employ to investigate processes and mechanisms of the interfacial electrochemical reaction.

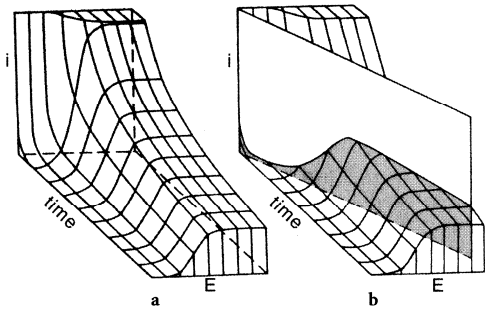

Fig. 2-3: (a) Schematic drawing of a three dimensional plot with a characteristic i-t-E relationship for transient and steady-state responses. (b) The trace following the intersecting plane shows approximately the peak characteristics of a linear sweep voltammograms [43].

Reinmuth [47] depicted the concept of the cyclic voltammogram in a three dimensional plot as shown in Fig. 2-3, in which the electrochemical information of a system can be obtained through a series of steps to different potentials following the recording of the corresponding current-time curves (Fig. 2.3a). Since the plot combines features of both transient and steady state techniques in a single experiment, the accumulation and analysis of the data is complicated and time-consuming. However, the analogous experimental information could be also obtained by sweeping the potential and recording the i-E curve directly, which is illustrated as the current trace in the diagonal cross section (Fig 2-3b). This is usually referred to as linear

sweep voltammetry (LSV) [43,45]. In case of cyclic voltammetry, the potential is swept first to one direction, then reversed and scanned to the opposite direction at the same sweep rate in a certain potential range (Fig. 2-4 left). A typical reversible current-voltage response has the form shown in Fig. 2-4 (right). The current response recorded when sweeping the potential to negative values called cathodic current (I_{pc}), and the positive counterpart is defined as anodic current (I_{pa}). The corresponding peak potentials are named E_{pc} and E_{pa}, respectively. The electrochemical formal potential is given as $E_0 = (E_{pc} + E_{pa})/2$.

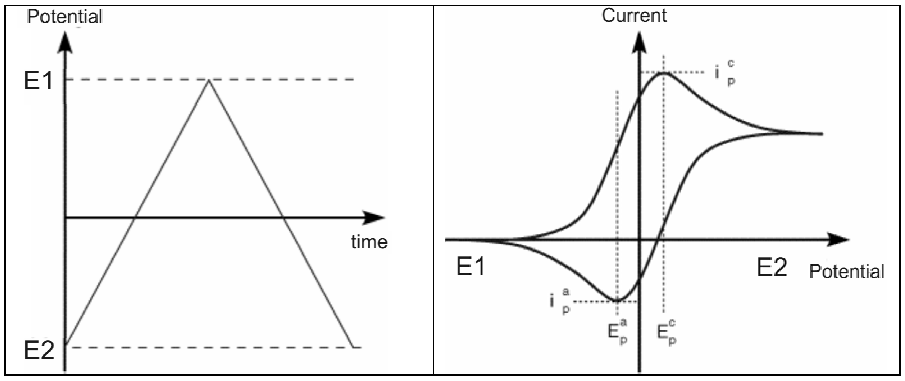

Fig. 2-4: The potential program in cyclic voltammetry [27].

Experiments are usually carried out in a solution containing a large excess of indifferent electrolyte in order to increase the conductivity of the solution, to eliminate effects of migration of any charged analyte and to compress the size of the double layer adjacent to the working electrode. For a diffusion-controlled, reversible electrochemical (Faraday) reaction the voltammogram recorded has certain well-defined characteristics [27].

i) The potential separation, which is derived from the Nernst equation, between the current peaks is $E_p = E_{pa} - E_{pc} = 59/n$ mV; n = the number of electrons.

ii) The ratio of the peak currents amounts to $(I_{pc} / I_{pa}) = 1$ at different scan rates.

iii) The peak current I_p is proportional to the square root of the scan rate ($v^{1/2}$) and to the bulk concentration (C^b).

In case of a surface-confined reversible redox reaction (adsorbed state), one observes a linear relation between scan rate v and the heights of the corresponding current peaks.

2.2 Electrochemical STM

We introduce in this section basic principles and the operation mode of scanning tunneling microscopy (STM) under electrochemical conditions (EC-STM).

2.2.1 Principle of STM

Scanning tunneling microscopy (STM) was invented at the Zürich laboratory of IBM in 1981 by G. Binnig and H. Rohrer, who were awarded the Nobel Prize in 1986. Over the last 25 years, STM has been applied to many fields of research, such as surface physics, materials science, biology, nano-electronics and interfacial electrochemistry.

The working principle of STM is based on the tunneling phenomenon. According to the tunneling theory, when an atomically sharp metal electrode (metal STM tip) approaches a conducting surface (STM substrate) at a very close distance, electrons from the Fermi levels of the two electrodes can tunnel through the gap (Fig. 2-5). If a bias voltage (the potential difference between a tip and a substrate, $E_{bias} = E_T - E_S$) is applied between the two electrodes, a tunneling current thus flows between the tip and the substrate. In vacuum, the current is exponentially dependent on the gap width.

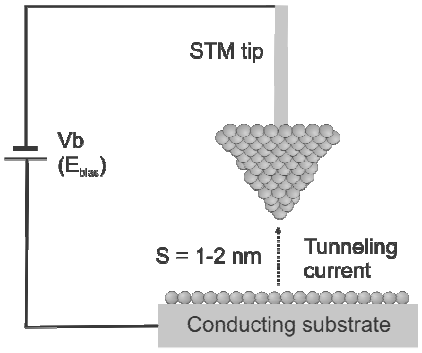

Fig. 2-5: Schematics of a tunneling experiment.

Scanning the tip in x-y direction allows to image the contours of the electronic states at the Fermi level of the substrate with high spatial resolution. The exponential dependence of tunneling current (I) on distance (s) can be expressed by Equation 2.1 [48], in which E_{bias} is the bias voltage, Φ represents the barrier height, and k is a constant.

$$I \propto E_{bias} \exp\left(-k\sqrt{\Phi}s\right) \tag{2.1}$$

Since the tunneling current depends exponentially on the gap width, a very small change of an apparent surface height (electronic state and surface morphology) can give rise to a large change of the tunneling current. Therefore, STM has an extremely high z resolution (typically 0.01 nm). For an atomically sharp tip, we may assume that there is only one metal atom at the apex of the tip, and a large percentage of the tunneling current will flow through it. The lateral resolution of an STM experiment may reach 0.1 nm in x and y direction.

The basic components of the microscope setup comprise a sharp conducting STM tip, which is typically prepared from tungsten, Pt/Ir, or gold wires depending on the experimental purpose, a substrate (conducting sample) and a mechanism to control the location of the tip when scanning in x and y direction parallel to the sample surface (Fig. 2-6). The latter is accomplished by means of piezoelectric actuators in the STM scanner, which are often made of lead zirconium titanate [49]. The set-up is completed by the electronic system (controller) and a computer for controlling the whole working system and to process the data recorded. Fig. 2-6 illustrates the basic working principle. With the bias voltage (the potential between the tip and substrate) applied, electrons tunnel through the gap between the tip and the substrate. The tunneling current is measured with a preamplifier and then this signal becomes the input signal of a feedback loop [49], which is designed to keep the tunneling current constant during the (x,y)-scanning in the constant current mode. Meanwhile, the tip goes up and down with the piezo to keep the tunneling current constant, which is illustrated in Fig. 2-6 [49].

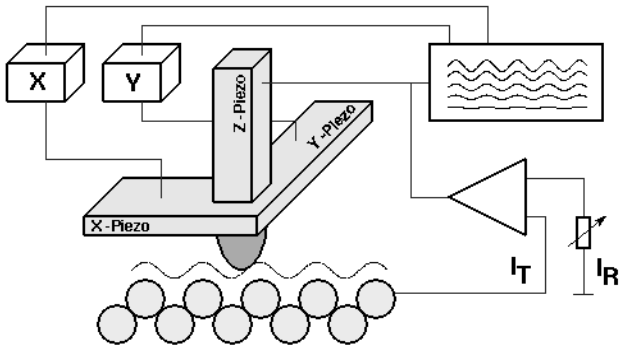

Fig. 2-6: The basic components of the microscope setup [50].

There are two types of scanning modes, the so-called constant current mode and the constant height mode as illustrated in Fig. 2-7. In the first case, the tunneling current is kept constant (at a preset value) by the feedback during the scanning, and the surface morphology (electronic and geometric contributions) was monitored by recording the tip displacements in vertical direction as a function of its lateral position. In case of the constant height mode, the tip is kept at the same height during scanning, and the modulation of the tunneling current is measured. The image represents the tunneling current values as a function of the horizontal position and the surface properties. Scanning in constant height mode is preferred for scanning at high speed. An atomically flat sample surface is required to prevent tip crashing, which limits its applications somewhat. The constant current mode is more frequently used. All images reported in this dissertation were recorded in this scanning mode.

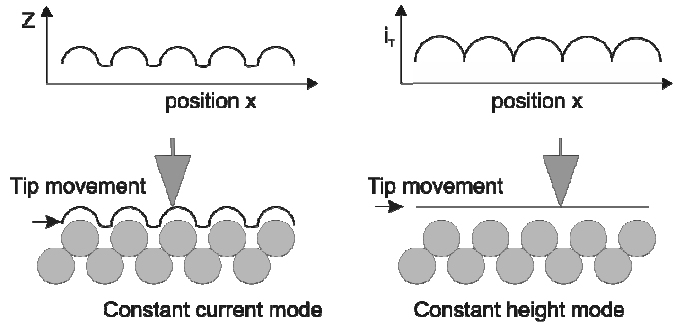

Fig. 2-7: Two types of STM scanning modes: the constant current mode and the constant height mode.

2.2.2 The electrochemical STM

STM can work in different environments, e.g. under ambient conditions, in ultra high vacuum (UHV), at low temperature (LT-STM), and in an electrochemical environment. The latter means working in a conducting electrolyte, which will be described next.

Electrochemical scanning tunneling microscopy (EC-STM) combines the STM with the electrochemical environment, which make the EC-STM one of the most powerful structure-sensitive in situ techniques for exploring bare and adsorbate-covered electrode surfaces.

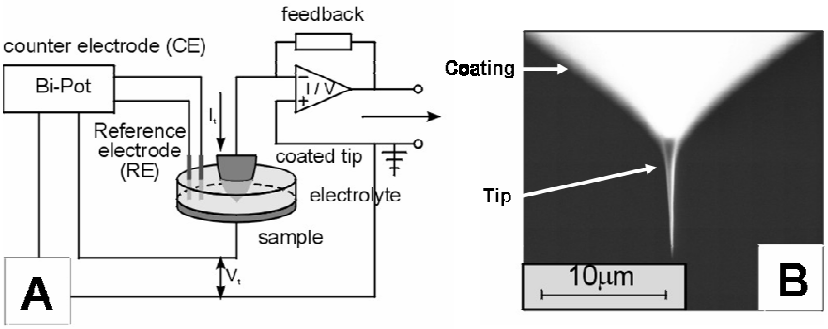

Fig. 2-8: (A) Schematic diagram of an electrochemical STM setup; (B) polyethylene coated tungsten tip [26].

Since the EC-STM works in a conducting environment (electrolyte), electrochemical reactions may take place at the tip as well as at the sample, superimposed on the tunneling current. They need to be controlled strictly. This is accomplished using a so-called bipotentiostat, with which the potential of sample and tip can be chosen independently versus a suitable reference electrode (Fig. 2-8). Furthermore, the tip needs to be coated with an insulating layer, e.g. polyethylene in our case, to minimize the contact area with the electrolyte. The remaining electrochemically active area of about 10^{-8} – 10^{-7} cm^2 yields faradaic currents of typically less than 5 pA, which do not interfere with tunnel currents of 100 pA to 10 nA [26,42].

In addition to the basic functions of an STM, such as the high-resolution spatial imaging and local investigation of electronic state, the EC-STM exploits the particular role of the electrode potential:

i) The electrode potential in EC-STM is a universal tuning source, which can be applied to tune adlayer structures and/or to control structure transitions on surfaces and at interfaces.

ii) Electrochemical gating. The variation of the Fermi levels of tip and substrate may allow to locally address single-molecular electron transfer properties. The electrolyte acts as "gate" via the reference electrode.

Fig. 2-9 A shows a large-scale in situ STM image of a thermally reconstructed Au(111) surface with the typical parallel zigzag reconstruction lines in 0.05 M H_2SO_4. In the high resolution image Fig. 2-9 B, the individual gold atoms and their positional arrangement, which change periodically in the 110-direction from face-centered cubic (fcc) through a transitional region of so-called "bridging site" (bright corrugation lines) to hexagonal close-packed (hcp) [51], are clearly discerned. For the unreconstructed Au(111) surface, STM reveals the hexagonal close-packed arrangement of gold atoms (Fig. 2-9 C).

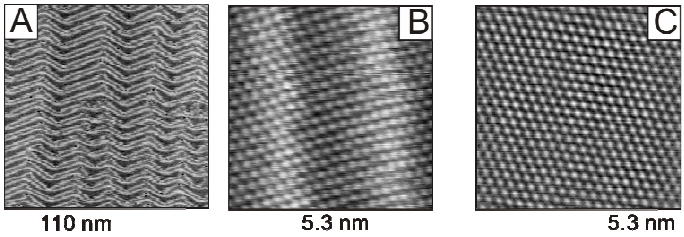

Fig. 2-9: (A) In situ STM images of Au(111)-(px√3): (A) large scale (B) high resolution of a Au(111)-(1x1) surfaces [51].

2.2.3 Scanning tunneling spectroscopy

In addition to the in situ imaging, scanning tunneling spectroscopy (STS) represents another important operation mode to explore the local electronic information of the sample surface and of various adlayers. Varying one of the

tunneling parameters in equation 2-1, e.g. distance s or bias E_{bias} allows to probe the the tunneling barrier properties by analyzing the i-Δs or i-E_{bias} characteristics. In case of an electrochemical environment, one also can sweep the substrate potential instead of varying the bias voltage and record so-called EC-IV spectroscopic data.

Current-distance spectroscopy

The shape of tunneling current–distance characteristics depends on the shape and the magnitude of the potential barrier the tunneling electrons are exposed to [52,53]. In case of a rectangular potential barrier, the tunneling current decays exponentially with distance:

$$i_T = i_0 \cdot \exp(-\kappa \cdot \sqrt{\phi_{rect}} \cdot \Delta s) \qquad (2.2)$$

where i_T is the tunneling current, ϕ_{rect} is the height of the rectangular barrier and κ is a constant which is equal to 10.12 $eV^{-1/2}$ nm^{-1} for a rectangular barrier height; i_0, a normalization current, accounts for the electronic properties of the metal surface and the bias voltage. According to this equation, we can relate a single barrier value to an exponentially decaying i-Δs characteristic [52].

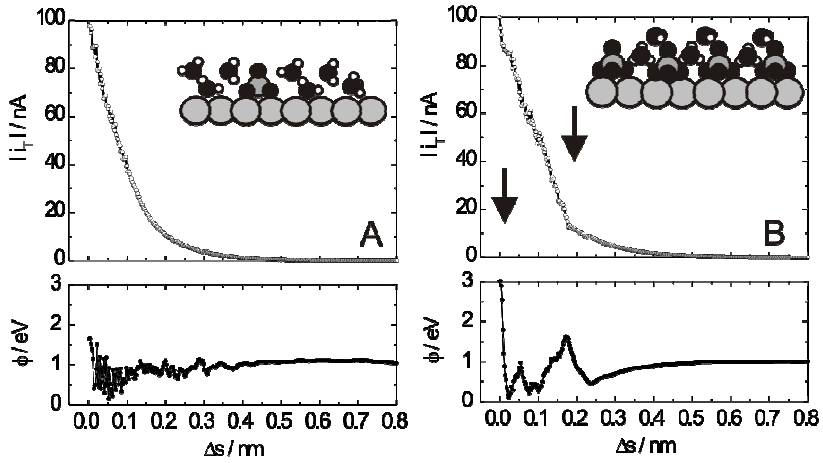

Fig. 2-10: (A) Left: averaged i-Δs characteristics (i_T) and the calculated one-dimensional potential barrier height profile (Φ) of Au(111) / H_2SO_4 for the disordered adsorption of sulfate ions and water. (B) Right: averaged i-Δs characteristics (i_T) and the calculated one-dimensional potential barrier height profile (Φ) of Au(111) / H_2SO_4 for an ordered √3 x √7 adlayer of sulfate [52].

Fig. 2-10 illustrates current-distance traces applied to explore properties of the electrochemical double layer [52]. The bare Au(111) electrode covered with a disordered adlayer exhibits a simple exponentially decaying i-Δs curves (Fig. 10 A). For the surface covered with an ordered adlayer, e.g. the √3 x √7 adlayer of sulfate ions shown in Fig. 2-10 B, the i-Δs characteristics exhibit non-exponential segments, which were shown to correlate with the actual adlayer structure [52].

EC-IV spectroscopy

EC-IV spectroscopy allows to explore specific tunneling properties in an electrochemical environment. The tunneling properties of porphyrine (non-redox) and metalloporphyrines (redox) were investigated in an in situ STM configuration [54]. The experiment started with a mixed ordered adlayer of the redox-active and redox-inactive molecules. In situ images were recorded for various substrate potentials, e.g. for the oxidized and the reduced form of the redox-active metalloporphyrine. A tunneling resonance phenomenon was observed upon reaching the electrochemical formal potential of the redox couple.

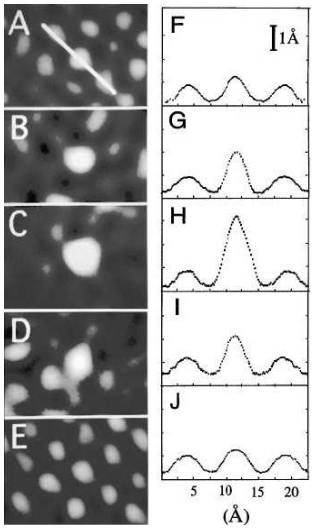

Fig. 2-11: STM image of FePP (Fe-protoporphyrine) embedded in an ordered array of protoporphyrine (PP). The substrate was held at -0.15 (A), -0.30 (B), -0.42 (C), -0.55 (D), and -0.65 V (E), respectively. (F)-(J) are the corresponding plots of the cross section along the white line indicated in (A) [54].

2.2.4 Fabrication and manipulation at the nanoscale

Scanning tunneling microscopy is also applied for the fabrication and manipulation of nanostructures. Since the STM tip can be accurately controlled by piezoelectric actuators in 3D space at the nanoscale level, it can be also regarded as the arm of a robot to build nanostructures. The necessary control can be obtained through electrostatic forces, van der Waals forces or by pulsing the electrode potential. Fig. 2-12 A shows a "quantum corral" constructed from Fe atoms adsorbed on a Cu(111) surface [55] as fabricated by Crommie et al with STM at low temperature (4K).

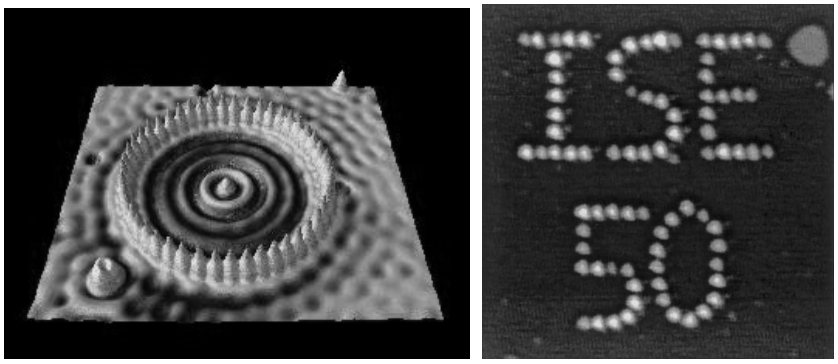

Fig. 2-12: (A) Left: A "quantum corral" of 48 Fe atoms adsorbed on a Cu(111) surface [55]. (B) Right: Cu clusters, 0.6 nm high, fabricated with an STM tip onto Au(111) in 0.05 M H_2SO_4 + 1 mM $CuSO_4$ [56].

Fabricating nanostructures with STM in an electrochemical environment offers another opportunity to control chemical reactions at the nanoscale. Fig. 2-12 B shows an example where Kolb et al. deposited Cu clusters at various, well-defined positions on a Au(111) surface under electrochemical conditions. The technique was used to selectively create and erase nanostructures at solid/liquid interfaces [56].

2.3 ATR-SEIRAS

Surface enhanced infrared reflection-adsorption spectroscopy (SEIRAS) in combination with electrochemistry is becoming an important complementary approach for EC-STM to explore properties of electrified solid/liquid interfaces [57].

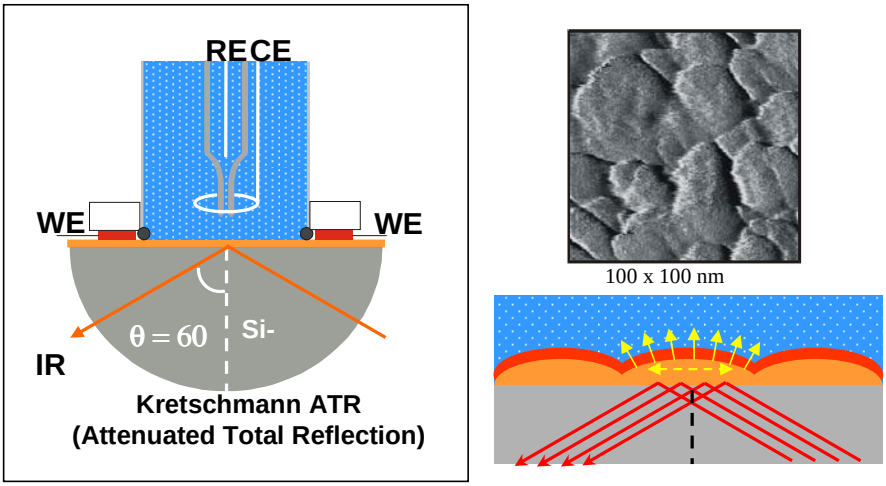

Fig. 2-13: (A) Left: Schematic diagram of an ATR-SEIRAS setup; (B) Right-up: AFM image of the SEIRAS gold film deposited on silicon prism. (C) Right-down: illustration for the total reflection and surface enhancement effect in an ATR configuration [58].

The basic principle and experimental setup of ATR-SEIRAS are illustrated in Fig. 2-13. The electrochemical in situ measurement is carried out in a three-electrode spectroelectrochemical cell employing an *attenuated total reflection* (ATR) configuration, in which the reflected IR signal is collected on the other side of the electrochemical interface. A thin layer of Au (20~25 nm in thickness) is used as working electrode as shown in Fig. 2-13. The AFM image of the film is composed of Au islands with an average diameter of about 30 nm. The surface-enhancement results from the polarization of these metal islands by the electromagnetic field of the incident radiation. The IR absorption intensity can be significantly increased by 10~1000 times on islands of coinage metals, in comparison to conventional IR measurements such as IRRAS [57,59,60].

The induced electric field is normal to the local island surface. This leads to the *surface selection rule*: only the molecular vibrations having dipole changes normal to the local surface can be excited and enhanced. This selection rule allows to explore the orientation of adsorbed molecules. On the other hand, the local electric field decays within a short distance away from the surface, which implies that this local enhancement occurs only in the near vicinity of the islands. The dominant contribution arises from adsorbed species in the first layer (Helmholtz region) and

minor contribution from subsequent layers [57]. The application of the SEIRAS technique to electrochemical interfaces was pioneered by Osawa et al [59].

In summary, in situ STM in combination with cyclic voltammetry and ATR-SEIRAS experiments represent a powerful method to qualitatively and quantitatively explore interfacial structures and reactions under steady-state as well as dynamic (time-resolved) conditions, which will be demonstrated by studying supramolecular nanostructures of carboxylic acids (Chapter 4) and exploring the self-assembly and electron transfer properties of viologen molecules (Chapter 5) in the present dissertation.

Chapter 3. Materials and Experimental Procedures

3.1 Electrodes and Sample Preparation

3.1.1 Au working electrodes

Three types of gold working electrodes were employed to investigate the structure properties of molecular adlayers and to explore electron transfer properties of redox molecules: (1) Au(111) single crystal disc electrodes (10 mm in diameter and 2 mm in height) for in situ STM experiments; (2) Au(111) single crystal cylinder-type electrodes (4 mm in diameter and 4 mm in height) for electrochemical experiments; (3) Au(111-25 nm) gold thin film electrodes for ATR-SEIRAS measurements. Clean and well-defined surfaces are crucial for high-quality experiments. Therefore, a particular routine for electrode preparation was followed before each experiment.

For STM experiments, the disc-type electrodes were carefully annealed in a hydrogen flame at red heat for 7 minutes (Fig. 3-1 A). The crystal was positioned on a Ceran® glass plate. The flame annealing is usually performed in a dark room to readily distinguish the temperature according to the color of the crystal. Fig. 3-1 B shows a crystal at red heat (temperature of approximately 600-700ºC) during a typical annealing step.

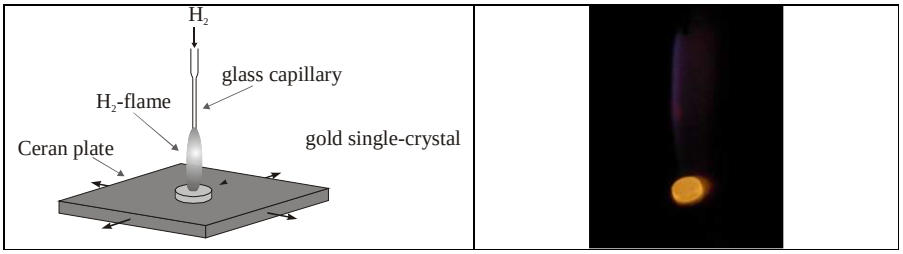

Fig. 3-1: (A) Left: schematics for the flame-annealing of a gold single crystal disc-type electrode. (B) Right: photograph of a Au(111) crystal at red heat during the annealing in a hydrogen flame [61].

After flame-annealing, the crystal was cooled down in high-purity argon and then immersed into 50 mM HCl for 20 min for lifting the thermally induced Au(111)-(p x √3) reconstruction. The resulting unreconstructed Au(111)-(1x1) surface is atomically flat with terraces several hundred nm wide, and very few, but large monoatomically high gold islands. Subesequently, the crystal was rinsed copiously with Milli-Q water to remove chloride ions. After drying with argon, the crystal is ready for surface modification or direct use in an in situ STM experiment.

The Au(111) electrodes for electrochemical (EC) experiments were single crystal cylinders. A gold wire was attached to the rear for mounting the electrode in a so-called hanging meniscus configuration [62]. The crystal was flame-annealed with a butane torch at red heat for 7 min and then cooled in argon before immersion into ultrapure water. Contact with the electrolyte was always established under potential control.

The working electrode for SEIRAS experiments was a quasi-single crystalline Au(111-25 nm) film electrode prepared by electron beam evaporation of gold onto the (111) plane of a silicon hemisphere, and subsequent electrochemical annealing. Details of the entire procedure were described in ref [57].

3.1.2 Electrode modification with viologens

Alkanethiol-substituted viologens are extremely sensitive to oxygen exposure during the sample preparation and the subsequent electrochemical measurements. The Au-S bond is very strong. Therefore, once the viologens are in contact with the Au surface, their mobility within the adlayer is low (at room temperature). Place exchange processes require a rather high activation energy.

Three different protocols were developed to prepare gold electrodes modified with viologen mono- and di-thiols to overcome these challenges: (1) Low-coverage *disordered* adlayers were obtained after immersion of a freshly prepared Au(111)-(1x1) electrode into a 50 μM deoxygenated ethanolic solution of the respective viologen derivative at room temperature for 1 min (cf. section 5.4). (2) Low-coverage *ordered* adlayers ("striped phases", cf. section 5.3) were prepared by exposure of the gold substrates at room temperature to 50 μM deoxygenated ethanolic, viologen-containing solution for 2 min, and subsequent annealing in pure ethanol at 70 ^{o}C for

12 hours. (3) High-coverage monolayers were obtained by immersion of the gold substrates into 1 mM ethanolic solution followed by thermal annealing in ethanol at 70 °C for 12 hours.

The thermal treatment of the samples was carried out in closed containers, which were deoxygenated. After incubation, the samples were removed from the solutions, rinsed with ethanol and carefully dried in a stream of argon.

3.1.3 Reference electrodes

Several electrodes have been employed in the in situ STM experiments as reference electrodes. They are compiled in table 3-1 and compared with other commonly used reference electrodes.

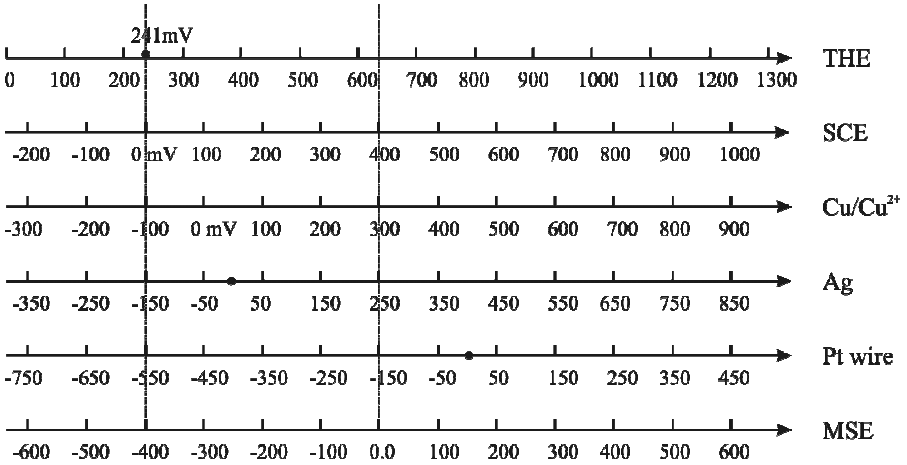

Table 3-1: Compilation of reference electrodes and their potential scales (in mV).

The studies on the 2D assembly of aromatic carboxylic acids (Chapter 4) were carried out in acidic electrolytes (0.05 M H_2SO_4 or 0.1 M $HClO_4$) with Pt wires as quasi reference electrodes. These electrodes are easy to prepare and exhibit a rather stable potential for pH < 4.0.

The experiments with viologen derivatives were typically performed in a neutral (50 mM $KClO_4$, pH = 7) or slightly alkaline solution (50 mM $KClO_4$ or 0.5 M $LiClO_4$, pH = 8.5) to access both one-electron redox processes $V^{2+} \leftrightarrow V^{\bullet+}$ and $V^{\bullet+} \leftrightarrow V^{o}$. Under those conditions and in the absence of oxygen, a Ag/Ag_xO_y quasi-reference electrode appears to be rather stable. Significant drift was observed in the presence of

oxygen. All STM experiments were carried out in a custom-designed all-glass environmental chamber to ensure a controlled, oxygen-free environment.

A saturated calomel electrode (SCE), a mercury sulfate electrode (MSE) and/or a trapped hydrogen electrode (THE) were used in all other electrochemical and SEIRAS experiments. All potentials in this dissertation are quoted with respect to a saturated calomel electrode (SCE).

3.2 Solution Preparation

One of the major challenges for electrochemical, and especially for the in situ STM experiments represents the strict control of contamination.

3.2.1 Caroic acid

Caroic acid is a 1:3 mixture of 35% aqueous H_2O_2 and 96% H_2SO_4. This mixture is a very strong oxidizing agent and was used to clean the glassware, the Teflon STM cells and the STM O-rings (Kalrez®). The parts were stored overnight (12 h) in caroic acid, and afterwards boiled in Milli-Q water. After additional rinsing with cold Milli-Q water, the glassware was ready for solution preparation, and the STM parts for mounting.

3.2.2 Electrolyte solutions

The electrolyte solutions were prepared with glassware either cleaned in caroic acid (STM) or in a 1:1 mixture of hot H_2SO_4 (96%) and HNO_3 (65%) followed by extended rinsing with Milli-Q water.

The following electrolyte solutions were used in this dissertation:

i) 0.05 M H_2SO_4 (Chapter 4)

ii) 0.05 M H_2SO_4 + 3 mM trimesic acid (Chapter 4)

iii) 0.1 M $HClO_4$ (Chapter 4)

iv) 50 mM HCl (for lifting of the reconstruction of the gold electrodes)

v) 0.5 mM isophthalic acid (saturated terephthalic acid, 12 mM benzoic acid) + 0.05 M H_2SO_4 or 0.1 M $HClO_4$ solutions (Chapter 4)

vi) 0.05 M $KClO_4$, pH = 7, 8.5 and 10 adjusted by addition of KOH (Chapter 5)

vii) 0.5 M $LiClO_4$, pH = 8.5 for tunneling spectroscopy experiments with viologens (Chapter 5).

3.3 STM-tip Fabrication

The fabrication of atomically sharp tips with small leakage currents is important for both STM imaging and STS experiments [63,64]. In the current work we employed tungsten and gold tips, both prepared by electrochemical etching procedures.

3.3.1 Tungsten tips

The electrochemical etching setup for the preparation of tungsten tips is shown in Fig. 3-2. The tungsten wire was anodically etched in 2 M NaOH solution in a lamella-arrangement using a Pt ring as a counter electrode employing a dc voltage of 2.7 V.

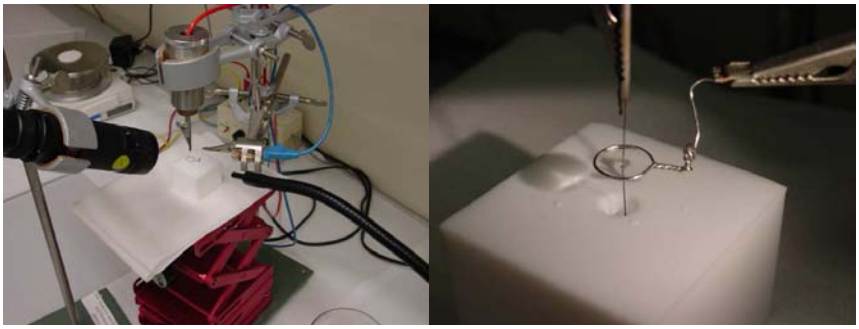

Fig. 3-2: Left: the setup for the electrochemical etching of a tungsten tip; Right: magnified assembly of tungsten wire, Pt-ring and lamella.

With the tungsten wire as anode, the latter becomes thinner and thinner in the contact region with the electrolyte lamella. Breaking of the wire is detected by a comparator, which ensures the immediate switching off of the applied voltage

(response time < 5 μs) ensuring an atomically sharp tip apex. Typical shapes of electrochemically etched tungsten tips are shown in the Fig 3-3.

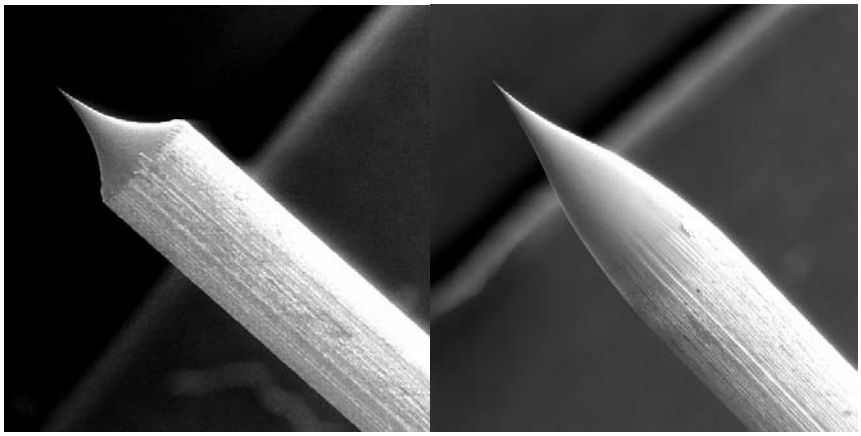

Fig. 3-3: TEM pictures of an upper (left) and a lower (right) uncoated tungsten tip.

3.3.2 Gold tips

The gold tips were etched employing an ac-procedure in a 1:1 or 2:3 mixtures of HCl (30%) and ethanol (98%). A graphite electrode served as a counter electrode. The gold wire, 0.25 mm in diameter, vertically dipped into the etching solution by about 1 mm, acted as an anode. Typical etching parameters are: 30-50 V ac voltage with a frequency of 3000-5000 Hz.

Both tungsten and gold tips were coated with polyethylene to decrease the contact area with the electrolyte or in other words to decrease faradaic current contributions to the tunneling current. The free areas of our coated STM tips range between 10^{-8} – 10^{-7} cm^2. The leakage current was typically less than 1-2 pA.

3.4 Instruments and Chemicals

3.4.1 Instruments

The STM experiments were carried out with a Molecular Imaging Pico-SPM which was positioned in a hermetically sealed container to prevent oxygen exposure of the samples. The STM-tips were electrochemically etched tungsten tips (0.25 mm diameter) or gold wires of 0.25 nm diameter coated with polyethylene. All STM

experiments were carried out at room temperature in constant current mode with tunneling currents ranging between 3 and 200 pA.

The electrochemical setup consists of a commercial AutoLab (PGSTAT-30) potentiostat employing single crystal cylinder electrodes in the so-called hanging meniscus configuration in a lab-built three-electrode electrochemical cell. Either a SCE or a MSE was used as reference electrode. A Pt wire served as counter electrode.

The SEIRAS experiments were carried out with a Bruker IF66 V/s Fourier Transform spectrometer synchronized with a Heka potentiostat PG 310 employing a vertical spectro-electrochemical cell in Kretschmann ATR-configuration. The spectrometer was operated in the slow-scan mode. For further details we refer to [60].

3.4.2 Chemicals

Except for the viologen molecules which were synthesized by the group of Prof. Marcel Mayor, University of Basel, all other molecules and chemicals were obtained commercially. The target molecules trimesic acid (TMA), isopthalic acid (IA) and benzoic acid (BA) were twice recrystallized with Milli-Q water. All electrolyte solutions for EC, SEIRAS and STM experiments were purged with argon to remove oxygen. The chemicals used are listed below:

Trimesic acid: for synthesis, Lancaster;

Isophthalic acid: for synthesis, Merck;

Terephthalic acid: for synthesis, Merck;

Benzoic acid: standard for element analysis, Merck;

Viologen derivatives: as synthesized, see reference [151] for details;

H_2SO_4: (for preparing caroic acid): 95 ~ 97 %, pro analysi, KMF;

H_2SO_4: (for preparing electrolyte solution): 96%, suprapure, Merck;

$HClO_4$: 70% solution, suprapure, Merck;

HCl: 30% solution, suprapure, Merck;

H_2O_2: (for preparing caroic acid): 30 or 35% (weight), puriss. stabilized, KMF;

NaOH: 30 % solution, suprapure, Merck;

$LiClO_4$: 99.99%, Aldrich;

KCl: 99.999%, suprapur, Merck;

$CaCl_2$: for analysis, Merck;

$KClO_4$: puriss. p.a., Fluka, twice recrystallized with Milli-Q water;

Ethanol: for analysis, KMF;

3.5 Specifics of the tunneling experiments

We have described above the basic preparation procedures and experiments employed in this dissertation. In the following we present specific aspects of single molecule STS experiments, which were carried out simultaneously with STM imaging studies (Chapter 5).

3.5.1 Molecular stretching in an EC STM configuration

Working in an electrochemical environment has the advantage that two potential differences can be controlled individually: the bias voltage between two working electrodes, and the potential drop between one working electrode and a reference electrode. The latter may be considered as a "gate electrode" as illustrated in Fig 3-4. An in situ STM set-up was applied to fabricate and to characterize electrical (and electrochemical) properties of single molecular junctions metal│molecule│metal between an STM tip and an appropriately modified substrate. This so-called "stretching method" was pioneered by Tao et al. [34] and by the Liverpool group [64,65] (cf. Fig. 3-4). We adopted this technique and introduced several modifications. The following sequence of steps was applied for studies under electrochemical conditions: Firstly, a gold tip (T) coated with polyethylene is brought to a predefined xyz - position and held at fixed bias $E_{bias} = E_T - E_S$. The distance (s_o) between the tip (T) and the adsorbate-covered gold substrate (S) is fixed by choosing a tunneling setpoint current i_o of 50 or 100 pA. After stabilization, the piezo feedback is disabled temporarily. The tip approaches the surface up to $s_o - \Delta s_a$ with certain rate, is held at this position for 100 ms, and subsequently retracted to $s_o + \Delta s_r$. The individual current–distance traces are recorded during the retraction process. Typical values of Δs_a and Δs_r were 1.1 and 2 nm. I_o and Δs_a were carefully selected to ensure strong tip-

adsorbate interactions. The strategy allowed the spontaneous formation of molecular bridges between the gold STM tip and the substrate surface, which were subsequently broken upon retraction. After enabling the feedback again, with the preset values of i_o, the surface was inspected by STM-imaging in constant current mode.

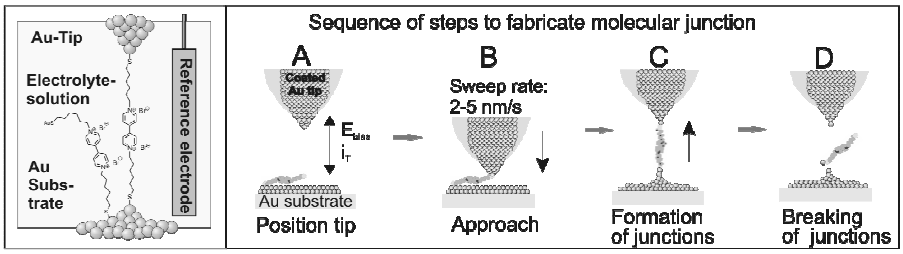

Fig. 3-4: (1) Redox-active viologens chemically bound to a Au substrate and a Au STM tip (left). The reference electrode works as gating electrode to tune the electron transfer through tailored molecules. (2) Illustration for the fabrication of molecular junctions by the stretching method in an in situ STM configuration (right).

3.5.2 Scanning tunneling spectroscopy

In combination with in situ STM experiments, we aim exploring the local electron transfer properties of redox-active thioalkyl-viologen derivatives. Two approaches were chosen: current-bias (i-E_{bias}) spectroscopy and current-overpotential (i-η) spectroscopy (cf. Chapter 5.5).

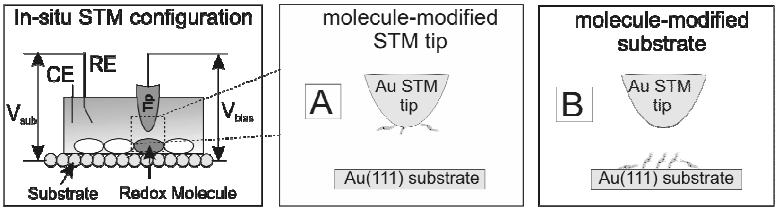

Fig. 3-5: (1) In situ STM configuration to explore local tunneling properties of viologens (left). (2) Illustration for the molecular tunnel junctions experiments with viologen-modified gold tip (A) and viologen-modified gold substrate (B).

The experiments started with the viologen-modified gold substrate or gold tip. After careful mounting and stabilization in the STM setup, the tunneling regime was established with a setpoint current i_o of about 100 pA and a bias voltage E_{bias} = 0.100 V (Fig. 3-5). After equilibration, the piezo feedback was switched off, and several current–voltage traces were recorded either at fixed bias (E_T – E_S) by sweeping

simultaneously the potentials of tip (E_T) and substrate (E_S) or at fixed sample potential (E_S) by sweeping E_{bias}. Individual scans consisting of 1000 data points were recorded. The cycle was repeated after stabilization at the preset value of i_o.

Chapter 4. Supramolecular Assembly of TMA and Its Related Molecules

4.1 General

4.1.1 TMA – a model system

Trimesic acid (TMA, 1,3,5-benzene-tricarboxylic acid) represents a prototype system for supramolecular self-assembly. The molecular structure of TMA is shown in Scheme 4-1. It represents a polyfunctional carboxylic acid with 3-fold symmetry comprising a phenyl ring and three identical carboxyl endgroups in the same plane [66]. The carboxyl groups of TMA are well-known to form intermolecular hydrogen bonds, such as the dimer illustrated in Scheme 4-1. This motif is called synthon in crystal engineering and often used as structure-controlling element in molecular fabrication processes. An example is the honeycomb assembly (Scheme 4-1), which is composed of three hydrogen-bonded dimers. The potential to form diverse supramolecular structures makes TMA a unique candidate in 2D self-assembly on surfaces and interfaces.

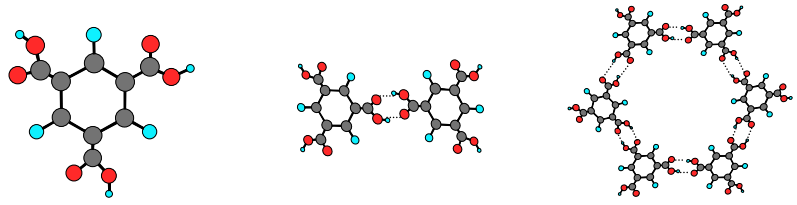

Scheme 4-1: Hydrogen-bonded supramolecular structures of trimesic acid.

4.1.2 STM studies of TMA and our approach

TMA has been used as unique building block to create a variety of 2D molecular nanoscale structures, which were investigated by scanning tunneling microscopy (STM) under different experimental conditions [66,67,68,69,70]. Molecular self-assembly at surfaces is governed by the subtle balance between intermolecular and molecule–surface interactions, which can be tuned by the substrate material and its symmetry, the temperature or, at electrified interfaces, by the applied electrode potential. Dmitriev et al. [66] reported on Cu(100) at low temperatures (~ 200 K) the existence of 2D ordered adlayer islands composed of a honeycomb structure of TMA molecules in a planar orientation. Barth et al. also explored the molecular assembly of metal–organic coordination networks of TMA and related aromatic carboxylic acids on well-defined metal surfaces in ultrahigh vacuum [70]. Griessl et al. [67] reported on HOPG (Highly Ordered Pyrolytic Graphite) at 25 K up to room temperature the coexistence of two hexagonal ring structures composed of TMA with hydrogen bonds formed between either two (honeycomb pattern) or three (flower structure) adjacent molecules.

Alternatively, the adsorption-triggered self-assembly of TMA can be explored on well-defined conducting surfaces in an electrochemical environment [60,68,69,71]. This approach offers the advantage, in comparison to a UHV-based environment, that formation, properties and structural transitions of a wide variety of 2D supramolecular adlayers can be tuned by the applied electrode potential, and subsequently characterized by structure-sensitive in situ techniques in real space and real time [51,72]. Ishikawa et al. reported for Au(111)/0.1 M $HClO_4$ a honeycomb-type (8 x 8) 2D network of flat-oriented TMA molecules, which transforms at higher potentials into a close-packed structure of TMA dimers [68]. Under rather similar experimental conditions, Su et al. found three distinctly different TMA adlayers [69] at different sample potentials.

Despite these rather detailed experimental results no molecular-level understanding on the kinetic process of the phase formation and/or stability of TMA adlayers on Au(111) electrode has emerged yet. This motivated us to carry out a comprehensive electrochemical in situ STM and spectroscopic study on steady state patterns and the dynamics of potential-induced supramolecular ordering of TMA

adlayers on Au(111)-(1 x 1) and Au(111)-(p x √3) surfaces [60]. Most of the work in this dissertation was carried out on Au(111) substrate in 0.05 M H_2SO_4 solution. Therefore we start with the presentation of the phase behavior of a Au(111) electrode in sulfuric acid without specifically adsorbed molecules or redox species.

The chapter is organized as follows: First, we show experimental data of Au(111) in sulfuric acid as obtained by cyclic voltammetry and in situ STM. Then we report on the electrochemical characteristics of trimesic acid on Au(111)-(1x1) and Au(111)-(p×√3) in 0.05 M H_2SO_4. In the third section steady-state properties of potential-dependent adlayers of trimesic acid on Au(111) will be presented. Finally, the kinetic aspects of adlayer formation processes will be explored, and selected details of structural transition will be reported.

4.2 Electrochemical Data of TMA

4.2.1 Au(111) in 0.05 M H_2SO_4

Fig. 4-1 shows a typical voltammogram of Au(111) in 0.05 M H_2SO_4 solution in -0.300 V ≤ E ≤ 1.350 V. The STM images illustrate the morphology of the gold surface in different potential ranges.

The experiment starts with the immersion of a flame-annealed Au(111)-electrode in the electrolyte under potential control at -0.20 V. The voltammogram shows three pairs of current peaks named P1/P1', P2/P2', and OA(1,2)/OC, corresponding to the substrate surface transition (lifting of the reconstruction), the formation/dissolution of the (√3 x √7) (hydrogen-) sulfate overlayer and the reduction/oxidation of the gold surface. Fig. 4-1 A shows a freshly prepared flame-annealed Au(111)-(p x √3) surface. The thermally-induced reconstruction lines with the characteristic zig-zag pattern are clearly resolved. Scanning the electrode potential in positive direction, passing the current peak P1, around the potential of zero charge (PZC) [73,74], results in the lifting of the surface reconstruction. A uniformly unreconstructed Au(111)-(1x1) surface is obtained (Fig. 4-1 B). The disorder/order transition of adsorbed sulfate ions takes place around 0.80 V as shown in Fig. 4-1 C, in which the left half of the image represents the atomic gold surface and the right half shows the ordered √3 x √7 sulfate adlayer. Further increase of the electrode potential

to 1.35 V causes the oxidation of the gold surface (Fig. 4-1 D), which correlates with the current peak OA2. Scanning the electrode potential towards negative values (passing OC1) causes the reduction of the oxidized surface, which is often accompanied by the formation of monatomically deep holes. Most of the experiments in this thesis were carried out on the unreconstructed Au(111)-(1 x 1) surface (Fig. 4-1 B). Some data will be also reported on the reconstructed surface (Fig. 4-1 A).

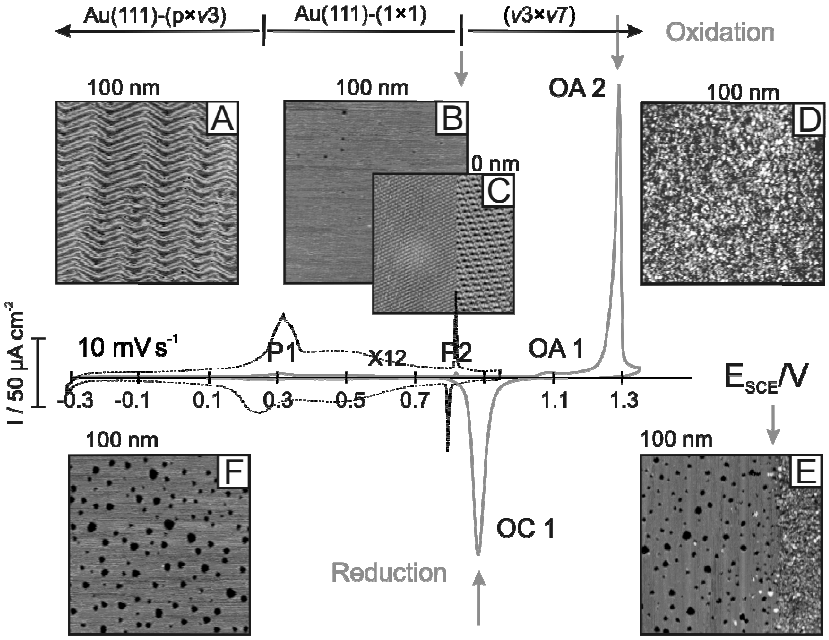

Fig. 4-1: Cyclic voltammogram of the Au(111) electrode in 0.05 M H_2SO_4, scan rate 10 mV s^{-1}. The dotted curve represents a magnification (factor 12) of the double layer region. The in situ STM images represent the surface structures at various potentials: (A) Thermally reconstructed Au(111)-(px√3) surface, E = -0.200 V, (B) Au(111)-(1x1) surface after the reconstruction was lifted, (C) Transition between the disordered and the ordered sulfate overlayer (√3 x √7), (D) Oxidized gold surface, (E) Transformation of the oxidized gold surface upon a negative-going potential scan, (F) Gold surface with monoatomic deep holes obtained after 5 subsequent oxidation/reduction cycles.

4.2.2 Au(111) in H_2SO_4 + TMA

Fig. 4-2 A shows a typical current vs. potential curve of Au(111)-(1 x 1) in 0.05 M H_2SO_4 in the absence (dashed line) and in the presence of 3 mM TMA recorded with a scan rate of 10 mV s^{-1}. Under these conditions TMA is completely protonated (pK_1 = 2.1, pK_2 = 4.1, pK_3 = 5.18) [75].

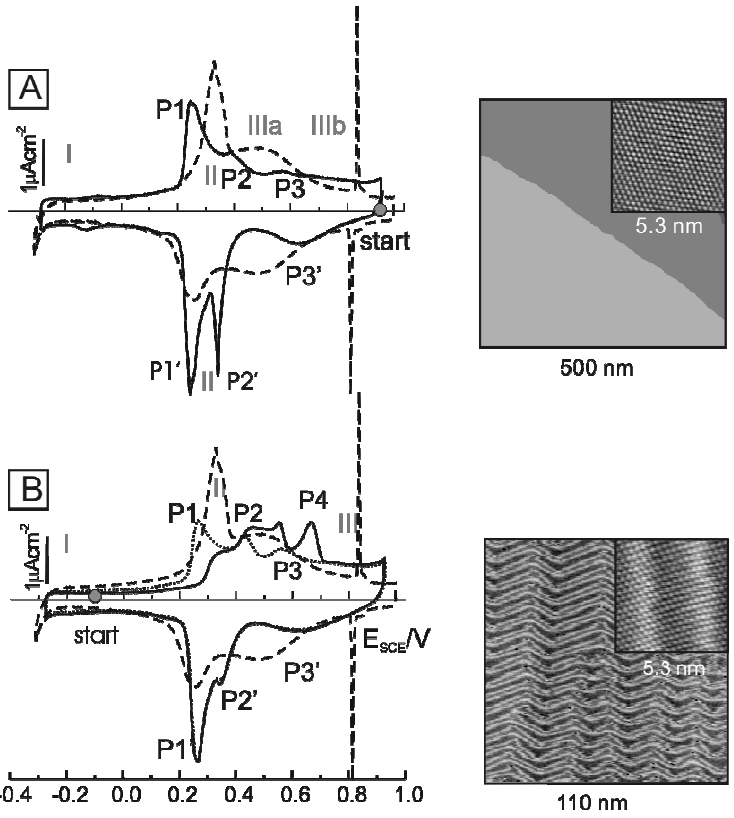

Fig. 4-2: Cyclic voltammograms for gold electrodes in 0.05 M H_2SO_4 in the absence (dashed lines) and in the presence of 3 mM TMA (full lines and dotted lines), scan rate 10 mV s^{-1}. (A) Au(111)-(1x1); (B) Au(111)-(p×√3). The dotted traces represent the steady-state curves recorded after three complete potential cycles. The inserted panels represent large-scale and atomic-resolution in situ STM images of the gold surfaces recorded at the respective starting potentials.

The experiment started at 0.90 V with an unreconstructed, island-free surface, which was prepared by flame-annealing and subsequent electrochemical annealing in 0.1 M HCl [76]. The solid trace represents the first negative-going voltammetric cycle in the double layer region. Four characteristic potential regions (labeled I, II, IIIa and IIIb in a sequence from negative to positive potentials), which are separated by the current peaks P1 | P1´, P2 | P2´ and P3 | P3´, can be readily distinguished. The stability range of I is delimited at negative potentials by the onset of hydrogen evolution, and at positive potentials by the current peaks P1 | P1´. After a narrow region II (between P1 | P1´ and P2 | P2´), which is strongly dependent on scan rate

and surface preparation, a broad current minimum develops in region IIIa. At more positive potentials, past the broad peak P3, a low-capacitance region IIIb is found. Upon increasing the potential further, the stability range of IIIb is delimited by the competing adsorption of OH^- and the onset of gold oxidation.

When starting the experiment at -0.10 V, i.e. at negative charge densities with a freshly flame-annealed, reconstructed Au(111) - (p x √3) surface, a different voltammetric profile is obtained (Fig. 4-2 B). The first cycle (solid line) illustrates that P1 and P2 degenerate into shoulders, a new peak P4 appears. Upon changing the direction of the potential scan toward negative values P1´ and P2´ broaden and nearly merge indicating the decrease of the stability range of II. Further cycling of the potential (dotted line in Fig. 4-2 B) leads to distinct peaks P1, P2 and P3 in the positive-going scan direction. P4 disappears. No significant differences between the first and subsequent potential cycles were found in the trace representing the negative-going scan direction. We notice that the shape of the current–potential curves recorded after multiple cycles with 10 mV s^{-1} in the double layer region are not dependent on starting the experiment either with a freshly prepared Au(111)-(1 x 1) or with a reconstructed Au(111)-(p x √3) surface.

The cyclic voltammograms of 3 mM TMA in 0.05 M H_2SO_4 (this work) and 0.1 M $HClO_4$ [60] are rather similar, except that the interfacial capacitances in regions IIIa and IIIb are slightly higher in sulfate-containing electrolyte, which is attributed to anion coadsorption in the Helmholtz region.

4.3 In situ STM study of TMA: Steady state

4.3.1 Overview

Steady state in situ STM measurements were performed to explore structural details of the various stages of the electrochemical experiment. A carefully prepared unreconstructed Au(111)-(1 x 1) electrode was brought in contact with an electrolyte containing 0.05 M H_2SO_4 and 3 mM TMA under potential control at various potentials (Fig. 4-2 A). Five distinctly different supramolecular adlayer motifs were observed depending on the applied potential and the assembly conditions (Fig. 4-3). Three long-range ordered adlayer structures were found in region I, which we shall

label honeycomb (structure Ia), ribbon-type (structure Ib) and herringbone-type (structure Ic) pattern. Region II is composed of strongly correlated chains of linear rows with characteristic translational domain boundaries (Fig. 4-3 II). No ordered pattern was found at potentials between the current peaks P2 | P3 and P2´ | P3´. A striped phase with a rather regular variation in the STM contrast appears at E > P3 (P3´) in the potential region IIIb. Structural details of the five ordered TMA adlayers will be discussed next.

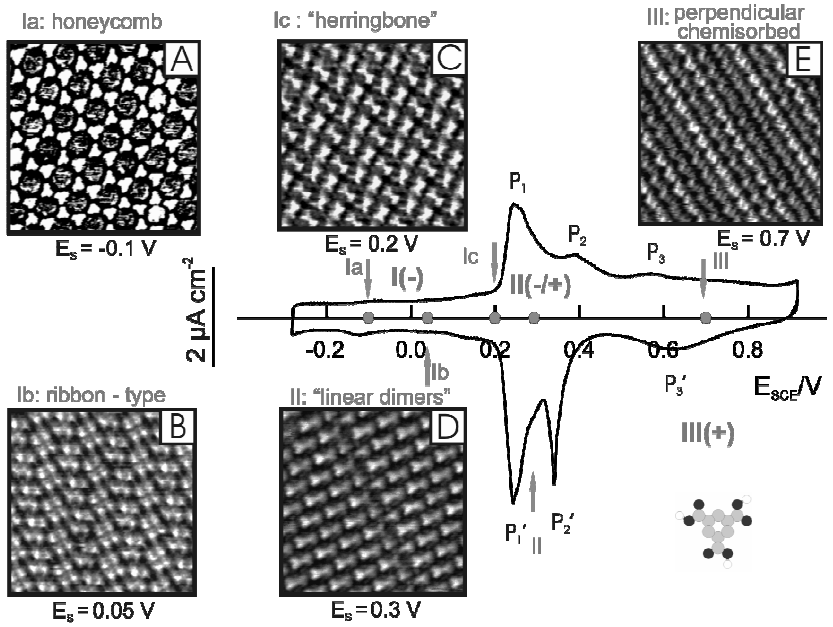

Fig. 4-3: Steady-state voltammogram for Au (111) | 0.05 M H_2SO_4 in the presence of 3 mM TMA. The stability regions of the various adlayer phases are labeled Ia, Ib, Ic, II, III and are illustrated with typical in situ STM images: (Ia) hexagonal honeycomb phase, E_S = -0.100 V; (Ib) ribbon-type motif, E_S = 0.050 V; (Ic) herringbone motif, E_S = 0.200 V; (II) hydrogen-bonded linear dimers, E_S = 0.300 V; (III) ordered chemisorbed striped phase of TMA at E_S = 0.700 V. All images represent a (10 nm x 10 nm) frame.

4.3.2 Planar oriented TMA in phase I and II

Hexagonal honeycomb phase Ia

Depositing TMA (c > 0.2 mM) from sulfuric acid solution on Au(111)-(1 x 1) at potentials more negative than 0.00 V, i.e. at a negatively charged electrode surface, gives rise to large domains (> 100 nm) of a long-range ordered honeycomb pattern.

The later represents a hexagonal network with equal-sized cavities. The rarely observed domain boundaries appear frizzy and do not strictly follow characteristic symmetry directions of the underlying Au(111) substrate surface indicating a high mobility of TMA monomers and rather weak adsorbate–substrate interactions. Once formed, the TMA adlayer Ia is stable until the onset of hydrogen evolution at E < -0.300 V, and at positive potentials up to the current peak P1 (Fig. 4-3). High resolution in situ STM images (Fig. 4-4 B) reveal that the honeycomb pattern is composed of six bright, separately resolved triangular features, which are assigned to individual TMA molecules, and a dark depression in the center of the assembly. Their triangular contrast pattern with a characteristic side length of $l \approx 0.7$ to 0.8 nm and the comparison with the molecular structure of TMA [77] suggest a planar surface orientation. The positions of the symmetrically arranged carboxyl groups in individual TMA molecules are clearly resolved. Adjacent carboxyl groups of each two neighboring TMA units appear to be aligned. Cross-section profiles (Fig. 4-4 C) reveal an apparent corrugation height of the bright spots ranging between 0.10 and 0.15 nm, and a value of 0.05 nm for the 1.2 nm in diameter dark, but somewhat streaky hole in the center. The former represent typical values for physisorbed, planar-oriented aromatic molecules with the π – system of the phenyl ring oriented parallel to the substrate surface [78-82]. The planar orientation of TMA in potential region I is also supported by the results of our recent ATR-SEIRAS study [60].

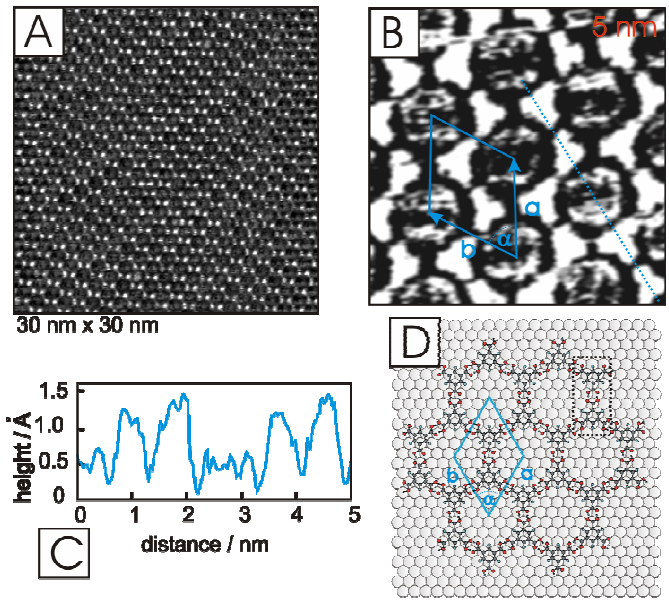

Fig. 4-4: (A) Large-scale in situ STM image of the hexagonal honeycomb phase Ia of TMA on Au(111) | 0.05 M H_2SO_4 in the presence of 3 mM TMA, E_S = -0.100 V, i_T = 70 pA. (B) High-resolution STM image of (A), E_S = -0.100 V, i_T = 70 pA. The primitive unit cell is indicated. (C) Cross-section profile along the cut indicated in (B). (D) Proposed packing model. The parameters of the unit cell are summarized in Table 4-1.

The highly symmetrical motif shows a characteristic repeat distance of (1.70 ± 0.08) nm. The experimentally determined rhombohedral unit cell with a = b = (1.70 ± 0.08) nm and α = (60 ± 5)^o is composed of two TMA molecules and gives rise to a coverage Γ_{Ia}(ex) = (1.3 ± 0.1)×10^{-10} mol cm^{-2} (Fig. 4-4 B, D). These data correspond to A_{Ia}(ex) = (1.25 ± 0.10) nm^2 as approximate area per molecule (Table 4-1). The registry between adlayer and substrate could not be determined unambiguously in our experiments. However, the characteristic lengths of the unit cell vectors are close to six times the gold diameter (6 x $|a_{Au}|$ = 1.73 nm). Based on literature data [80,82,83], we propose that the aromatic phenyl rings of the TMA molecule are preferentially bound to high symmetry threefold hollow sites of the substrate lattice. This assumption suggests a nearly perfect alignment of the (6 x 6) honeycomb – type TMA adlayer to adjacent [110] symmetry directions of the substrate surface. Using vectors of the primitive gold lattice, a_{Au} and b_{Au} (Fig. 4-4 D) with $|a_{Au}| = |b_{Au}|$ = 0.2885 nm

as basis one obtains in matrix notation: $\begin{pmatrix} a \\ b \end{pmatrix} = \begin{pmatrix} 6 & 6 \\ 0 & 6 \end{pmatrix} \begin{pmatrix} a_{Au} \\ b_{Au} \end{pmatrix}$. The parameters of the corresponding unit cell are summarized in Table 4-1.

Table 4-1: Characteristic dimensions of the unit cell parameters of the various ordered adlayers investigated for Au(111) in 0.05 M H_2SO_4 + 3 mM TMA.

adlayer	a [nm]	b [nm]	α [°]	area A per molecule [nm^2]	coverage Γ 10^{-10} mol cm^{-2}
honeycomb Ia	1.70 ± 0.08 *1.73*	1.70 ± 0.08 *1.73*	60 ± 5 *60*	1.25 ± 0.10 *1.30*	1.3 ± 0.1 *1.3*
ribbon-type Ib	3.57 ± 0.20 *3.6*	1.92 ± 0.10 *2.02*	80 ± 5 *76*	0.84 ± 0.05 *0.88*	2.0 ± 0.1 *1.9*
herringbone Ic	3.30 ± 0.15 *3.25*	4.10 ± 0.15 *4.04*	84 ± 5 *87.5*	0.75 ± 0.05 *0.73*	2.2 ± 0.2 *2.3*
linear dimers II	1.43 ± 0.05 *1.44*	1.18 ± 0.05 *1.15*	63 ± 5 *60*	0.75 ± 0.02 *0.72*	2.2 ± 0.1 *2.3*
chemisorbed striped phase IIIb	0.86 ± 0.05 *0.865*	2.15 ± 0.20 *2.00*	86 ± 8 *90*	0.46 ± 0.05 *0.43*	3.6 ± 0.4 *3.8*

The experimentally determined values are plotted in the first line of each row. The second line (italics) represents the parameter of the theoretical model suggested upon considering the registry between substrate surface and adlayer.

The open six-fold honeycomb structure with a 1.2 nm diameter “hole” in the center of the ring may act as a nanoscale host system with predefined sites for guest molecules [67,84,85,86]. The formation of size-selective inclusion complexes may significantly increase the packing stability of the hydrogen-bonded pattern. In aqueous electrolyte and in the absence of specific adsorption of anions the cavities appear streaky (Fig. 4-3 A, Fig. 4-4 B). These observations are attributed to the high mobility and/or transient adsorption of either water or solute molecules [87]. This interpretation is supported by the absence of similar features in TMA adlayers prepared in UHV [66,67]. Increasing the solution concentration of TMA above 1 mM allows incorporating individual, flat-lying physisorbed TMA molecules having a finite residence time in the organic host lattice (Fig. 4-5). The guest species appear

disk-like with an apparent corrugation of approximately 0.10 to 0.15 nm. No triangular features were resolved.

The size and shape of the TMA guest molecules indicate no specific interaction, such as directional hydrogen bonds, with the host skeleton. Their smeared-out appearance, in comparison to the regular triangular shape of the two-dimensional host lattice molecules, may indicate a rotation of the TMA guest being significantly faster than the acquisition time of the STM image. A similar interpretation was suggested for coronene incorporated into a TMA host lattice [85].

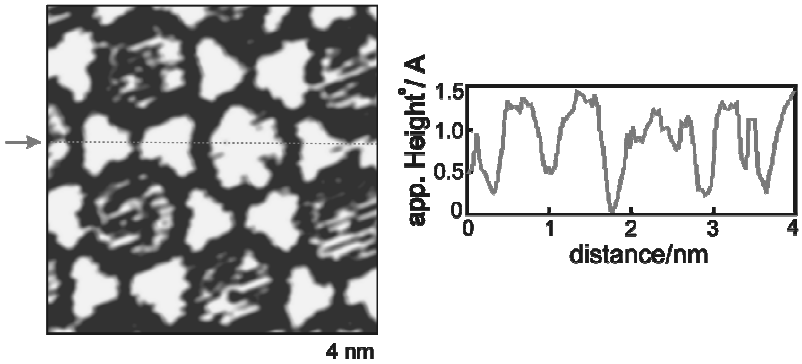

Fig. 4-5: TMA guest molecule positioned in the center of a honeycomb hexagonal TMA host lattice, E_S = -0.10 V, i_T = 70 pA. The line scan represents a typical cross-section profile.

Ribbon-type motif Ib

Depositing TMA from aqueous electrolyte at higher concentrations (c > 1.0 mM) under potential control in 0.00 V < E < 0.20 V reveals large domains of a new two-dimensional assembly pattern of TMA on Au(111)-(1 x 1) and Au(111)-(p x$\sqrt{3}$) (Fig. 4-6 A, B). One identifies alternating parallel rows of squares and rhombohedral motifs. Each subunit is composed of four bright spots, which are assigned to individual flat-lying TMA molecules. High-resolution images (Fig. 4-6 B) illustrate their regular shape, and an apparent corrugation height of 0.10 to 0.15 nm. The nearest neighbor distance of the square motif within one row is estimated to b = (1.92 ± 0.10) nm, and between two adjacent rows of squares to a = (3.57 ± 0.20) nm. The enclosed angle α amounts to (80 ± 5)^o. The derived unit cell, as drawn in Fig. 4-6 C, contains eight individual, flat-lying TMA molecules, which are arranged in alternating rows of

quadratic tetramer motifs and parallel dimers in rhombohedral subunits. The area per molecule is estimated to $A_{Ib}(ex) = (0.84 \pm 0.05)$ nm^2, which corresponds to a coverage $\Gamma_{Ib}(ex) = (2.0 \pm 0.1)\times10^{-10}$ mol cm^{-2}.

Adjacent dimers appear to be aligned with the upper right and the upper left, and the lower right and the lower left TMA molecules in the squared sub-motif at each corner. The tetramer arrangement is attributed to the formation of a hydrogen-bonded closed loop between four carboxyl groups of one unit. Similar motifs were reported for the crystal structures of chloroacetic acids [88], and for the self-assembly of 5,10,15,20-tetrakis-(4-carboxylphenyl)-21H,23H-porphyrin (TCPP) on HOPG [89]. The suggested tetrameric configuration of TCPP was attributed to a compromise between optimal intermolecular hydrogen bonding, maximization of 2D packing and substrate–adsorbate interaction to minimize surface free energy [89,90]. Crystallographic studies show that the tetramer close-loop motif of carboxylic groups is stabilized by incorporation of water molecules or short-chain alcohols [91,92,93].

We did not succeed in deriving the registry between the ribbon-type adlayer Ib and the unreconstructed Au(111)-(1 x 1) surface from direct experimental imaging. However, we did find that, within the experimental accuracy, TMA molecules form an identical structure on the reconstructed Au(111)-(p x √3) surface in a similar potential range (Fig. 4-3, Fig. 4-6 A). These experiments illustrate that the quadratic tetramer motifs are aligned with the $[11\bar{2}]$ and the $[1\bar{1}0]$ directions of the substrate surface.

Combining the experimental results that molecules are oriented flat with the properties of the 2D ordered molecular network, we propose the model depicted in Fig. 4-6 C for the adlayer Ib. Using vectors of the primitive gold lattice, a_{Au} and b_{Au}, one obtains in matrix notation $\begin{pmatrix} a \\ b \end{pmatrix} = \begin{pmatrix} 10 & -4 \\ 7 & 7 \end{pmatrix} \begin{pmatrix} a_{Au} \\ b_{Au} \end{pmatrix}$. The model shows typical lengths and angles of intermolecular hydrogen bonds, and nearly all TMA molecules of the unit cell occupy threefold substrate coordination sites. The model is in good agreement with the results derived from the experimental images (Table 4-1, Fig. 4-6 C).

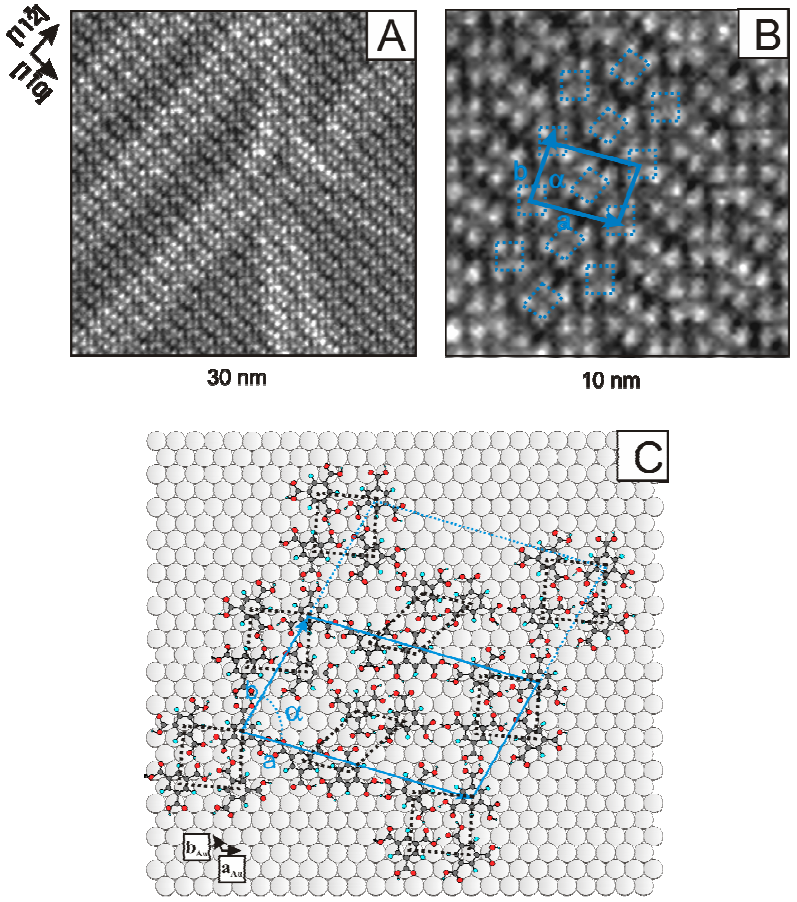

Fig. 4-6: (A) Large-scale in situ STM image of the ribbon-type motif Ib of TMA on Au(111)-(p x √3) | 0.05 M H_2SO_4 in the presence of 3 mM TMA, E_S = 0.030 V, i_T = 150 pA. (B) High-resolution image of Ib. The unit cell and the characteristic lattice directions on Au(111)-(1 x 1), E_S = 0.000 V, i_T = 160 pA The characteristic quadratic and rhombohedral structural elements as well as the primitive unit cell are indicated. (C) Proposed packing model of TMA in Ib.

Herringbone motif Ic

Transient desorption of the ribbon-type motif Ib upon excursion to positive potentials and immediate return to potentials around 0.200 V, i.e. just negative of the capacitive current peak P1´, allows to create a new two-dimensional assembly of TMA (Fig. 4-3, Fig. 4-7). High-resolution images reveal a regular arrangement of dimers composed of two triangular units with typical properties of planar oriented TMA molecules (side length ~ 0.7 to 0.8 nm, apparent corrugation height of (0.10 ±

0.02) nm). The length of one dimer-type unit in the STM contrast pattern along the main axis is estimated to (1.4 ± 0.2) nm. These observations and the comparison with the honeycomb motif Ia described before indicate that the dimers are stabilized by centrosymmetric hydrogen bonds between two carboxyl groups of adjacent TMA molecules.

Here, we define two adlayer directions by introducing the vectors $\vec{a}'$ and $\vec{b}'$ (Fig. 4-7). Individual dimers are arranged with their main axis either parallel (represented by "—") or perpendicular (represented by "|") to the introduced adlayer directions. Parallel to the lattice vector $\vec{a}'$ the one-dimensional assembly of TMA dimer units follows the motif "… —| |—| |—…". Parallel to $\vec{b}'$ we identify the motif "…—|—— —|— —|—…". The careful inspection of high-resolution STM images demonstrates that the assembly of the four dimers "—| |—" along $\vec{a}'$ and of "|— —|" along $\vec{b}'$ identifies the unit cell of the herringbone-type TMA adlayer Ic. The characteristic dimensions along $\vec{a}'$ and $\vec{b}'$ are estimated as a = (3.30 ± 0.15) nm, b = (4.10 ± 0.15) nm separated by an angle α = (84 ± 5)^{o}. The complex unit cell is formed by eighteen TMA molecules arranged in a regular 2D pattern of centrosymmetric dimers. The area per molecule A_{Ic}(ex) = (0.75 ± 0.05) nm^2, and the resulting coverage is given by Γ_{Ic}(ex) = (2.2 ± 0.2) 10^{-10} mol cm^{-2} .

A tentative model of the adlayer Ic assumes that the phenyl rings of the TMA molecules are preferentially located in or nearby high-symmetry sites of the hexagonal Au(111)-(1 x 1) substrate. Taking the latter assumption, the properties of the experimentally derived unit cell, and the geometrical restrictions for dimer, trimer respective tetramer hydrogen bonding assemblies [89,90], we propose the model drawn in Fig. 4-8 for the herringbone-type TMA phase Ic. With the primitive vectors of gold lattice, a_{Au} and b_{Au} one obtains in matrix notation $\begin{pmatrix} a \\ b \end{pmatrix} = \begin{pmatrix} 14 & 0 \\ 7 & 13 \end{pmatrix} \begin{pmatrix} a_{Au} \\ b_{Au} \end{pmatrix}$.

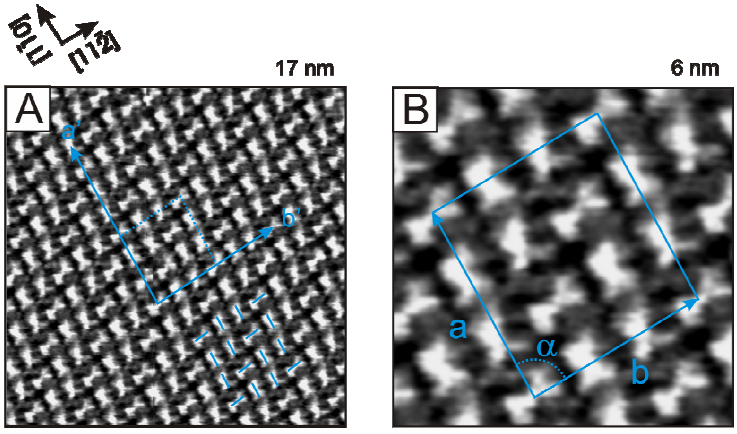

Fig. 4-7: (A) Large-scale in situ STM image of the herringbone-type motif Ic of TMA on Au(111)-(1 x 1)|0.05 M H_2SO_4 in the presence of 3 mM TMA, E_S = 0.200 V, i_T = 270 pA. The lattice vectors $\vec{a}'$ and $\vec{b}'$ are indicated. (B) High-resolution image of Ic on Au(111)-(1 x 1), E_S = 0.180 V, i_T = 120 pA. The experimental unit cell is outlined.

The tentative assignment is supported by estimations based on molecular modeling with ChemDraw Pro. The model implies a compromise between intermolecular interactions due to hydrogen bonding and adsorbate–substrate interactions to minimize the surface free energy. It is in agreement with the properties of the experimentally observed unit cell (Table 4-1 summarizes the comparison of the parameters), and maximizes the number of flat oriented TMA molecules localized in or close to high coordination, threefold hollow sites of the Au(111) surface. The model proposes that the $\vec{a}'$ direction of the unit cell is aligned with the $[1\bar{1}\,0]$ substrate direction. The $\vec{b}'$ vector is misaligned by 2.5° with respect to the $[11\bar{2}]$ direction of Au(111). The experimentally observed "—| |—" and "|——|" motifs are clearly recognized as subunits of the model structure. The lengths of the hydrogen bonds OH···O in the dimer units are typically (0.26 ± 0.01) nm with bond angles of (180 ± 5)°. The lengths of the hydrogen bonds in the three-mer and four-mer units appear elongated up to 0.30 nm with estimated angles varying between 150° and 180°.

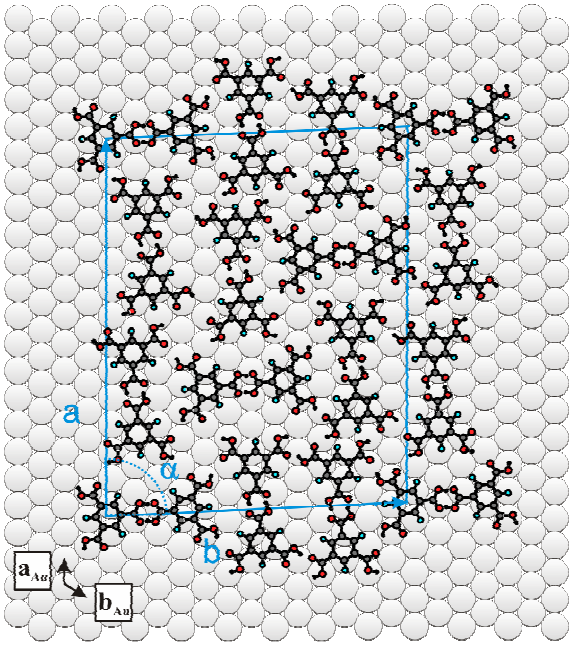

Fig. 4-8: Proposed packing model of TMA in Ic. The substrate - adsorbate registry is chosen with the assumption to maximize the number of phenyl rings in or close to high symmetry positions of the substrate lattice. The parameters of the unit cell are summarized in Tab. 4-1.

The herringbone structure Ic dissolves at positive potentials when passing the current peak P1´ in the cyclic voltammograms (Fig. 4-3). On the other hand, it is stable at negative potentials until $E \leq -0.20$ V.

Hydrogen bonded dimer motif II

The potential-controlled deposition of TMA in $0.20\ V \leq E \leq 0.40\ V$, i.e. in the range marked by the current peaks P1 | P1´and P2 | P2´ in the cyclic voltammograms (Fig. 4-3) triggers the assembly of TMA dimers in quasi-linear rows. The field in the electric double layer is expected to be small because the electrode bears a rather low excess charge in this potential region [60]. The new adlayer emerges from an initially disordered phase, which slowly transforms into large two-dimensional islands of the assembly motif II. Characteristic translational (Fig. 4-9 A) and rotational (Fig. 4-9 B) domain boundaries were found. Occasionally we found kink sites causing steps and a rotation of the domain boundary by 45^o (Fig. 4-9 A). Identical adlayer structures were detected on Au(111)-(1 x 1) and Au(111)-(p x $\sqrt{3}$). The latter studies indicate that translational domain boundaries often extend over several tens of nanometers and are closely aligned to the $[11\bar{2}]$ direction of the substrate. The width of the corresponding

domains in [$1\bar{1}0$] direction is determined by two up to ten characteristically shaped protrusions aligned in parallel, and highly correlated one-dimensional chains.

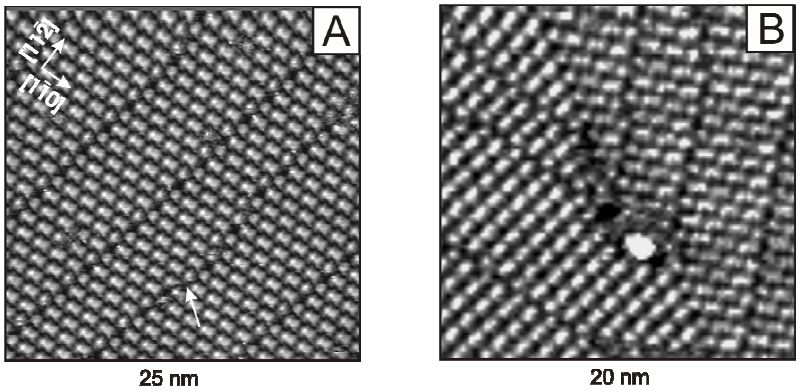

Fig. 4-9: (A) Translational and (B) Rotational domain boundaries in a large-scale in situ STM image of the hydrogen-bonded dimer motif II of TMA on Au(111)-(1 x 1) | 0.05 M H_2SO_4 in the presence of 3 mM TMA, E_S = 0.330 V, i_T = 111 pA. The arrow in (A) marks a characteristic kink site at a translational domain boundary.

Closer inspection (Fig. 4-10 A) reveals that the characteristic protrusions are composed of two triangular features with the typical properties of a planar oriented TMA molecule (side length 0.7 to 0.8 nm, apparent corrugation height (0.08 ± 0.01) nm). Assigning the corners of the triangular spots to the positions of the three carboxyl groups in individual TMA molecules we conclude on the existence of hydrogen-bonded centrosymmetric TMA dimers. Dimers within one chain and of the entire two-dimensional domains point in the same direction. The centers of these dimers are aligned with the [$1\bar{1}0$] lattice direction. The center-to-center separation is estimated to a = (1.43 ± 0.05) nm ≈ 5 x $|a_{Au}|$. Moreover, the molecular axis of individual TMA dimers is rotated by $\beta = (5 \pm 2)^o$ with respect to the chain direction (Fig. 4-10 A). Linear chains of dimers are separated by an inter-row distance of (1.05 ± 0.04) nm. The nearest neighbor distance between the dimer centers of adjacent rows is estimated to (1.18 ± 0.05) nm ≈ 4 x $|a_{Au}|$.

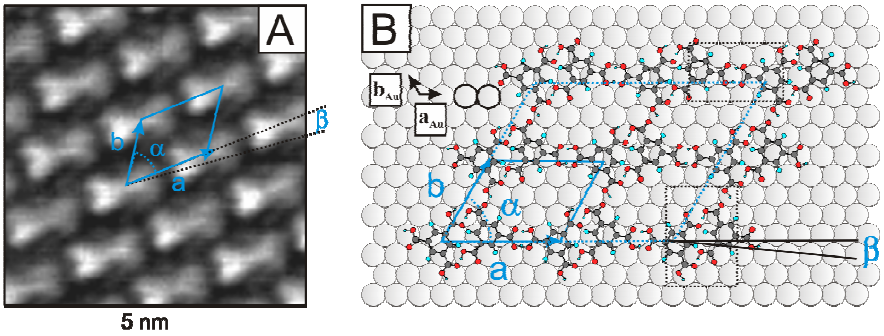

Fig. 4-10: (A) High-resolution STM image of phase II on Au(111)-(1 x 1), E_S = 0.300 V, i_T = 200 pA. The primitive unit cell is indicated. (B) Proposed packing model of TMA in II. The parameters of the unit cell are summarized in Table 4-1.

The derived unit cell, which contains two TMA molecules, is indicated in Fig. 10 B (Tab. 4-1). The corresponding area per molecule and coverage were estimated to $A_{II}(ex) = (0.75 \pm 0.02)$ nm^2 and $\Gamma_{II}(ex) = (2.2 \pm 0.1)\ 10^{-10}$ mol cm^{-2}, respectively. The experimental observations can be rationalized by the directional nature of hydrogen bonds. Molecular modeling reveals that the regular arrangement of dimers within one linear row may involve hydrogen-bonded macrocyclic dimers formed between four carboxyl groups of two adjacent TMA units. This motif is known to support the assembly of TMA in planar sheets in three-dimensional supramolecular assemblies [94]. Adjacent TMA molecules of the one-dimensional chains appear to be connected by hydrogen bonds in an alternating arrangement of centrosymmetric and macrocyclic dimers. Single hydrogen bonds may exist between molecules of parallel rows. This hypothesis is supported by the observation that the positions of dimers within one domain appear to be very stable and not frizzy and highly correlated [87]. Neighboring molecular rows at translational domain boundaries are not in registry. They are in interstitial positions and contain, in an alternating arrangement, TMA monomers with a broken centrosymmetric hydrogen bond.

The experimentally observed registry between the linear dimer motif II and the substrate surface suggests a commensurate (5 x 4) TMA adlayer structure. The commensurability of the molecular adlayer II with respect to the substrate is further supported by the absence of long-range corrugations indicative of a Moiré or dislocation pattern. Using vectors of the primitive gold lattice one obtains in matrix

notation $\begin{pmatrix} a \\ b \end{pmatrix} = \begin{pmatrix} 0 & 5 \\ 4 & 4 \end{pmatrix} \begin{pmatrix} a_{Au} \\ b_{Au} \end{pmatrix}$. We further assume that the phenyl rings of the TMA molecules are located in threefold hollow sites of Au(111). The corresponding model, depicted in Fig. 4-10 B, is in agreement with all experimental observations and gives reasonable values for the OH···O bond lengths and angles of the suggested hydrogen-bonded assembly (Table 4-1). We notice that the substrate–adsorbate interaction reduces the distance between the TMA centers of one centrosymmetric dimer by approximately 10 %. The model predicts further the misalignment of the dimer axis by -5° with respect to the $[1\bar{1}0]$ substrate direction, which results from the directional nature of hydrogen bonds in the alternating arrangement centrosymmetric and macrocyclic dimers.

4.3.3 Upright oriented TMA – phase III

Increasing the electrode potential to higher positive values, i.e. past the current peak P2 in Fig. 4-3, causes the transformation of phase II previously assigned to hydrogen-bonded linear dimers of TMA. No ordered structure was found in the potential region between P2 | P2´and P3 | P3´ (region IIIa). For E > P3, where the electrode surface bears a positive excess charge [60], a long-range ordered and rather fragile new phase, labeled IIIb, starts to emerge (Fig. 4-11). Individual domains of 50 to 100 nm size exhibit a characteristic arrangement of alternating bright and dark stripes. Often one observes neighboring domains mutually rotated by integer multiples of 30° indicating a commensurate registry of the adlayer with the hexagonal substrate surface.

High-resolution images such as shown in Fig. 4-11 B reveal details of the striped phase. Rows of identically aligned bright dots (trace (i)) are separated by alternating rows of parallel aligned light gray (trace (iii)) respective dark gray (trace (ii)) ellipsoidal-like features of 0.7 to 0.9 nm length. Their axis is tilted by 60° to 70° with respect to the main row directions. Cross-section profiles (Fig. 4-11 C) along the row of bright dots (trace (i) in Fig. 4-11 B, C) reveal asymmetric main maxima and smaller side maxima with characteristic repeat distances of (0.86 ± 0.05) nm, i.e. neighboring features are approximately three lattice constants apart. The apparent corrugation height is estimated as 0.20 to 0.40 nm. Adjacent rows of bright dots

appear to be slightly darker while every other row is identical and exactly aligned. The interspacing rows of light and dark features exhibit rather broad maxima of similar periodicity with an apparent corrugation height of 0.05 to 0.15 nm (Fig. 4-11 C, traces (ii) and (iii)). A rectangular repeat motif with a = (0.86 ± 0.05) nm (≈ $3 \mid a_{Au} \mid$) parallel and b = (2.15 ± 0.20) nm (≈ $4\sqrt{3} \mid a_{Au} \mid$) perpendicular to the bright rows could be identified (Fig. 11 B, Tab. 4-1). The different STM contrast patterns and the increase of the apparent corrugation height in region IIIb indicate an orientation change from flat-lying to a tilted and/or upright-standing configuration accompanied by major changes in the substrate–adsorbate interaction potential.

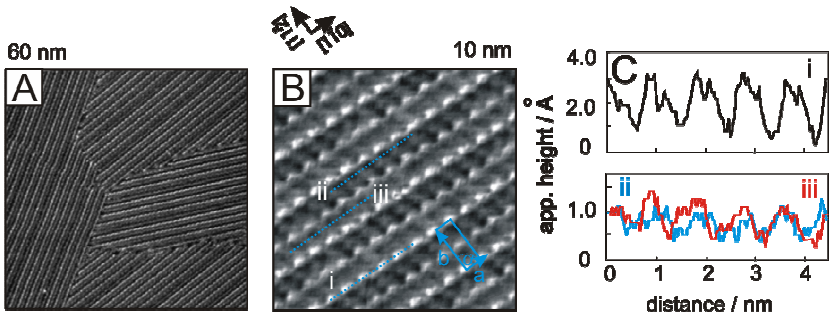

Fig. 4-11: (A) Large-scale in situ STM image of the chemisorbed striped TMA adlayer IIIb on Au(111)-(1 x 1) | 0.05 M H_2SO_4 in the presence of 3 mM TMA, E_S = 0.70, i_T = 60 pA. (B) High-resolution image of IIIb on Au(111)-(1 x 1), E_S = 0.70 V, i_T = 77 pA. The primitive unit cell is indicated. (C) Typical cross-section profile along the directions indicated in (B).

The surface orientation was explored in a comprehensive steady state and time resolved study employing surface enhanced infrared reflection absorption spectroscopy (ATR-SEIRAS). The detailed study has been presented in ref [60], and here we only focus on selected main results (Fig. 4-12). No TMA-related spectral features were found at E < 0.40 V supporting the notion of flat-orientated molecules. In the potential regions IIIa and IIIb, i.e. for E > 0.40 V, three distinct positive-going IR bands appear in the presence of 3 mM TMA at 1720 to 1735 cm^{-1}, around 1375 cm^{-1}, and at 1300 to 1320 cm^{-1} [60]. Comparison with solid state and solution spectra [95,96] supports the assignment of these spectral features to the following TMA vibrations: the stretching mode of C=O in COOH ($\upsilon_{(C=O)}$), the symmetric stretching mode of O-C-O in COO^- ($\upsilon_{s(OCO)}$), i.e. a deprotonated carboxylate group, and the stretching mode of C-OH in COOH ($\upsilon_{(C-OH)}$), respectively. The intensities of the TMA

bands increase with positive potential, reach their maximum in the chemisorbed region III, and decrease to zero during the subsequent negative-going scan [60]. Referring to the surface selection rule of SEIRAS that only vibrations with dipole changes perpendicular to the local surface can be observed [97], we conclude that perpendicularly oriented TMA molecules could be chemisorbed onto the positively charged electrode surface via one or two deprotonated carboxylate groups. TMA forms a distinct chemisorption bond. The corresponding gain in chemisorption energy with the upright geometry is assumed to compensate for the loss of the π-bonding upon reorientation of the flat-lying species. Carboxylate formation is a typical finding on a positively charged electrode surface in contact with aqueous electrolyte [98,99,100].

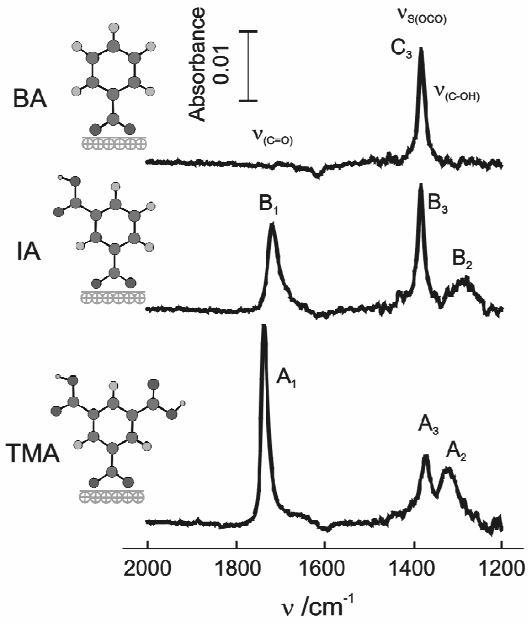

Fig. 4-12: Equilibrium SEIRA spectra of TMA (3 mM), IA (saturated solution) and BA (3 mM) in 0.05 M H_2SO_4 obtained at 0.800 V in region IIIb. The reference spectra were taken at E = -0.200 V. The insets illustrate the derived interfacial orientations of the three molecules chemisorbed on a positively charged Au(111-25 nm) film electrode.

To resolve the issue on surface coordination, we carried out a comparative study of TMA with benzoic acid (BA) and isophthalic acid (IA) in the high coverage region [60]. These carboxylic acids have different numbers of identical carboxyl groups, but similar conjugated structures. Fig. 4-12 shows typical SEIRAS equilibrium spectra of

the three molecules at E = 0.80 V. The comparative correlation and intensity analysis of the observed carboxylate modes and of the vibrations attributed to protonated carboxyl groups provide clear evidence for deprotonation and surface coordination of only one carboxylate group of TMA. The remaining two protonated carboxyl side groups are directed toward the electrolyte and may form intermolecular hydrogen bonds [60]. Based on calculations and experimental evidence for related systems [66,98-105], we suggest that the surface bound carboxylate group is centered at twofold short bridge sites. The carbon atom resides midway between two nearest neighbor gold atoms, and the chemically bound oxygen atoms are equivalent from the surface. The phenyl ring and the protonated carboxyl groups may undergo conformational rotations with respect to C–C bonds which allow forming a supramolecular network stabilized by intermolecular hydrogen bonds involving the solution-directed carboxyl groups.

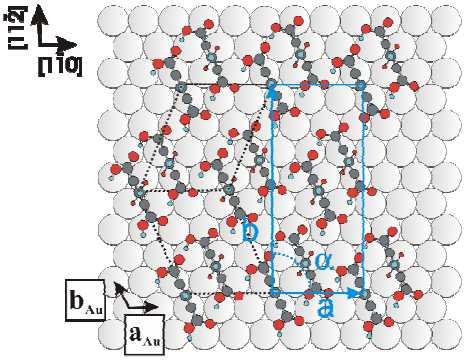

Fig. 4-13: Proposed packing model of TMA in region IIIb. The parameters of the unit cell are summarized in Table 4-1.

Based on complementary observations from in situ STM and ATR-SEIRAS experiments we propose the model depicted in Fig. 4-13 for the adlayer of chemisorbed TMA in the potential region IIIb. The structure is represented by a commensurate (3 x 4√3) unit cell. Using vectors of the primitive gold lattice, a_{Au} and b_{Au} as basis, one obtains in matrix notation $\begin{pmatrix} a \\ b \end{pmatrix} = \begin{pmatrix} 3 & 0 \\ 4 & 8 \end{pmatrix} \begin{pmatrix} a_{Au} \\ b_{Au} \end{pmatrix}$. The unit cell is composed of four molecules. The corresponding area per molecule and coverage were obtained as $A_{IIIb}(th) = 0.43\ nm^2$ and $\Gamma_{IIIb}(th) = 3.8\ 10^{-10}\ mol\ cm^{-2}$, respectively. The bright dots along [1$\bar{1}$0] are assigned to pairs of upright and parallel aligned TMA molecules coordinated to the positively charged substrate surface via one

deprotonated carboxylate group per molecule. The aromatic ring and the carboxylate group of one molecule assume a coplanar conformation. A 30^o rotation of the carboxylate plane is suggested for the second TMA molecule of the pair. The surface-bound carboxylate groups of both molecular units are in registry with the direction of the hexagonal substrate in energetically favored bridge sites.

The parallel orientation of the phenyl ring and their alignment with the rows of densely packed gold atoms within one pair is supported by the possible formation of intermolecular hydrogen bonds involving the solution directed protonated carboxyl groups. In this arrangement the parallel phenyl rings of one dimer are separated by 0.375 nm (= ¾ √3 $|a_{Au}|$), and the distance between the displaced centers of carboxylate groups amounts to 0.38 nm (= ½ √7 $|a_{Au}|$). Nearest neighbor parallel rows of bright dots, which appear slightly darker in the experimental STM image, are also assigned to pairs of upright TMA molecules, exhibiting just the reverse alignment of phenyl ring and coordinating carboxylate. The two types of alternating molecular rows are separated by 1 nm (= 2√3 $|a_{Au}|$) in $[11\bar{2}]$ direction. The bright features in neighboring rows representing pairs of molecules are mutually shifted by 0.43 nm (= 3/2 $|a_{Au}|$) along the $[1\bar{1}0]$ direction. This arrangement still enables the existence of inter-row hydrogen bonding. Each TMA molecule may form up to four hydrogen bonds with neighboring moleculs, thus giving rise to a supramolecular ladder-type network. Based on X-ray crystal structure data [77] and molecular modeling with ChemDraw Pro hydrogen bond lengths ranging between 0.26 to 0.30 nm are estimated. The interspacing rows of light gray and dark gray ellipsoidal features between the rows of bright dots, as illustrated in the STM contrast pattern in Fig. 4-11B, might results from aligned carboxyl groups and/or mutually shifted phenyl rings of pairs of dimers.

4.4 Potential-induced Phase Transition:Dynamic Processes

The steady state experiments demonstrated that, depending on the applied electrode potential, up to five differently ordered TMA adlayers could be assembled on Au(111)-(1 x 1)/0.05 M H_2SO_4. The coverage increases upon polarizing the electrode surface from negative to positive charge densities accompanied by an

orientation change from planar (Ia, Ib, Ic, II) to upright (IIIb). We also notice that the three structures Ia (honeycomb), Ib (ribbon-type) and Ic (herringbone-type), once formed upon the potential-controlled assembly at the Au(111)│electrolyte interface, do not transform mutually into each other by tuning the electrode potential within an observation time of up to four hours. However, structural transitions could be triggered if the final potential was chosen in the potential regions II or III.

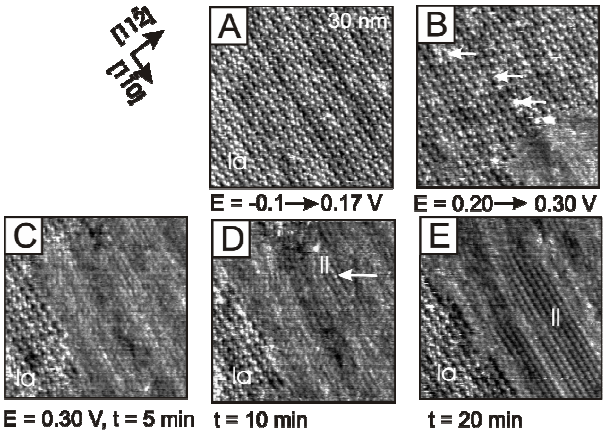

Fig. 4-14: Sequence of STM images (30 nm x 30 nm) for Au(111)│0.05 M H_2SO_4 in the presence of 3 mM TMA after a sequence of potential steps from E_S = -0.100 V (stability range of the hexagonal honeycomb phase Ia) to E_S = 0.300 V (stability range of the hydrogen-bonded dimer phase II), i_T = 120 pA. The formation of active "hole" nucleation sites is indicated by white arrows.

Fig. 4-14 illustrates the dissolution of the long-range ordered honeycomb phase Ia and the subsequent evolution of the linear dimer motif II after a series of potential steps from E_i = -0.100 V to E_f = 0.300 V. The process starts with the appearance of "frizzy spots" indicating a local enhancement in the mobility of the hydrogen-bonded network Ia (cf. arrows in Fig. 4-14 B). The active sites are evenly distributed across entire terraces without specific preferences to defects of the adlayer or substrate lattice. Subsequently, they transform into islands of a disordered pattern, such as indicated in the lower right corner of Fig. 4-14 B. Growth proceeds preferentially along the symmetry directions of the molecular adlayer Ia, which are in registry with the substrate surface. The transient phase appears fluid-like with a distinct local order (Fig. 4-14 C, D). However, no patterns resembling the motifs Ib or Ic could be identified. After an induction period parallel lines of linear dimers, the adlayer motif II, start to

grow along the [1$\bar{1}$0] symmetry direction of the substrate surface (first islands in Fig. 4-14 D and larger areas in Fig. 4-14 E). Adjacent patches of Ia and II are separated by disordered regions. No complete transformation could be achieved, most probably related to kinetic limitations due to uncorrelated domains of the two ordered phases and/or to the slow movement of domain walls [106].

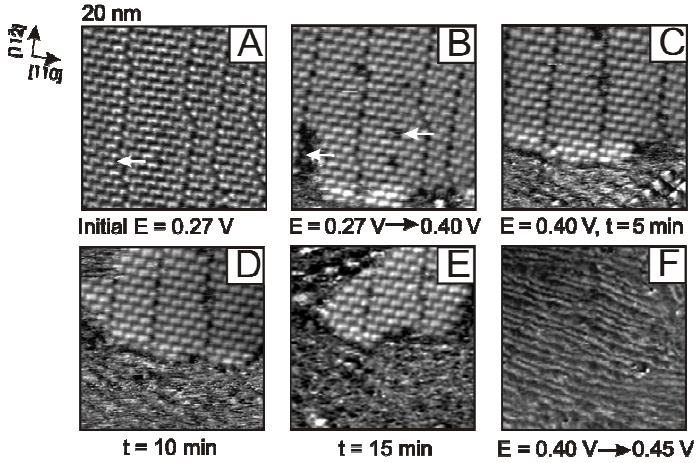

Fig. 4-15: Sequence of STM images for the transition from phase II to phase IIIa after a potential step from E_S = 0.270 V (stability range of the linear dimer phase II) to E_S = 0.450 V (stability range of the disordered chemisorbed stripe phase IIIa), i_T = 82 pA. White arrows indicate the formation of active sites of the structural transformation.

Once the hydrogen-bonded dimer motif II is formed by potential controlled self-assembly from electrolyte solution on Au(111)-(1 x 1) (stability range delimited by the pairs of current peaks P1 | P1´ and P2 | P2´), it can be transformed at E < P1´ into the honeycomb phase Ia, and at E > P2 into the disordered chemisorbed adlayer IIIa (Fig. 4-15). The later process starts at adlayer defects on terraces, but most frequently on translational domain boundaries. These local sites are composed of planar-oriented TMA monomers (Fig. 4-15 A, Fig. 4-15 B). The latter are less strongly stabilized by the two-dimensional hydrogen-bonded network in region II. Subsequently, the linear dimers dissolve anisotropically line-by-line. The dissolution rate parallel to the chains of linear dimers, which are aligned to the [1$\bar{1}$0] substrate direction, is faster than the process perpendicular to these rows. The newly formed adlayer IIIa is composed of rather fragile and irregular one-dimensional features, which start to align at higher positive fields into a disordered chemisorbed striped phase. Complementary IR-

spectroscopic investigations revealed that this transition involves an orientation change of TMA molecules from planar to perpendicular, accompanied by the deprotonation of *one* COOH-group that is chemically bound to the positively charged electrode. The formation of a highly ordered two-dimensional network of chemisorbed TMA molecules IIIb, as found for the direct assembly from electrolyte solution (Fig. 4-11), appears to be hindered kinetically. Possible reasons are the high surface coverage of TMA molecules as well as the low mobility of TMA molecules on the surface due to the strong chemisorption.

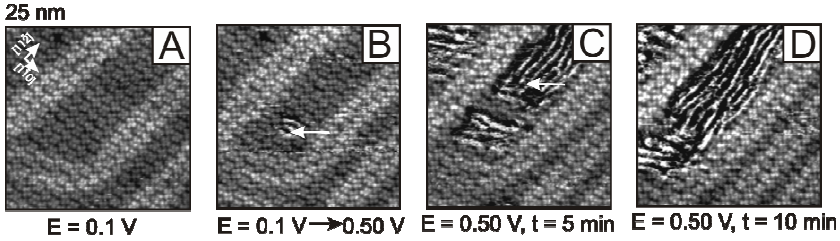

Fig. 4-16: Sequence of STM images for Au(111)-(p x √3)│0.1 M H_2SO_4 in the presence of 3 mM TMA after a potential step from E_S = 0.100 V (stability range of the ribbon-type motif Ib) to E_S = 0.500 V (A, B, C, D), i_T = 82 pA. White arrows indicate the formation of active sites (B, C) of the structural transformation.

Finally, we report on the role of the Au(111)-(p x √3) surface reconstruction. All hydrogen-bonded adlayers of planar oriented TMA molecules (Ia, Ib, Ic and II) were also found on the thermally and electrochemically reconstructed Au(111)-(p x √3) electrodes. We estimated dimensions of the respective unit cells being identical to the results obtained with Au(111)-(1 x 1) within experimental error. However, we also discovered that the physisorbed adlayers of planar oriented hydrogen-bonded TMA molecules are stabilized within the reconstruction domains, where the top-layer gold atoms occupy hcp and fcc lattice sites. An example is given in Fig. 4-16. The ribbon-type adlayer Ib was assembled via direct deposition from aqueous solution at E = 0.100 V on an electrochemically reconstructed surface. Alternating rows of squares and rhombohedral motifs are aligned with the $[11\bar{2}]$ substrate direction. Stepping the potential to E_f = 0.500 V, i.e. to positive charge densities in region IIIa, causes the formation of hole nuclei only on unreconstructed patches of the Au(111) surface (Fig. 4-16 B). These activated sites initialize the growth of the disordered chemisorbed striped phase IIIa. Individual stripes of the newly formed adlayer are typically aligned

with one of the neighboring reconstruction lines parallel to the [11 $\bar{2}$] substrate direction. No disintegration of the hydrogen-bonded physisorbed adlayer was found on the reconstructed patches.

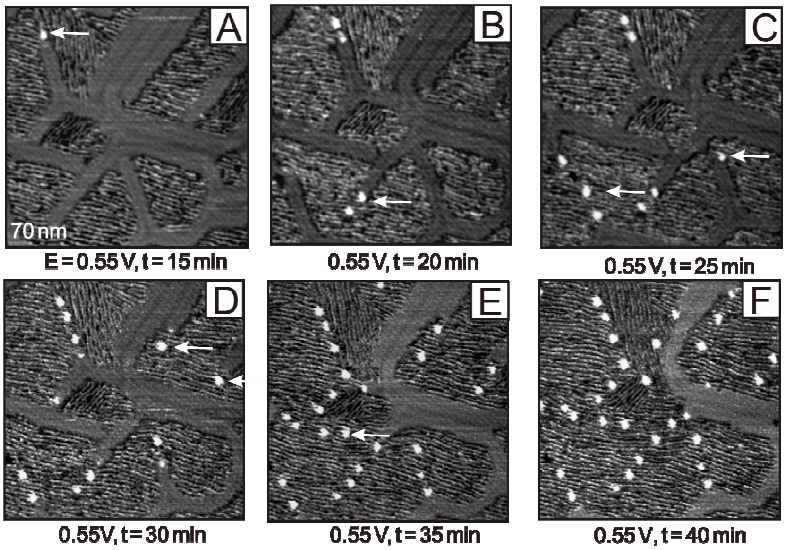

Fig. 4-17: Sequence of STM images for Au(111)-(p x √3) | 0.1 M H_2SO_4 in the presence of 3 mM TMA after a potential step from E_S = 0.100 V (stability range of the ribbon-type motif Ib) to E_S = 0.550 V (stability range of the disordered chemisorbed stripe phase IIIa), i_T = 170 pA. White arrows indicate the formation of monatomic gold islands due to the lifting of the substrate surface reconstruction.

Upon further increasing the electrode potential to positive values one triggers the lifting of the surface reconstruction as indicated by the appearance of gold islands in Fig. 4-17. The local reconstruction is lifted with progressing observation time resulting in the formation of many monatomically high gold islands. Their size is rather constant (about 5 nm), and they seem to decorate exactly the directions of the previously existing reconstruction elements. This observation demonstrates that the gold islands just contain atoms, which are released from adjacent lattice positions of the previously reconstructed substrate, and immediately after this step their further mobility is “frozen”. The formation of gold islands induces a distinct disorder within phase IIIa, which prevents the growth of the long-range ordered chemisorbed striped phase IIIb, even at significantly higher electrode potentials. Similar observations were

also obtained when starting the experiment with the honeycomb Ia or the herringbone Ic phases on Au(111)-(p x √3).

4.5 Isophthalic, Terephthalic and Benzoic Acids

We have discussed the potential-controlled self-assembly of TMA on Au(111) in 0.05 M H_2SO_4. In order to further understand the structure-determining role of hydrogen bonds formed from the carboxylic groups, we extended our studies to a series of carboxylic acid molecules containing either two carboxylic groups such as isophthalic acid (IA, 1,3-benzenedicarboxlic acids) and terephthalic acid (TA, 1,4-benzenedicarboxlic acid), or a single one (benzoic acid, BA) as shown in scheme 4-2.

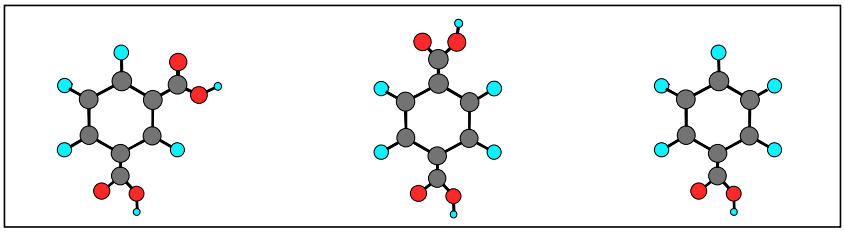

Isophthalic acid (IA) **Terephthalic acid (TA)** **Benzoic acid (BA)**

Scheme 4-2: Molecular structures of the target molecules IA, TA and BA.

The strategies applied here are similar to those already reported for TMA. Therefore, we will only focus on the main results and comparisons among these molecules. We will start this section with an overview of the electrochemical and large-scale STM data. Then, 2D ordered physisorbed structures together with the corresponding structure models of the IA, TA and BA will be presented in a comparative way. Finally, chemisorbed adlayers of the above molecules will be described.

4.5.1 Electrochemistry and STM overview

Cyclic voltammograms of IA, TA and BA on Au(111)-(1x1) in 0.1 M $HClO_4$ are shown in Fig. 4-18.

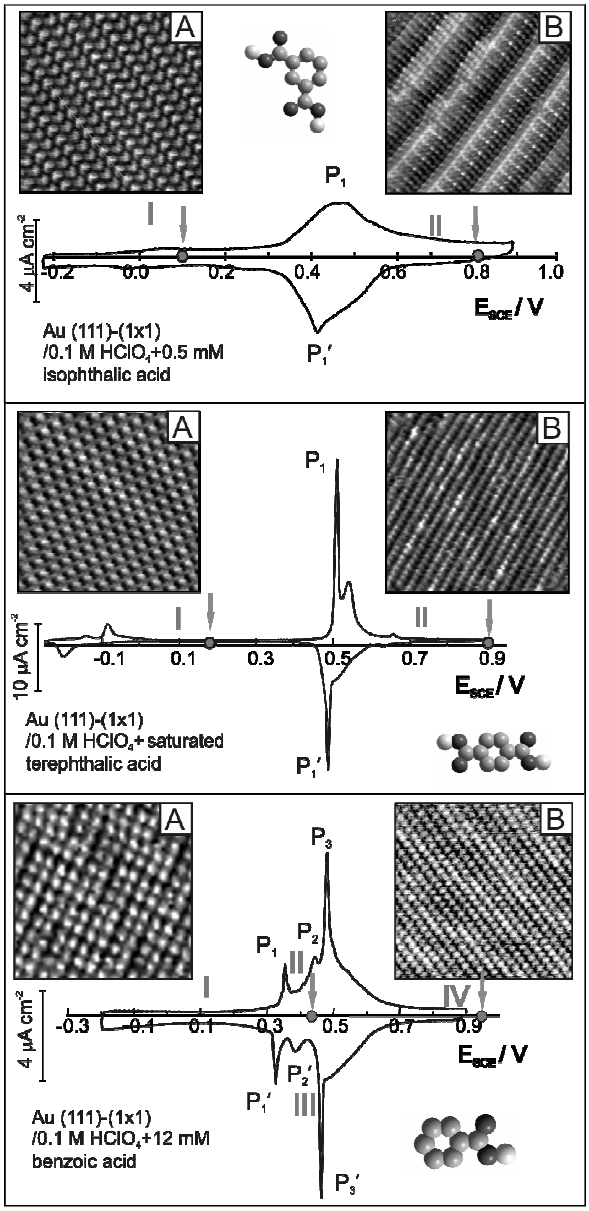

Fig. 4-18: Cyclic voltammograms and in situ STM images of IA (upper block), TA (middle block) and BA (lower block). The images "A" represent physisorbed adlayers and "B" represent chemisorbed structures. The corresponding potentials for the individual adlayers are indicated by the arrows. The size of the images is 10 nm x 10 nm.

The current vs. potential curve of IA on Au(111)-(1x1) in 0.1 M $HClO_4$ shows only one pair of current peaks around the potential of E_S = 0.450 V, corresponding to

the structural transition between the planar-oriented physisorbed adlayer, which exhibits a zig-zag motif in the STM image of Fig. 4-18, upper panel (A), and an upright-oriented chemisorbed structure [Fig. 4-18, middle pannel (B)]. The stability range of the planar-oriented zig-zag adlayer is -60 mV $\leq$ E $\leq$ 390 mV. No ordered molecular adlayer was detected at potentials more negative than -60 mV.

The voltammogram of TA shows two pairs of current peaks with the main peaks labeled as P1/P1'. The pair of peaks P1/P1' represents a phase transition between planar and upright oriented molecules. One also observes a pair of small current peaks at rather negative potentials, which we assign to the formation and dissolution of 2D ordered planar-oriented molecules. No ordered molecular adlayer was found at potentials negative from these small current peaks.

The current vs. potential curve of Au(111)-(1 x 1) in 0.1 M $HClO_4$ in the presence of 3 mM BA shows only one pair of current peaks at E = 0.480 V. We observed small domains of chemisorbed BA molecules at a positively charged electrode. Increasing the solution concentration of BA from 3 mM to 12 mM, 3 pairs of well-developed current peaks were found, which separate 4 potential regions labeled I, II, III and IV (Fig. 4-18, lower panel). Three highly ordered molecular structures were observed in the potential regions II, III, IV, and no ordered adlayer was found at potentials more negative than P1/P1', i.e. in region I.

Two distinctly different types of adlayers are created at negative and positive charge densities for IA and TA. The phase behavior of BA is more complex. However, for comparison with IA and TA we show in Fig. 4-18 only one of the physisorbed structures (phase III) and the chemisorbed adlayer (phase IV). Details of the 2D ordered adlayer structures of these three molecules on Au(111) will be discussed in the following section.

4.5.2 2D physisorbed adlayers

The self-assembly of physisorbed adlayers of aromatic carboxylic acids (IA, TA, and BA) on Au(111)-(1x1) demonstrates the selective role of directional hydrogen bonds in the formation of self-assembled adlayer structures on surfaces.

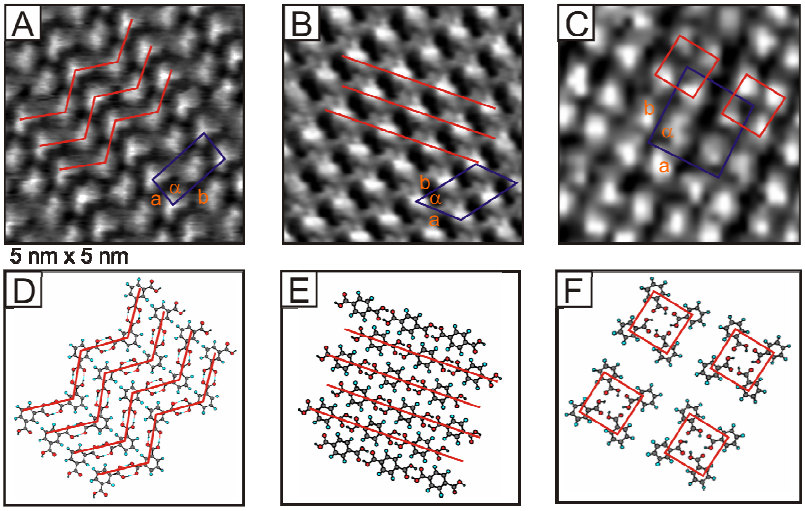

Fig. 4-19: High-resolution in situ STM images of planar-oriented physisorbed molecular structures of the IA (A), TA (B) and BA (C) on Au(111)-(1x1); i_T = 20 – 200 pA and E_S refers to Fig. 4-18. The corresponding molecular models are shown in panels D, E and F . The characteristic structure motifs of the hydrogen-bonded adlayers [zigzag (IA), linear tapes (TA), and molecular squares (BA)] are illustrated as red curves. The unit cells are indicated as blue parallelograms.

At potentials more negative than the pair of current peaks P1/P1' in the Fig. 4-18 (upper panel), IA is planar oriented on Au(111)-(1x1) (supported by the cross section analysis and the ATR-SEIRAS experiments discussed in the 4.3.3, cf. Fig. 4-12). High-resolution STM images, such as Fig. 4-19 A, show a characteristic zigzag pattern (red lines in Figs. 4-19 A and D). Individual bright features were assigned to IA molecules, which are hydrogen-bonded to two adjacent molecules. The corresponding angle is estimated to 120 degrees. The experimentally determined unit cell with a = (0.74 ± 0.05) nm, b = (1.68 ± 0.08) nm and α = (90 ± 5)° is composed of two IA molecules (Fig. 4-19 A), giving rise to a coverage of $\Gamma = (2.7 \pm 0.3) \times 10^{-10}$ mol cm^{-2}. Our tentative model containing one molecule is proposed on the basis of the analysis of the characteristic dimensions, and the comparison with crystallographic data. For clarity, the substrate atoms are not shown in the figure but were taken into account for the analysis. The corresponding parameters are summarized in Table 4-2.

Depositing the TA molecules at negative potentials, e.g. E = 0.18 V as indicated in Fig. 4-18, middle panel, gives rise to a linear tape structure. The molecules are planar oriented. Each molecule in the linear tapes aligns with two neighboring

molecules through hydrogen bonds formed between the carboxylic groups. The corresponding unit cell contains two molecules. The estimated dimensions are a = (1.00 ± 0.08) nm, b = (1.50 ± 0.10) and α = (53 ± 8)° nm. The area per molecule is obtained as 0.6 nm^2, which corresponds to a surface coverage of Γ = (2.8 ± 0.3) × 10^{-10} mol cm^{-2}. The characteristic data and the corresponding model parameters are summarized in Table 4-2.

Table 4-2: Characteristics of the unit cell parameters of physisorbed IA, TA and BA adlayers.

molecules	a [nm]	b [nm]	α [°]	area A per molecule [nm^2]	coverage Γ 10^{-10} mol cm^{-2}
IA	0.74 ± 0.05 *0.75*	1.68 ± 0.08 *1.73*	90 ± 5 *90*	0.62 ± 0.05 *0.65*	2.7 ± 0.3 *2.6*
TA	1.00 ± 0.08 *1.0*	1.50 ± 0.10 *1.5*	53 ± 8 *60*	0.60 ± 0.05 *0.65*	2.8 ± 0.3 *2.6*
BA	1.58 ± 0.10 *1.52*	1.62 ± 0.10 *1.52*	85 ± 8 *79*	0.63 ± 0.06 *0.57*	2.6 ± 0.3 *2.9*

The experimentally determined values are plotted in the first line of each row. The second line (italics) represents the parameters of the proposed model suggested upon considering the registry between substrate surface and adlayer.

In case of the BA, no physisorbed ordered adlayer was detected in our studies for solute concentrations lower than 3 mM. Increasing the concentration to 12 mM gives rise to two types of physisorbed, planar-oriented adlayers, which were identified as striped and zig-zag tetramer structures. Here, we only show the latter for comparison with the other two carboxylic acids. In situ STM images, such as shown in Fig. 4-19 C, show quadratic features (red curve). The bright spots at each corner of the quadratic motifs represent individual BA molecules, and four molecules at the corners seem to interact with each other via intermolecular hydrogen bonds [107,108] to increase the stability and to decrease the adsorption energy. The unit cell indicated by the blue quadrate in Fig. 4-19 C shows the following characteristic dimensions: a = (1.58 ± 0.10) nm, b = (1.62 ± 0.10) and α = (85 ± 8)°. The unit cell contains 4 molecules, which gives rise to a coverage of Γ = (2.6 ± 0.3) × 10^{-10} mol cm^{-2}. The characteristic data and the corresponding model parameters are summarized in Table 4-2.

4.5.3 2D chemisorbed adlayers

Increasing the substrate potential to higher positive values, e.g. E > P1/P1' for IA and TA, and E > P3/P3' for BA, gives rise to distinctly different structural patterns. The cross-section measurements show that the apparent heights are 0.3 - 0.4 nm, which is 2-3 times as large as the physisorbed, planar-oriented adlayers discussed above. Clearly, a non-planar molecular orientation is formed. This hypothesis is supported by ATR-SEIRAS experiments [60]. A systematic ATR-SEIRAS study of the four carboxylic acids (TMA, IA, TA, BA) indicates that in this potential range all molecules adsorb in a vertical or tilted manner on the Au(111) surface with a single deprotonated carboxylate group facing the electrode [60]. The formation of equilibrated 2D ordered, chemisorbed adlayers was rather difficult. To create long-range ordered structures with large domains, we applied two strategies for assembling the molecules: (1) adding molecule-containing solution at rather positive potentials, e.g. 0.80 V, under strict potential control, followed by continuous sweeping of the substrate potential for two hours in the positive region. (2) To overcome the energy barrier for rearrangement of molecules, we added warm solutions (50 ºC) instead of using an assembly solution at room temperature. Both strategies allowed creating highly ordered molecular adlayers with a domain size as large as 30 - 40 nm.

Fig. 4-20 shows high-resolution STM images of chemisorbed structures of IA (Fig. 4-20 A), TA (Fig. 4-20 B) and BA (Fig. 4-20 C) at positive potentials. The adlayer of IA is rather fragile and easily destroyed by tip scanning compared with TA and BA. The high-resolution STM image in Fig. 4-20 A exhibits striped rows consisting of parallel bright spots. The bright features are tilted by 75° referring to the main row direction. Characteristic repeat distances of a = 1.55 nm separating every second row, and b = 0.80 nm as the distance between every other molecule within one row, were observed. Cross-section measurements show that the corrugation of the adlayer is about 0.3 nm – 0.4 nm. On the basis of these STM observations and of the results of a previous ATR-SEIRAS experiment [60], we conclude that IA molecules at E > 0.500 V are perpendicularly adsorbed on the gold surface with one deprotonated carboxylate group in contact with the electrode, and the other protonated carboxyl group facing the electrolyte. The repeat motif from the high-resolution STM image (Fig. 4-20 A) shows a $3\sqrt{3} \times \sqrt{7}$ structure. The tentative unit cell, composed of four IA

molecules, is represented by a parallelogram with a = 1.50 nm, b = 0.76 nm, and α = 71°. We also suggest that the surface-bound carboxylate group is centered at the two-fold bridge sites of the gold substrate, similar as proposed for the chemisorbed TMA adlayer. The corresponding unit cell parameters from experiments and models are summarized in Table 4-3.

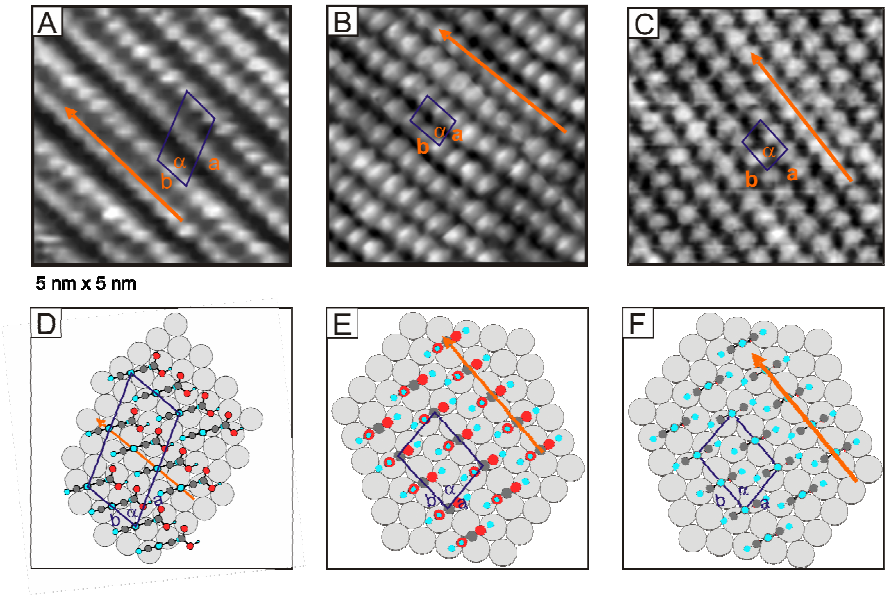

Fig. 4-20: High-resolution in situ STM images of the upright-oriented chemisorbed molecular structures of IA (A), TA (B) and BA (C); i_T = 5 – 50 pA. The values of E_S are identical to those reported in Fig. 4-18. The corresponding molecular models are shown in D, E, F respectively. The orange arrows indicate the molecular rows. The unit cells are indicated as blue parallelograms.

The chemisorbed adlayers of TA and BA are similar to that of IA. The molecules assume an upright or tilted orientation. The difference is that for benzoic acid, the molecules are chemisorbed on the surface with the only available deprotonated carboxylate group. In case of TA, one carboxyl group is deprotonated and directed toward the electrode surface, while the other one faces the electrolyte. The similarity between the adsorption of these molecules can be used to explain why the two molecules have the same unit cell (table 4-3). In case of IA molecules, the unprotonated carboxyl side group leads to a somewhat lower packing density together with a higher fragility of the adlayer formed. All characteristic parameters of the suggested unit cells are summarized in Table 4-3.

Table 4-3: Characteristics of the unit cell parameters of chemisorbed IA, TA and BA adlayers.

molecules	a [nm]	b [nm]	α [°]	area A per molecule [nm^2]	coverage Γ 10^{-10} mol cm^{-2}
IA	1.55 ± 0.08 *1.50*	0.80 ± 0.05 *0.76*	75 ± 5 *71*	0.29 ± 0.05 *0.27*	5.7 ± 0.4 *6.1*
TA	0.56 ± 0.05 *0.58*	0.74 ± 0.08 *0.76*	80 ± 5 *79*	0.21 ± 0.03 *0.22*	7.9 ± 0.5 *7.6*
BA	0.58 ± 0.05 *0.58*	0.82 ± 0.08 *0.76*	76 ± 5 *79*	0.21 ± 0.03 *0.22*	7.9 ± 0.5 *7.6*

The experimentally determined values are plotted in the first line of each row. The second line (italics) represents the parameters of the proposed model adlayers.

Based on the discussion above, one can conclude that intermolecular hydrogen bonds play a key role in forming a wide range adlayer motifs of aromatic carboxylic acids on Au(111). The molecules assemble into the specific structures following the direction of the intermolecular bonds, e.g. IA forms zigzag molecular rows since the two carboxylic groups are in the 1 and 3 position of the phenyl ring having an angle of 120 degree. On the contrary, TA forms one-dimensional linear tapes determined by directional hydrogen bonds between two neighboring carboxylic groups located in 1,4-positions. In case of BA, each molecule has only one carboxylic group, which assembles in characteristic tetramers.

The molecular structures also affect the formation of chemisorbed adlayers. TA and BA exhibit the same stacking motif and have the same unit cell parameters since both molecules are vertically absorbed with one carboxylate group directed toward the surface. This packing motif is disturbed by the protonated carboxyl side group in IA, which leads to a lower coverage and a less stable adlayer compared to BA and TA.

4.6 Summary and Conclusions

We have studied the potential-controlled self-assembly of TMA and related molecules (IA, TA and BA) on Au(111)-(1x1) in contact with aqueous 0.05 M H_2SO_4 and 0.1 M $HClO_4$ solution by in situ scanning tunneling microscopy in combination with ATR-SEIRAS and cyclic voltammetry.

TMA is known to form in the crystalline state diverse patterns of intermolecular hydrogen-bonded assembles. Adsorption on a surface imposes significant contributions from additional substrate–adsorbate interactions. The electrochemical environment allows to steer the molecular self-assembly and to establish equilibrium structures by the subtle variation of the externally applied electric field.

At negative charge densities, individual TMA molecules appear in the STM contrast pattern as bright equilateral triangles, which reflect a flat-lying geometry with the phenyl ring parallel to the substrate surface. Based on experimental evidence and theoretical predictions, we propose that the aromatic phenyl rings of TMA are preferentially bound to threefold hollow sites of the Au(111) lattice. Four long-range ordered, commensurate adlayers with distinct two-dimensional packing motifs were found, which we labeled honeycomb (Ia), ribbon-type (Ib), herringbone-type (Ic) and linear dimer (II) phases. The commensurability reflects the non-negligible interactions with the Au(111) surface. A basic element or "synthon" of all these structures represents centrosymmetric hydrogen-bonded dimers formed between two carboxyl groups of two aligned TMA molecules. The honeycomb pattern, which only exists at a negatively charged electrode surface, is exclusively composed of hydrogen-bonded dimers formed through adjacent carboxyl groups.

The potential-controlled deposition of TMA at less negative charge densities leads to planar oriented hydrogen-bonded assemblies composed of ribbon-type (Ib) and herringbone-type (Ic) motifs. The surface coverage increases up to 70 %. The proposed structure models suggest a complex, but regular arrangement of centrosymmetric hydrogen-bonded TMA dimers, together with macrocycles composed of two, three or four individual molecules. These two-dimensional networks appear to be a compromise between an optimum geometry of hydrogen bond and minimization of surface free energy.

The hydrogen-bonded tri- and tetra-mer macrocycles are not stable if the external electric field is small. Around the potential of zero charge, TMA molecules form one-dimensional chains composed of an alternating arrangement of centrosymmetric and macrocyclic, hydrogen-bonded dimers. Neighboring chains are correlated giving rise to highly ordered two-dimensional sheets. Molecular modeling suggests the existence of inter-chain hydrogen bonds.

Increasing the electrode potential further to positive charge densities destabilizes all hydrogen-bonded networks of flat-adsorbed TMA molecules, and an orientation change from planar to upright takes place. One observes initially a disordered chemisorbed adlayer, which transforms at higher potentials into the mesoscopically long-range ordered striped phase. The process was monitored by combining in situ STM and SEIRAS: TMA molecules change their orientation from planar to upright accompanied by the deprotonation of one carboxyl group. Subsequently, this carboxylate group coordinates to the positively charged electrode surface while the two other carboxyl groups are directed toward the electrolyte. This arrangement supports the formation of a long-range ordered supramolecular ladder-type network, which is structurally determined by substrate–adsorbate coordination and lateral hydrogen bonds.

Complementary to TMA, we have also studied BA, IA and TA for comparison. We found that all three molecules can form highly ordered physisorbed (planar-oriented) and chemisorbed (upright-oriented) adlayers with the various assembly strategies developed. At negative potentials, IA forms 2D ordered zigzag stripes, and TA assembles into linear tapes, both triggered by directional hydrogen bonds. BA forms quadratic tetramers. At positive potentials, TA and BA have common unit cell parameters, and IA has a lower surface coverage due to the position of the second carboxylic group, which prevents the formation of a more compact molecular adlayer.

Chapter 5. Viologen Adlayers and Molecular Tunnel Junctions

5.1 Introduction

As the miniaturization of electronic components approaches the nanometer scale, new concepts to tailor structure, functionality and fabrication strategies are essential to overcome the fundamental physical and economic limitations of conventional inorganic silicon technology [109]. Bottom-up (self-) assembly of well-defined nanoscale building blocks, such as molecules [110], quantum dots [111], and nanowires [112] having key properties controlled by size, morphology and chemical composition represent an attractive alternative. The idea of building an electronic device using individual molecules was first proposed by Aviram and Ratner [113]. The molecular approach bears several unique opportunities: (1) custom design of nanoscale molecular units, (2) high reproducibility due to self-organization and recognition properties of the molecular building blocks, (3) implementation of localized functions such as charge transfer, π–π stack conductivity or molecular rectification [114,115].

The development of several experimental techniques, including mechanically controlled break junctions [31-33,116-118], nanowires [112], mercury junctions [35,119], and various SPM-based methods [34,38,41,54,110,120-127] have enabled scientists to explore electric properties of tailored individual molecules and molecular assemblies attached to conducting substrates. In SPM and surface nano-electrochemistry, free or cluster-tagged molecules [41,124] are typically in direct contact with one metal electrode. Bridging of individual molecules between a gold STM tip and a gold substrate was recently achieved in solution [34,65,128,129]. The statistical analysis of repeatedly created junctions provided access to the measurement of single-molecular conductivities.

Motivated by the pioneering work of the Liverpool group on single-molecule conductivity [41,65,128] we carried out a comparative study on the redox activity of viologens immobilized on gold electrodes in an electrochemical environment. Our approach combines macroscopic voltammetry with in situ scanning tunneling microscopy (STM) and spectroscopy (STS) [52]. The main goal of the present work is focused on measurements of electron transfer with redox-active, thiol-functionalized viologens as they are addressed by the electrochemical potential to explore relations between structures and electronic properties in molecular assemblies approaching the single molecule level.

The tailored functional target molecules in our studies are N-alkyl-N´-(n-thioalkyl)-4,4´-bipyridinium bromides (HS-nVn-H) and N,N´-bis(n-thioalkyl)-4,4´-bipyridinium bromides (HS-nVn-SH). The chemical structure of these viologens is illustrated in Scheme 5-1. The molecules are composed of a redox-active 4,4´-bipyridinium group, two flexible alkyl-spacer units of variable length, and one or two -SH end groups. The terminal thiol groups can chemically bind to gold electrodes, which allows to measure electron transfer characteristics and molecular conductance properties of Au │viologen │Au junctions.

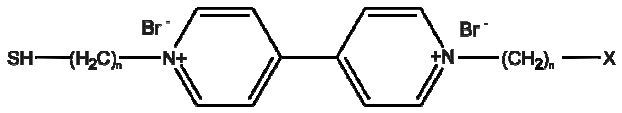

n = 5, 6, 7, 8, 10 (5V5, 6V6, 7V7, 8V8, 10V10); X = H: monothiol; X = SH: dithiols

Scheme 5-1: Chemical structure of the viologen molecule.

The redox-active viologens exit in three different oxidation states, the dication V^{2+}, the radical cation $V^{\bullet+}$ and the neutral form V^0. The transitions between these three forms involve two, rather reversible one electron transfer processes: $V^{2+} \leftrightarrow V^{\bullet+}$ and $V^{\bullet+} \leftrightarrow V^0$ [130,131]. Viologens have been incorporated as “backbone”-components in self-assembled monolayers [132-139], in nanometer-scale electronic switches [41,65] and in various functional materials [140]. The self-assembly and redox-functionality of thiol-functionalized viologens on gold macro-electrodes has been investigated by cyclic voltammetry [132,133,135-139], quartz crystal microbalance [132], IR [128], ex-situ STM [41,128], and STS [65,128] etc. In spite of

these abundant studies, there is no insight on the sub-molecular assembly and correlation between molecular structure and tunneling properties of viologens on gold surfaces available yet, which will be contributed in this study.

This chapter is organized as follows: First, we report electrochemical studies on Au (111) single crystal electrodes. Then, we present in situ STM investigations on the assembly of viologens of different chain length on gold electrodes. The final part of this chapter explores single-molecule electron transport and tunneling properties of redox-active viologens under electrochemical conditions based on molecular stretching and tunneling spectroscopy experiments.

5.2 Electrochemical Characterization of Viologens

5.2.1 Two-step redox process

Fig. 5-1 shows a typical first scan voltammogram of a Au(111)-(1x1) electrode modified with a monolayer of HS-6V6-SH in 0.05 M $KClO_4$ adjusted to pH = 10 by addition of KOH. The adlayer was prepared by immersion of the gold electrode in 1 mM ethanolic solution of HS-6V6-SH followed by thermal annealing at 70 ^oC for 12 hours. Contact with the electrolyte was established at E = -0.700 V. Subsequent potential excursion reveals three characteristic pairs of current peaks labeled P1/P1´, P2/P2´and P3/P3´. Restricting the potential range to E ≥ -1.050 V results in two pairs of well-defined current peaks (Fig. 5-1). P1 (E = -0.438 V) and P1´ (E = -0.419 V) are assigned to the one-electron reaction $V^{2+} \leftrightarrow V^{\bullet+}$ [130,131]. The peak-to-peak separation is rather constant up to 1 V s^{-1}, and the peak height scales linearly with the scan rate. These observations indicate a reversible electron transfer process [141]. The monolayer coverage is estimated to $(4.5 \pm 0.5) \times 10^{-10}$ mol cm^{-2}, which corresponds to an area of 0.37 nm^2 per molecule. The second pair of peaks P2 (E = -0.970 V) and P2´ (E = -0.840 V) is assigned to $V^{\bullet+} \leftrightarrow V^0$ [130,131], which is less reversible. The broadening of the peaks P2 and P2´ indicates quasi-reversibility and higher disorder within the adlayer.

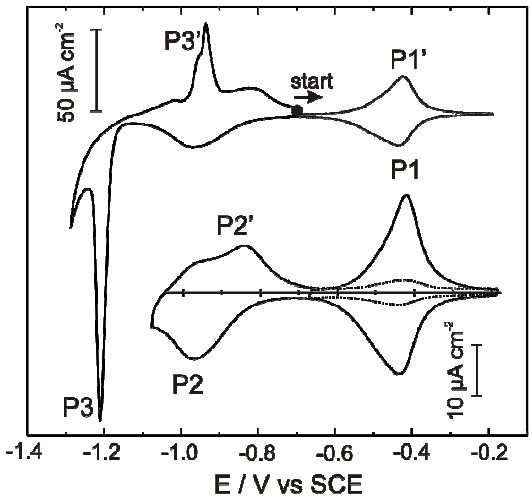

Fig. 5-1: First scan cyclic voltammograms of Au(111)-(1 x 1) electrodes modified with HS-6V6-SH in 0.05 M $KClO_4$, pH adjusted to 10 with KOH, sweep rate 50 mV s^{-1}. The inset shows first-scan voltammograms recorded in a limited potential range for high coverage (solid lines) and low coverage (dotted lines) viologen adlayers.

Au(111)-(1x1) electrodes modified with the monothiol HS-6V6-H gave results similar to those just described for HS-6V6-SH. The strict elimination of the oxygen exposure during the electrochemical measurement is extremely critical because trace amounts of oxygen could oxidize the adlayer (or due to some unknown reactions) and distort the redox response. We note that EC experiments of similar quality could be also recorded in our EC-STM setup if a lab-built "argon chamber" is used.

5.2.2 EC experiment in the STM setup

Fig. 5-2 (left) shows the lab-built argon chamber for carrying out experiments in an oxygen-free environment. The chamber is composed of a glass cylinder, a plastic front door and a metal lid. There are 4 outlets on the lid: two for input and output of argon, one for the STM cable connection and one for the teflon tube, through which the solution can be added. The following experimental procedure is applied: After the molecule-modified single crystal sample is mounted in the STM cell, the STM head together with cell and sample is transferred into the argon chamber. After careful sealing of the chamber, it is purged with argon. Finally, a certain amount of electrolyte solution (330 µl) is injected through the teflon tube using a clean Hamilton syringe and then the chamber was completely closed.

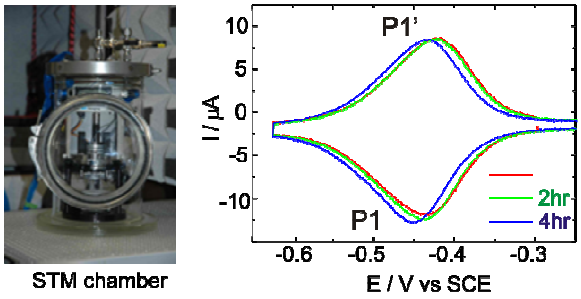

Fig. 5-2: (left) Lab-built STM chamber for controlling the environment. (right) Cyclic voltammograms of a Au(111)-(1 x 1) electrode modified with HS-6V6-H in a limited potential range around the first redox current peaks. Sweep rate: 100 mV s^{-1}.

Fig. 5-2 (right) shows a representative voltammogram of an Au(111)-(1x1) electrode modified with a monolayer of HS-6V6-H in 0.50 M $LiClO_4$, pH adjusted to 8.5 with KOH measured in the argon chamber. The first pair of characteristic redox peaks P1/P1´ ($V^{2+} \leftrightarrow V^{\bullet+}$) can be repeatedly obtained within the measuring time (several hours up to a whole day). There is no indication of oxygen distortion of the voltammograms. The potential drift is small, typically 20 mV over 4 hours. The following experiment work, e.g. in situ STM imaging and electron transfer investigation of the viologen adlayers, are carried out in the potential region of the first one electron transfer $V^{2+} \leftrightarrow V^{\bullet+}$ as shown in Fig. 5-2.

5.3 2D Assembly of Viologen Adlayers

In the previous sections, we described the electrochemical properties of viologens for both, a low-coverage and a high-coverage monolayer on Au(111)-(1x1). Subsequently, we carried out a series of in situ STM experiments in the potential range around the first redox peak to understand the 2D structural properties of these assemblies.

5.3.1 2D structures of viologens 6V6

Based on the sample-preparation protocol II (2 min contact with 50 µM ethanolic viologen-containing solution, 12 hours annealing in pure ethanol at 70 ^{o}C) and protocol III (cf. Section 3.1.2), distinctly different low-coverage and a high-coverage adlayers were obtained for both monothiol and dithiol viologens. Following the protocol II, HS-6V6-H and HS-6V6-SH (Fig. 5-3 A and D) form highly ordered

low-coverage adlayers on Au(111)-(1 x 1). One observes regular arrays of parallel stripes, which cover the entire substrate surface. The stripes are not uniform. Bright and dark contrast patterns alternate. Individual domains extend 10 to 50 nm. Neighboring domains with sharp boundaries are mutually rotated by multiples of 120° indicating registry of the adlayer with respect to the hexagonal substrate surface. This hypothesis is supported by the faceting of steps (Fig. 5-3 A). The steps are aligned with characteristic angles of 120° and step edges are decorated by parallel molecular rows. Occasionally one observes monatomically high gold and/or vacancy islands at domain boundaries.

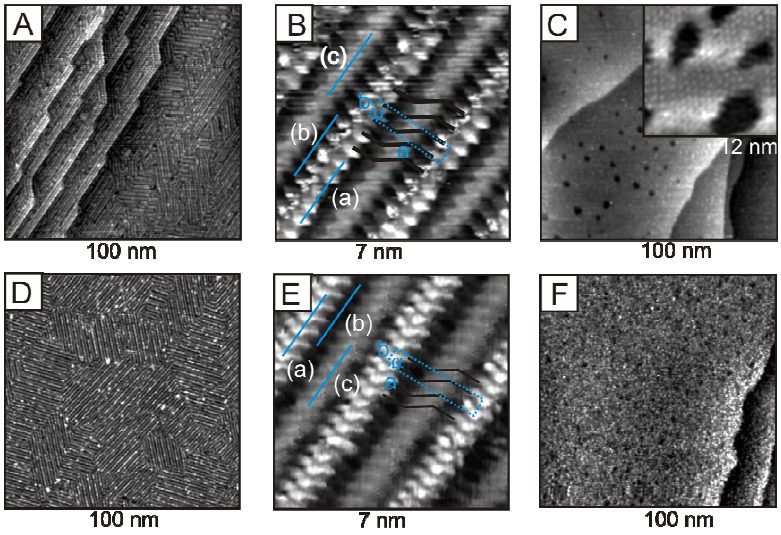

Fig. 5-3: In situ STM images of HS-6V6-H (Fig. A, B and C) and of HS-6V6-SH (Fig. D, E, F) on Au(111)-(1 x 1) in 0.05 M $KClO_4$, pH = 7, recorded at E_S = -0.200 V. Setpoint current: 50–100 pA. The images represent the low-coverage "striped" adlayers (A, B, D and E) and the high-coverage monolayers (C and F). The high-resolution images show distinct row patterns, which are indicated by the traces (a), (b) and (c). The typical zig-zag motif of the aligned segments is drawn as a sequence of black solid lines.

High-resolution experiments such as shown in Fig. 5-3 B and Fig. 5-3 E reveal more details of the molecular adlayers. The molecular rows composed of bright dots (trace a) are separated by parallel rows of dark grey (trace b) respectively light grey (trace c) ellipsoid-like segments. Their axes exhibit characteristic tilt angles with respect to the main row direction, which were estimated to (60 ± 5)° (light grey rows) and (90 ± 10)° (dark grey rows). The resulting, nearly equilateral zig-zag motif is

indicated in both high-resolution images. Parallel rows of the same type are separated by (2.6 ± 0.3) nm and (2.7 ± 0.3) nm for HS-6V6-H and HS-6V6-SH, respectively. Cross-section profiles reveal a periodicity of (0.50 ± 0.05) nm between individual features of each type of row, but distinct differences in the apparent corrugation height. Fig. 5-4 illustrates the apparent height profiles for HS-6V6-H. We estimate typical corrugations of (0.14 to 0.19) nm (trace a), (0.03 to 0.06) nm (trace b) and (0.05 to 0.12) nm (trace c). Similar data were obtained for HS-6V6-SH. The above results suggest a commensurate repeat motif with b = (0.50 ± 0.05) nm (= $\sqrt{3}\ a_{Au}$) parallel and a = (2.6 ± 0.3) nm (~ 9 a_{Au}) perpendicular to the molecular rows.

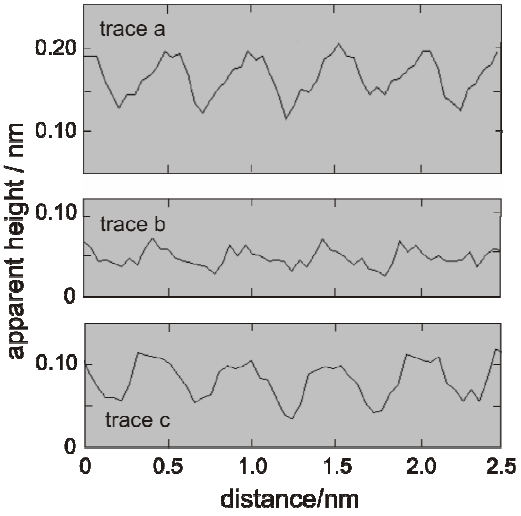

Fig. 5-4: Typical cross-section profiles along the traces drawn in Fig. 5-3 B for the striped adlayer of HS-6V6-H on Au(111)-(1 x 1) in 0.05 M $KClO_4$ at E_S = - 0.200 V.

In an attempt to derive structural models of the two adlayers we notice that the values of the apparent corrugation heights are similar to data reported for alkanthiols [142] aligned with their C-C-C backbone parallel, and for aromatic molecules [143] oriented with the π–system of the phenyl ring planar or slightly tilted to the Au(111) surface. This arrangement appears to be applicable for the two striped viologen adlayers prepared. This conclusion is also supported by our SEIRAS results, which showed no bands related to in-plane vibrations of the bipyridinium ring under conditions of the low coverage striped phase. Application of the surface selection rules of SEIRAS indicates that the aromatic rings of viologens appear to be oriented close to parallel to the gold surface [144].

In the literature, an enhancement of the tunneling current is observed in the vicinity of the sulfur group, often apparent as bright spots or slightly elongated features [145-147], while the alkyl chains are observed as regions of rather dark contrast [145,146]. Aromatic groups, such as phenyl, biphenyl or bipyridine units were also reported to enhance the tunneling contrast [143,148-150]. In applying this knowledge to the present case we notice that the width of the dark rows (trace b) increases with the length of the alkyl chains when replacing the hexyl groups in 6V6 by longer alkyl chains, such as octyl (C_8) or decyl (C_{10}), while all other features in the bright and light grey rows do not change [151]. The dimensions of the corresponding repeat motifs, which all indicate commensurability to the underlying Au(111) lattice, are compiled in Table 5-1. The values increase approximately 0.5 nm per $(CH_2)_2$-unit, which exactly scales with twice the distance between neighboring CH_2-groups [152]. In consequence, we assign the dark rows to the positions of the alkyl chains in a fully extended all-trans conformation with the molecular axis parallel to the surface plane. Based on adsorption studies of alkanes on Au(111) [152], we assume that the C-C-C axis aligns with the $[1\bar{1}0]$ direction of the hexagonal substrate.

The light grey lines in Fig. 5-3 B and Fig. 5-3 E exhibit an internal structure, which resembles the arrangement of planar or extended stacking rows of 4,4´-bipyridine units in self-assembled monolayers [149,150]. In analogy to these reports we attribute the light grey rows in the high-resolution STM images tentatively to the positions of the viologen moieties. The intermolecular distance between neighbouring units, 0.43 nm ($= \sqrt{3}a_{Au}\sin 60^o$), is too small to allow a plane-parallel arrangement to the substrate, but also too large for a perfect stacking structure. The latter is not expected to be stable due to electrostatic repulsion between the 4,4´-bipyridinium dications. Finally, we assigned the bright rows to the positions of the terminal sulfur functionalities.

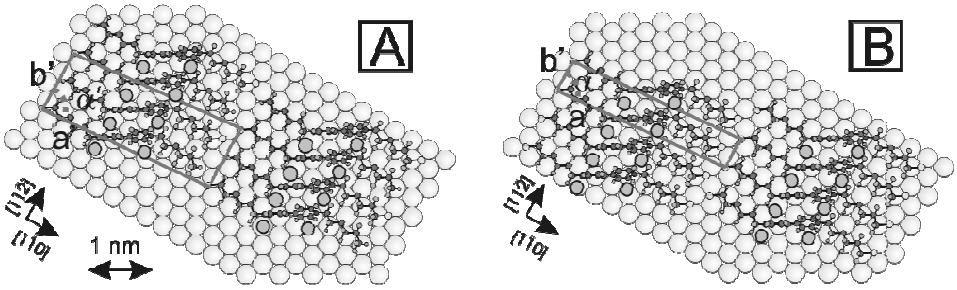

Fig. 5-5: Proposed packing models of the ordered striped phases of HS-6V6-H (A) and HS-6V6-SH (B) on Au(111)-(1 x 1). The co-adsorbed perchlorate ions (open circles) are tentatively located next to the ring nitrogen atoms. The sulfur atoms are represented as yellow circles.

The suggested structural models of HS-6V6-H and HS-6V6-SH on Au(111) are drawn in Fig. 5-5. Using the vectors of the primitive gold lattice, a_{Au} and b_{Au}, with $|a_{Au}| = |b_{Au}| = 0.2885$ nm as a basis, we propose the following unit cell in matrix notation $\begin{pmatrix} a \\ b \end{pmatrix} = \begin{pmatrix} 9 & 1 \\ -2 & 4 \end{pmatrix} \begin{pmatrix} a_{Au} \\ b_{Au} \end{pmatrix}$ and $\begin{pmatrix} a \\ b \end{pmatrix} = \begin{pmatrix} 9 & 1 \\ -1 & 2 \end{pmatrix} \begin{pmatrix} a_{Au} \\ b_{Au} \end{pmatrix}$ for HS-6V6-H and HS-6V6-SH respectively. The unit cell, containing two (HS-6V6-H) or one (HS-6V6-SH) molecules, are indicated by the thick blue lines in Fig. 5-5. The area per molecule and the coverage obtained from the unit cells are $A_L = 1.4$ nm^2, $\Gamma_L = 1.2 \times 10^{-10}$ mol cm^{-2} for the both low-coverage ordered viologen adlayers. The detailed characteristic data and the corresponding model parameters of HS-6V6-SH are summarized in Table 5-1.

The adsorption of the viologen molecules 6V6 onto Au(111)-(1x1) was also investigated following the preparation protocol III (1 mM ethanolic viologen solution 12 hour at 70 ºC, cf. 3.1.2). This leads to a high-coverage, poorly ordered structure of HS-6V6-H (Fig. 5-3 C inset). A ($\sqrt{7}$ x $\sqrt{7}$) R19.1º structure motif could be identified. The resulting coverage amounts to 3.3×10^{-10} mol cm^{-2}, which is in reasonable agreement with the voltammetry data. The adlayer is composed of many atomically deep vacancy islands with a typical size of 2-5 nm in diameter. No ordered adlayer was found for the high-coverage phase of upright HS-6V6-SH molecules on Au(111)-(1x1) (Fig. 5-3 F). The difference to the monothiols nicely illustrates the structure-determining role of the alkyl chain above the aromatic group as already pointed out by Ulman et al. [153].

5.3.2 Viologen 5V5

The electrochemical characteristics and surface structural properties of N,N´-bis(5-thiopentyl)-4,4´-bipyridinium bromide (HS-5V5-SH or 5V5) are rather similar with HS-6V6-SH (6V6) [151]. Here, as an example, we only briefly discuss the structural properties of 5V5 to reveal the differences and common motifs of viologens with distinct chain spacers. Fig. 5-6 A shows the low-coverage ordered 5V5 adlayer on Au(111) prepared according to protocol II. The stripes are not uniform, and bright and dark contrast patterns alternate. The high-resolution image (Fig. 5-6 B) reveals details of the molecular adlayer. Rows of bright dots are separated by parallel rows of dark grey and light grey ellipsoidal-like segments. The parallel rows of the same type are separated by (2.4 ± 0.2) nm. The periodicity between identical features within one row is estimated to be (0.50 ± 0.05) nm (= $\sqrt{3}\, a_{Au}$). In analogy to the comprehensive analysis of the low-coverage HS-6V6-SH adlayer discussed before we assign the dark rows to the positions of the alkyl chains in a fully extended all-trans conformation with the molecular axis parallel to the surface plane. The grey rows are attributed to the viologen moieties and the bright dots are assigned to the positions of the terminal sulfur functionalities. Using the vectors of the primitive gold lattice, a_{Au} and b_{Au} (Fig. 5-6 C), with $|a_{Au}| = |b_{Au}| = 0.2885$ nm as a basis, we propose the following unit cell in matrix notation $\begin{pmatrix} a \\ b \end{pmatrix} = \begin{pmatrix} 8 & 1 \\ -1 & 2 \end{pmatrix} \begin{pmatrix} a_{Au} \\ b_{Au} \end{pmatrix}$, which gives rise to $|a| = 2.46$ nm, $|b| = 0.5$ nm enclosing an angle $\alpha = 83.3^{o}$.

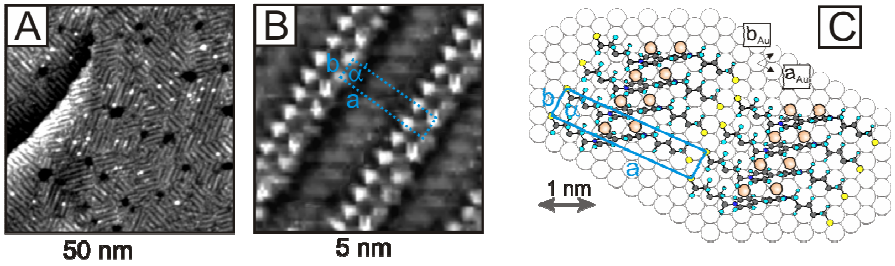

Fig. 5-6: (A) Large scale in situ STM image of the low coverage striped phase of HS-5V5-SH, E_S = -0.250 V, E_{bias} = 0.100 V, i_T = 60 pA; (B) High resolution of (A), E_S = -0.350 V, E_{bias} = 0.080 V, i_T = 40 pA; (C) Proposed packing model of the ordered striped phase.

The area per molecule is obtained as $A_L(STM) = 1.22\ nm^2$, which corresponds to a coverage of $\Gamma_L(STM) = 1.36 \times 10^{-10}$ mol cm^{-2}, which is smaller than in the low-coverage ordered 6V6 adlayer. The detailed characteristic data and the corresponding model parameters are summarized in Table 5-1.

5.3.3 Comparison of viologens (nVn, n = 5-8, 10)

Comparing 5V5 and 6V6 we found that their structures and unit cells are rather similar, except that the molecular length of 5V5 is smaller, resulting in a smaller value of the parameter a in the unit cell. In order to explore this trend further we carried out a series of experiments on the self-assembly of viologens with different length of hydrocarbon chain (n = 5-8, 10).

Employing the assembly strategies introduced for 6V6 (cf. Section 3.1.2 for details), we could successfully obtain three different adlayers, a low-coverage disordered, a low-coverage ordered striped structure and high-coverage phase, for all viologen molecules (nVn, n = 5-8, 10).

The STM images of the low-coverage ordered adlayers are composed of parallel rows of bright, dark grey and light grey contrast pattern. The width of the dark rows (corresponding to the carbon chain of molecules, cf. the analysis in chapter 5.3.1) increases with the length of carbon chains. The bright, and light gray contrast features appear to be not altered. The respective unit cells of HS-nVn-SH and H-nVn-SH are rather similar to HS-6V6-SH and H-6V6-SH respectively (cf. 5.3.1), except that the $|a|$ distance increases by 0.2885 nm, i.e. one gold lattice constant, with each additional $(-CH_2)_2$ groups. No odd-even effect was found. The characteristic unit cell parameters of the low-coverage striped phases of HS-nVn-SH on Au(111)-(1x1) are summarized in Table 5-1.

In situ STM images of viologen monothiols at high coverages revealed ordered structures with a $(\sqrt{7} \times \sqrt{7})$ R19.1° motif. A disordered adlayer was observed for viologen dithiols at high coverages. The adlayers show characteristic monatomic deep holes.

Table 5-1. Unit cell parameters of the low coverage striped phase of HS-nVn-SH on Au(111)-(1x1)

Viologens	a/nm	b/nm	α/°	Γ/10^{-10} mol cm^{-2}	A/nm^2
5V5	2.4 ± 0.3	0.50 ± 0.03	83 ± 3	1.4	1.2
	(2.5)	(0.5)	(83)	(1.3)	(1.2)
6V6	2.8 ± 0.3	0.50 ± 0.03	87 ± 8	1.2	1.4
	(2.8)	(0.5)	(84)	(1.2)	(1.4)
7V7	3.0 ± 0.3	0.50 ± 0.03	84 ± 5	1.1	1.5
	(3.0)	(0.5)	(84)	(1.1)	(1.5)
8V8	3.3 ± 0.3	0.50 ± 0.03	86 ± 7	1.0	1.6
	(3.3)	(0.5)	(85)	(1.0)	(1.6)
10V10	3.8 ± 0.5	0.50 ± 0.03	86 ± 4	0.88	1.9
	(3.9)	(0.5)	(86)	(0.85)	(1.9)

The experimentally determined values are plotted in the first line of each row. The numbers in parentheses represent the model parameters

In the studies above, we applied in situ STM in combination with cyclic voltammetry to explore the macroscopic electron transfer and the 2D assemblies of viologen monolayers on Au(111)/electrolyte interfaces. In the next paragraph, we will focus on electron transfer properties of nanoscale molecular junctions.

5.4 Single-molecule Conductance of HS-nVn-SH

5.4.1 i-Δs stretching experiments

The molecular conductance of HS-6V6-SH was measured by the repeated formation and breaking of molecular junctions between a Au STM tip and a Au substrate electrode modified with disordered viologen molecules. The sample was prepared according to protocol I (cf. section 3.1.2). We applied the so-called stretching method, which was described in section 3.5.1. Current–distance traces were acquired according to the following protocol: (1) after reaching a stable tunneling position at s_o (defined by i_o = 100 pA and a properly chosen bias voltage), the feedback was disabled, (2) the tip approaches the viologen-modified surface until (s_o – 1.0 nm), (3) the tip stays at (s_o – 1.0 nm) during a dwelling time of 100 ms to form molecular junctions, (4) recording of the current vs. distance characteristics upon retraction from (s_o – 1.0 nm) to (s_o + 2.0 nm) with a pulling rate of 2-6 nm s^{-1}, (5) stabilizing of the tip at s_o and switching on the feedback, (6) repetition of the cycle.

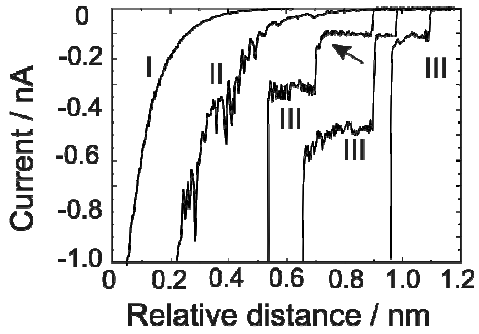

Fig. 5-7: Current-distance (i - Δs) "stretching" curves for HS-6V6-SH in 0.05 M $KClO_4$, pH = 7, at E_S = -0.250 V and E_T = -0.150 V. For clarity, individual traces are plotted with an offset in the distance scale.

Fig. 5-7 shows characteristic i-Δs stretching curves for molecular junctions Au(T)│HS-6V6-SH│Au(S) recorded at E_S = -0.250 V and E_T = -0.150 V in $0 < i \leq 100$ nA. We observed three types of transient curves during the stretching. Type I curves are characterized by a smooth exponential decay due to electron tunneling between the gold tip and the substrate. No molecular junctions were formed and the percentage of these decay curves was 50% - 80% (Fig. 5-7). Type II curves are noisy and non-monotonous (around 10%), which could be attributed to mechanical vibrations, acoustic noise or impurities [154]. Traces of type I and type II were rejected when constructing the conductance histograms. Type III conductance traces are monotonous and non-exponential (10% - 40%), and were used exclusively to build the histograms. They exhibit single or a series of plateaus which are separated by abrupt steps. The selection criteria are: minimum plateau length of 0.05 nm and an average variation of the current of less then 5 %.

The corresponding plateau currents are rather low, and cannot be attributed to the well-known conductance quantization of a metal nanowire [34]. Instead, we assign these current steps to the breaking of molecular junctions previously formed between the gold STM tip and the substrate [34,65]. This hypothesis is supported by the following observations: (1) Only exponentially decaying current-distance traces were found for the bare supporting electrolyte in $0 < i \leq 100$ nA. (2) The current–distance traces were rarely (< 2 %) found in experiments with HS-6V6-H, i.e. viologen-type monothiols capable to form a chemical bond only to one of the adjacent gold electrodes. (3) The plateau currents in the i–Δs curves (Fig. 5-7) were different for

different molecules, e.g. for molecules with different linker length, which show a distinct dependence on the applied electrode potential.

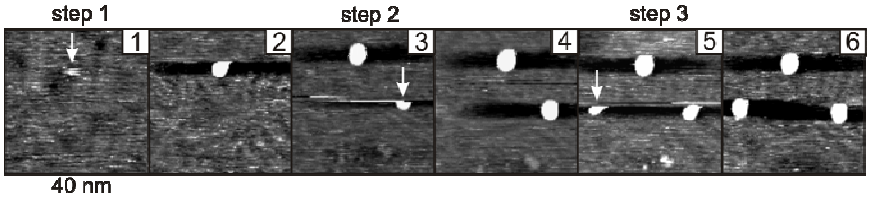

Fig. 5-8: Series of in situ STM images acquired simultaneously with three successive i – Δs traces for a disordered adlayer of HS-6V6-SH on Au(111) in 0.05 M $KClO_4$. The white arrows in the images with odd numbers represent the formation of small monatomically height gold islands immediately after the completion of an individual pulling event. The experiment was carried out at E_S = -0.250 V and E_T = -0.150 V, i_T = 100 pA.

During the stretching process we not only measure the current–distance traces, but also monitor simultaneously the surface morphology in situ STM imaging. Fig. 5-8 illustrates a characteristic STM sequence. The x – y positions of the individual transients are indicated by the arrows in the frames 1, 3 and 5 while the even-numbered frames show the same surface area with the newly created monoatomically high gold islands. We observed no indications of a tip crash. We favor the idea that these islands are the result of materials transfer from the gold STM-tip accompanied by the rupture of a large number of local molecular junctions.

5.4.2 Statistical analysis of the molecular conductance

For estimating the single junction conductance properties, we carried out a statistical analysis of the plateau currents and constructed histograms. The histograms were constructed based on a large number of individual type III stretching curves (Fig 5-7), typically more than 500 individual transients. A typical histogram obtained from data acquired at E_S = -0.250 V and E_T = -0.150 V was plotted in Fig. 5-9, which shows a characteristic series of peaks corresponding to one, two or three molecules in the gap. Fitting the histogram with Gaussians determines the peak centers and the full width at half maximum. These peak values are then plotted vs. the peak number. One obtains a linear relation. The slope gives the current of a single Au(T)│HS-6V6-SH│Au(S) junction. The data plotted in Fig. 5-9 yield 0.1 nA at a fixed bias of 0.100 V, which corresponds to the single-junction conductance of 1 nS for HS-6V6-SH.

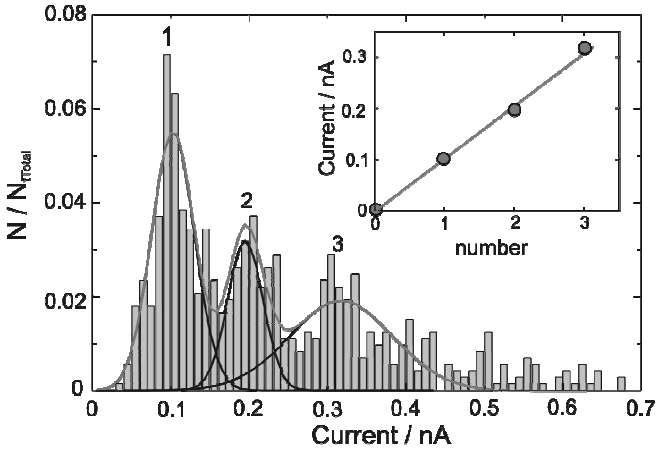

Fig. 5-9: (A) Histogram constructed from values of the plateau currents of more than 500 individual type III stretching curves for molecular junctions Au(T) │HS-6V6-SH│Au(S) recorded at E_S = -0.250 V and E_T = -0.150 V. The peak positions were determined by Gaussian fits (black lines) to the histogram peaks (blue line as the sum of the Gaussians). The inset shows the linear correlation between peak current and peak number.

5.4.3 Dependence of the junction conductance on the substrate potential

Systematic stretching experiments at various substrate potential E_S were carried out for single molecule junctions of Au(T) │HS-6V6-SH│Au(S). Histograms were constructed based on the analysis of i - Δs traces for substrate potentials in -0.750 V ≤ E_S ≤ -0.250 V, i.e. within the range of the process $V^{2+} \leftrightarrow V^{\bullet+}$, while keeping the bias voltage constant.

Fig. 5-10 shows the single-molecule conduction currents as a function of E_S at E_{bias} ($E_T - E_S$) = 0.100 V. The conductance is rather constant in the stability region of the oxidized viologen dication V^{2+}, increases at E_S < -0.400 V and appears to reach a plateau at E_S ≤ -0.700 V, i.e. past the formal potential of the reversible redox process $V^{2+} \leftrightarrow V^{\bullet+}$. We tentatively attribute the sigmoidal-type increase of the molecular conductance current to the higher electron density and the higher conjugation of $V^{\bullet+}$ compared with V^{2+}. This view is supported by force field calculations of Hester et al [155]. They reported that the inter-ring bond order increases when the viologen dication transforms into the radical upon reduction, which implies that the aromatic character extends across both rings for the latter compound.

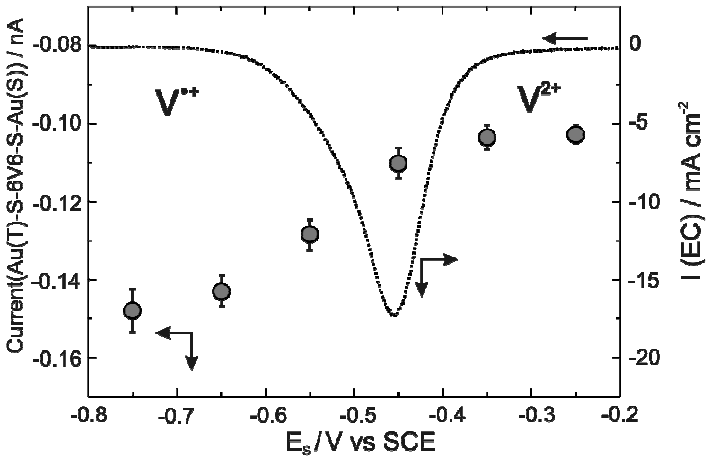

Fig. 5-10: Single molecule conduction currents of Au(T) │HS-6V6-SH│Au(S) junctions vs. the substrate potential E_S at fixed bias (E_T - E_S) = 0.100 V. The sign convention of the bias voltage gives the negative conduction currents. The dotted line corresponds to the macroscopic current-voltage curve for the reduction of $V^{2+} \rightarrow V^{\bullet+}$ (cf. cyclic voltammograms in Fig. 5-1).

5.4.4 Conductance of Au │nVn │Au junctions

In order to understand further the correlation of junction conductance and molecular structure, we investigated the single-molecule conductance within a series of viologens (HS-nVn-SH, n = 5-8) to explore the influence of the alkyl chain length on the transport characteristics.

5.4.4.1 HS-5V5-SH

Since the molecular conductance experiments of HS-nVn-SH (n = 5-8) employing the STM-based stretching method are similar to those already described for HS-6V6-SH, we will only present one selected result for HS-5V5-SH, and then concentrate on the comparison of the four viologens.

Fig. 5-11 shows a typical histogram for HS-5V5-SH obtained from a careful analysis of stretching experiments for E_S = -0.650 V and E_{bias} = 0.100 V. One observes a series of equally spaced current peaks, which represent one, two or three molecular junctions in the gap. The first peak in this plot is attributed to the conductance current of single-molecular junctions. The corresponding single-junction conductance is estimated to (5.2 ± 2.0) nS.

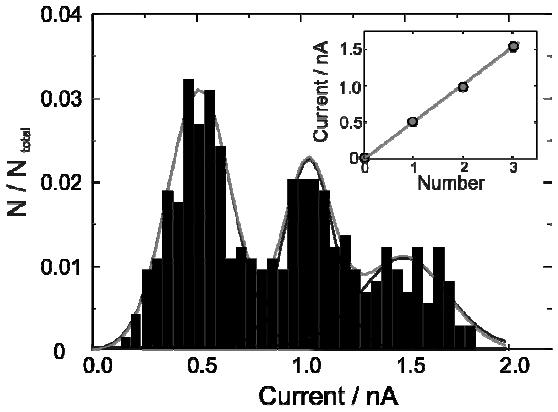

Fig. 5-11: Histogram for HS-5V5-SH on Au(111)-(1x1) in 0.05 M $KClO_4$, pH ~ 7 at E_S = -0.650 V, E_{bias} = 0.100 V. 335 type III stretching curves out of 1100 total current–distance curves were selected, bin width 0.05 nA. The solid black and blue lines represent the Gaussian fit.

5.4.4.2 Chain length dependence of the conductance (n = 5-8)

The above experiments were extended to substrate potentials in -0.700 V ≤ E_S ≤ -0.200 V for a series of viologen derivatives (HS-nVn-SH) with n = 5 to 8. The statistical analysis was carried out according to the strategy described above. The obtained conductance of single junctions Au(T) | HS-nVn-SH | Au(S) are plotted in Fig. 5-12 for E_S = -0.250 V and E_S = -0.650 V, i.e. for the viologens in the dication V^{2+} and the radical cation $V^{\bullet+}$ states. The numerical results are summarized in Table 5-2. The single-junction conductance of the "reduced" radical cation state is approximately 50% higher than the corresponding "oxidized" dication state. The logarithmic plots of the conductance G vs. the number of CH_2–units are linear for both oxidation states and follow a simple tunneling model with $G = G_{con} \exp(-\beta_N N)$, where β_N is the decay constant and the pre-exponential factor G_{con} is related to the metal | molecule contact. The parameters β_N and G_{con} were estimated as (0.76 ± 0.13) and (9 ± 2) μS for the viologen dication V^{2+} and (0.74 ± 0.13) respectively (10 ± 4) μS for the radical cation $V^{\bullet+}$. With the typical length contributions of 0.125 nm per CH_2-group in an all-trans alkyl chain one obtains β_{CH2} = (5.9 – 6.1) nm^{-1}.

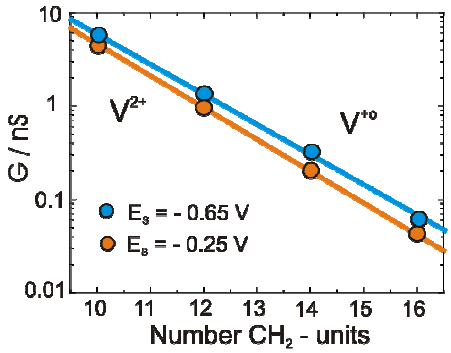

Fig. 5-12: Chain lengths dependence of the single junction conductance Au(T)│HS-nVn-SH│Au(S), n = 5 to 8, in 0.05 M $KClO_4$, pH ~ 7, for the oxidized V^{2+} and the reduced $V^{\bullet+}$ state of the viologen moiety.

The values of G_{con} scatter around 10 μS for both systems, and are rather independent of the redox state of the viologens. Comparing Au(T)│HS-nVn-SH│Au(S) and Au(T)│HS-C_m-SH│Au(S) junctions with the same number of CH_2-units, i.e. m = 2n [156], we found that the single-molecule conductance of the former is one to two orders of magnitude larger than the latter, and that this difference increases with increasing chain length. In an attempt to rationalize this result we assume that the single molecule conductance of the two types of junctions, $G_{HS\text{-}Cm\text{-}SH}$ and $G_{HS\text{-}nVn\text{-}SH}$, is given by the following expressions [157,158]:

$$G_{HS\text{-}Cm\text{-}SH} = T_{conT} \cdot T_{Cm} \cdot T_{conS} \cdot G_o \quad (5.1)$$

$$G_{HS\text{-}nVn\text{-}SH} = T_{conT} \cdot T_{Cn} \cdot T_{BP} \cdot T_{Cn} \cdot T_{conS} \cdot G_o \quad (5.2)$$

Here, T_{conT} , T_{Cm} and T_{conS} represent the transmission functions for the contacts between the Au tip and the alkyl chain (Au(T)│-S-│C_m), the alkyl chain (-S-│C_m│-S-) as well as the contact between the alkyl chain and the substrate (C_m│-S-│Au(S)). The viologen-type junction requires two additional factors representing the transmission functions of the bipyridyl moiety T_{BP} (-CH_2-│BP│-CH_2-) and of the alkyl chains between the sulfur and the pyridyl functionality, T_{Cn} (-S-│$(CH_2)_n$│-BP). G_o = 77 μS is the quantum conductance [34]. The contributions of T_{conT} and T_{conS} are expected to be similar for both junctions because they represent identical Au-S bonds, and the sulfurs being attached to saturated alkyl chains. The conductance contribution of T_{Cm} appears to decrease more rapidly with increasing number of CH_2–units than $T_{Cn} \cdot T_{BP} \cdot T_{Cn}$. We propose two hypotheses to rationalize this trend: (i) First, the presence of the viologen moiety suppresses gauche defects and facilitates an all-trans

conformation of the alkyl chains, which is known to exhibit a higher conductance [157]. (ii) Second, the increasing length of the symmetrically arranged alkyl side chains might impose a gradually increasing preferential coplanar alignment of the two pyridyl rings, which also enhances the conductivity [159].

Table 5-2. Single-junction conductance (in nS) for the oxidized (V^{2+}, E_S = -0.250 V) and the reduced state ($V^{\bullet+}$, E_S = -0.650 V) of Au(T) │HS-nVn-SH│Au(S) in 0.05 M $KClO_4$, pH ~ 7.

nVn	**5**	**6**	**7**	**8**
V^{2+}	3.90 ± 0.10	1.00 ± 0.02	0.21 ± 0.01	0.040 ± 0.001
$V^{\bullet+}$	5.22 ± 0.12	1.43 ± 0.03	0.34 ± 0.01	0.060 ± 0.002

5.5 Tunneling Spectroscopy of Redox-Active Viologens

Based on the knowledge we gained in measuring conductance of molecular junctions with the stretching method (i-Δs spectroscopy), we constructed tunneling junctions modified with (single) redox molecules and carried out I-V spectroscopic measurements.

5.5.1 I-V Spectroscopy at constant E_{bias}

The experiments started with a HS-6V6-H-modified gold substrate or STM tip in 0.5 M $LiClO_4$, pH ~ 8.5. We have chosen the viologen monothiol as the redox-active reactant to ensure a single anchoring possibility. After stabilization of the tunneling junction at a preset value of i_o, the tunneling feedback was switched off, and the current response was measured upon sweeping tip and substrate potentials simultaneously while keeping the bias voltage $E_{bias} = E_T - E_S$ constant. In other words, we changed the Fermi levels of tip and substrate relative to the molecular redox level. For further details of the experimental set-up we refer to section 3.5.2.

Fig. 5-13 shows the tunneling current versus the tip potential (E_T) recorded for the junction Au(S)-S-6V6-H│Au(T) at fixed bias ($E_T - E_S$) = 0.100 V. The black trace represents the average of 10 independent half cycles recorded when scanning the tip potential from -0.650 V and -0.270 V (positive direction) with a scan rate 0.5 V s^{-1}

and the feedback switched off. The tip voltammogram (orange curve) was recorded as background curve with the same scan rate (0.5 V s^{-1}) and in the same potential window in the absence of tunneling.

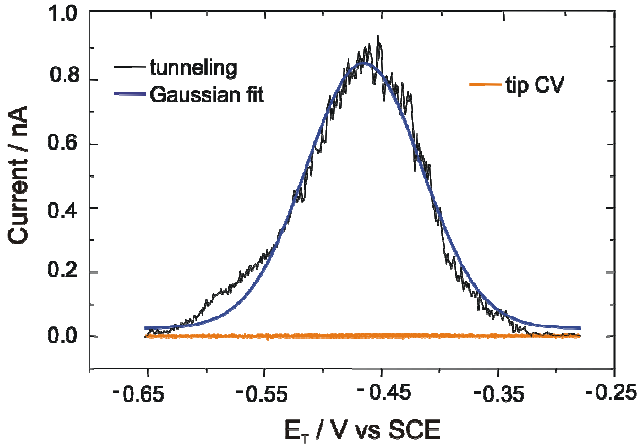

Fig. 5-13: Tunneling current vs. tip potential (EC-IV spectroscopy) recorded in 0.5 M $LiClO_4$, pH ~ 8.5 for the tunnel junction Au(S)-S-6V6-H │Au(T). E_{bias} = 0.050 V, i_T = 0.1 nA, scan rate: 0.5 V s^{-1}.

The tunneling curve in Fig. 5-13 shows a well-defined maximum i_M = (0.88 ± 0.10) nA at E_M = -(0.47 ± 0.02) V, which is close to the equilibrium potential of the one-electron redox process $V^{2+} \leftrightarrow V^{\bullet+}$ (see 5.2.1). The current decreases significantly at $|E_S - E_M| > 0.10$ V and approaches the initially preset tunneling current of 100 pA. This consistency illustrates the sufficient stability of the viologen-modified tunnel junction during the sweep experiment. The $i_T - E_T$ characteristics can be modeled by a Gaussian peak function as shown in Fig. 5-13. The maximum current at E_M is significantly larger than the electrochemical background signal (on/off ratio ≥ 70) and can be attributed convincingly to an enhanced tunneling response. Control experiments with bare gold surfaces and substrates modified with inactive dodecanethiol did not produce these features.

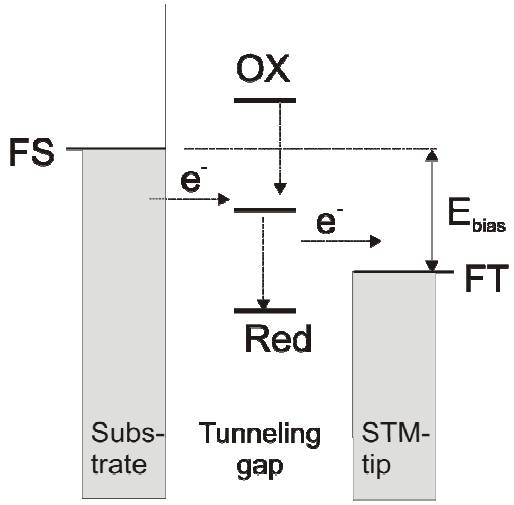

Fig. 5-14: Schematic electronic energy diagram of the two-step electron transfer mechanism for a redox molecule in EC-STM configuration. FS and FT represent the Fermi levels of substrate and tip, respectively. Tunneling occurs from the negatively (substrate) to the positively (tip) biased electrode via the molecular redox level.

The appearance of the maximum in the tunnel current can be rationalized as follows [123]: The formation of a junction Au(S)-S-6V6-H ⎪ Au(T) implies that a molecule with discrete electronic levels is located in the gap between substrate and tip, both representing continuous distributions of electronic levels. The localized electronic states are broadened by interactions of the redox-center with the surrounding electrolyte [160,161], and with the substrate [162]. Variation of the overpotential at fixed bias ($E_T - E_S$) is equivalent to a parallel shift of the Fermi levels of tip and substrate. The current first rises as the redox level approaches one of the Fermi levels (here the substrate Fermi level). Further increase leads to the current decrease as vacant levels of the positively biased electrode become increasingly thermally inaccessible. The position of the tunneling current maximum provides criteria to distinguish between different mechanisms of electron transfer (ET) [54,123,163-165]. Resonance tunneling [54,164] and a mechanism based on coherent two-step ET [123,163] predict a maximum in the tunneling current, but in both cases it is expected to be shifted from the equilibrium potential by the reorganization Gibbs free energy. A maximum located exactly at the equilibrium potential is predicted for a sequential two-step ET if the bias potential drop at the site of the redox-center is close to half the total potential drop ($E_T - E_S$) [165]. This theoretical treatment considers the ET in a redox-molecule functionalized tunneling junction as two consecutive interfacial single ET steps with vibration relaxation between the steps. The process comprises a cycle of consecutive molecular reduction and re-oxidation. Tentatively

we favor the sequential two-step ET mechanism to explain the experimental i_T vs. E_T characteristics of the Au(S)-S-6V6-H ⎪ Au(T) tunnel junction.

5.5.2 Bias dependence of the resonance peak potentials

The two-step electron transfer theory developed by Ulstrup and Kuznetsov et al. considers the ET in a redox-molecule functionalized tunneling junction as two consecutive interfacial single-electron transfer steps with vibrational relaxation between the steps. The theory predicts correlations between the tunneling resonance peak (E_M) and the applied bias voltage (E_{bias}) [123,166]:

$$i_T = \frac{1}{2} e\kappa\rho(eE_{bias}) \frac{\omega_{eff}}{2\pi} \exp\left(-\frac{\lambda - eE_{bias}}{4k_BT}\right) \left[\cosh\left(\frac{\left(\frac{1}{2}-\gamma\right)eE_{bias} - e\xi(E-E^{\circ})}{2k_BT}\right)\right]^{-1} \quad 5.1$$

here, κ is the electronic transmission coefficient, ρ is the density of electronic levels in the metal, ω_{eff} is the characteristic nuclear vibrational frequency, λ is the reorganization free energy, η (= E - E_0) is the electrochemical overpotential, i.e. the difference between the sample and equilibrium potentials, and γ and ξ are the fractional potential drops of bias and sample overpotential at the redox center.

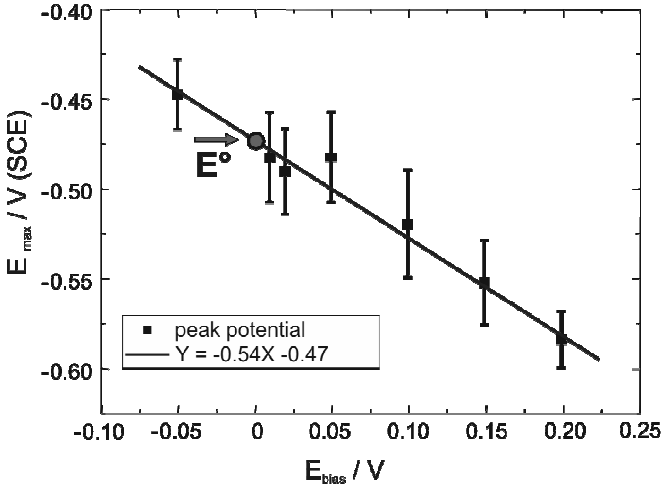

Fig. 5-15: Dependence of the tunneling resonance peak potentials (E_{max}) on the bias voltage for the tunnel junction Au(S)-S-6V6-H ⎪ Au(T) in 0.5 M $LiClO_4$, pH ~ 8.5 solution. Each data point represents 10-20 individually measured i-E_T curves. The blue line represents the result of the linear fit. The red point shows the electrochemical equilibrium potential.

The above theory was initially applied to redox-active proteins and metal transition complexes [123,166,167]. Fig. 5-15 shows the linear correlation between the maximum of the tunneling resonance and the applied bias voltage, which supports the validity of the two-step ET model represented by eqn. 5-1.

5.5.3 I-V Spectroscopy at variable bias voltage

The success in the first type of tunneling resonance experiments motivated us to extend the experimental approach towards variable bias values, i.e. the bias voltage E_{bias} is swept instead of the substrate potential E_S. These experiments were carried out with a HS-6V6-H modified gold substrate and a bare gold tip.

Fig. 5-16 shows the tunneling current versus potential bias (i_T-E_{bias}) curves of HS-6V6-H on Au(111) in 0.5 M $LiClO_4$, pH = 8.5. The initial experimental conditions are: tunneling current setpoint i_T = 0.05 nA, E_S = -0.200 V, tip potential E_T = -0.250 V. Then the tunneling current was recorded during scanning the tip potential from -0.250 V to -0.600 V, and from -0.250 V to 0.200 V, scan rate of 1 V s^{-1}. The feedback was switched off, and the substrate potential E_S was kept constant. Consequently, the bias voltage was changed negatively from E_{bias} = -50 mV to -400 mV, and from -50 mV to 400 mV. In the tip potential range of -0.200 V to 0.200 V (corresponding to 0.000 – 0.400 V for E_{bias}), in which there is no electrochemical redox process of the viologen species, the current response (Fig. 5-16) is the quasi-linear. However, when scanning the tip potential more negative, and therefore approaching the viologen-based redox process $V^{2+} \leftrightarrow V^{\bullet+}$, an increase of the tunneling current was observed for the forward and the backward sweeping directions.

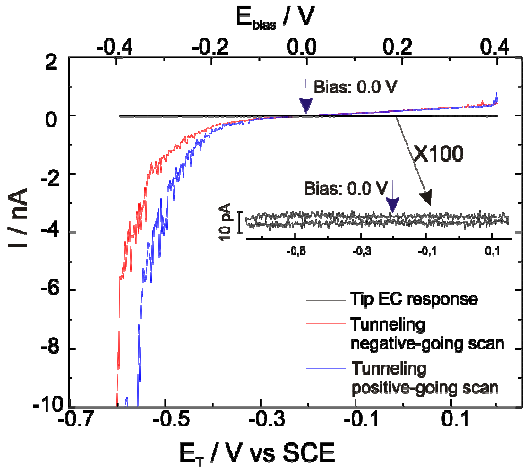

Fig. 5-16: (A) Diode-like tunneling response of HS-6V6-H on Au(111) in 0.5 M $LiClO_4$, pH = 8.5 by i-E_{bias} spectroscopy. Tunneling current setpoint i_T = 0.05 nA, E_S = -0.200 V, initial tip potential E_T = -0.250 V. Scan rate: 1 V s^{-1}. The inset shows the tip CV recorded in the same potential window and with the same scan rate.

Comparing the current response at negative (tunneling enhancement) and positive (quasi-linear current-bias voltage curve) bias voltage (Fig. 5-16 red and blue curves), one observes an apparent diode-like behavior of the tunneling current. For reference, we also measured the current-voltage curve of the tip outside the tunneling junction by withdrawing the tip. No enhanced current signal was observed. Clearly, the apparent diode-like response is not related to a purely electrochemical response of the tip, but rather to an enhanced tunneling resonance due to the alignment of molecular levels with the Fermi level of the tip. The enhancement leads to an on/off ratio of 70 at $|E_{bias}|$ = 0.400 V.

5.6 Summary and Conclusions

A comparative study on the redox activity of tailored viologens immobilized on gold electrodes has been carried out by applying in situ scanning tunneling microscopy (STM) and spectroscopy (STS) in combination with classical voltammetry in an electrochemical environment.

Firstly, the self-assembly and redox properties of viologen derivatives, HS-nVn-H and HS-nVn-SH (n = 5-8, 10), immobilized on Au(111)-(1x1) electrodes were

investigated by in situ scanning tunneling microscopy (STM) and cyclic voltammetry. The strict elimination of oxygen exposure during the assembly and the design of characteristic assembly protocols (time, concentration, temperature) allowed creating three distinct types of supramolecular adlayers for all viologens: (1) a low-coverage *disordered* and a low-coverage *ordered* "striped" phase of flat-oriented molecules, and a high-coverage monolayer composed of tilted viologen moieties. For the low-coverage phase, 2D ordered adlayer structures were monitored by in situ STM for various viologens with different spacer lengths (HS-nVn-SH and HS-nVn-H, n = 5-8, 10) and corresponding structural models were proposed. Ordered high-coverage adlayers were found for the viologen monothiols, but no ordered structure was observed for the corresponding viologen dithiols in the present studies.

Secondly, in situ STM was employed to explore electron transport properties of single-molecule junctions Au(T) │HS-nVn-SH │Au(S). The junction conductance of a series of viologen molecules were estimated based on current–distance stretching measurements and a careful statistical analysis. We found that the single-junction conductance of HS-nVn-HS in the reduced radical cation state is approximately 50% larger than the dication state. The observed sigmoidal potential dependence of the single molecule conductance, measured at variable substrate potentials E_S, was attributed to electronic structure changes of the viologen moiety during the one-electron reduction/oxidation process $V^{2+} \leftrightarrow V^{\bullet+}$. The simultaneous recording of in situ STM images and successive i–Δs traces revealed structural insight into the nature of the "stretching" experiment.

The single-junction conductance of viologens decreases exponentially with the length of the CH_2 spacer units giving rise to a tunneling decay constant of β = 5.9 to 6.1 nm^{-1}. Comparing Au(T) │HS-nVn-SH │Au(S) and Au(T) │HS-C_m-SH │Au(S) junctions with the same number of CH_2–units, i.e. m = 2n, one deduces that the single-molecule conductance of the former is one to two orders of magnitude larger than the latter, and that this difference increases with increasing chain length. The difference is attributed to conformational changes between these junctions. The contact conductance is estimated as 10 μS for viologens and alkanedithiols.

Thirdly, tunneling spectroscopy experiments in STM-based junctions Au(S)-S-6V6-H │Au(T) resulted in tunneling current–substrate potential (i_T-E_S) curves with a

well-defined maximum located at the equilibrium potential of the redox-process V^{2+} $\leftrightarrow$ $V^{\bullet+}$. The second type of tunneling experiment (i_T-E_{bias}) shows a diode-like type of the tunneling response with an on/off ratio $\geq$ 70. The tunneling resonance characteristics of the viologen-modified tunneling junction were tentatively attributed to a sequential two-step electron transfer mechanism

.

Chapter 6. Conclusions

In situ scanning tunneling microscopy (STM) and spectroscopy (STS) were employed, in combination with macroscopic electrochemical techniques and infrared spectroscopy (ATR-SEIRAS) to explore the two-dimensional self-assembly, structure transitions and local reactivity of two molecular systems at electrified Au(111)/aqueous electrolyte interfaces: (i) The interfacial properties of trimesic acid adlayers (TMA) were compared with those of the related aromatic carboxylic acids: benzoic acid (BA), isophthalic acid (IA) and terephthalic acid (TA). (ii) macroscopic and nanoscale studies of electron transport properties were carried out employing a series of custom-synthesized mono- and dithiol viologen derivatives ((N-alkyl-N'-(n-thioalkyl)-4,4'-bipyridinium bromide, HS-nVn-H, and N,N'-bis(n-thioalkyl)-4,4'-bipyridinium bromide, HS-nVn-SH).

Depending on the applied electric field, TMA forms five distinctly different, highly ordered supramolecular adlayers on Au(111) surfaces. We have characterized their real-space structures at the molecular scale. In the potential range -0.250 V < E < 0.200 V planar-oriented TMA molecules form a hexagonal open-ring honeycomb structure, $\begin{pmatrix} 6 & 6 \\ 0 & 6 \end{pmatrix}$, a hydrogen-bonded ribbon-type phase, $\begin{pmatrix} 10 & -4 \\ 7 & 7 \end{pmatrix}$, and a herringbone-type phase, $\begin{pmatrix} 14 & 0 \\ 7 & 13 \end{pmatrix}$, all stabilized by directional hydrogen bonds and weak substrate–adsorbate interactions. For 0.200 V ≤ E < 0.400 V, i.e. around the potential of zero charge, and at slightly higher coverages a close-packed physisorbed adlayer of hydrogen-bonded TMA dimers, $\begin{pmatrix} 0 & 5 \\ 4 & 4 \end{pmatrix}$, was observed. Further increase of the electrode potential to positive charge densities causes an orientation change from planar to upright, giving rise to a stripe-like chemisorbed and perpendicularly oriented TMA adlayer with $\begin{pmatrix} 3 & 0 \\ 4 & 8 \end{pmatrix}$.

Self-assembly studies of TMA-related aromatic carboxylic acids lead at negative charge densities to zigzag tapes, 1-D linear tapes and tetrameric structures

for physisorbed adlayers of IA, TA and BA respectively. The structure determining units (synthon) are hydrogen-bonded dimers. A structural transition leads to a tilted or perpendicular molecular orientation at more positive potentials (or charge densities).

The comparison of our in situ STM investigations with infrared measurements for the high coverage phases (perpendicularly adsorbed orientation) of TMA with IA and BA leads to the conclusion that only one carboxylate group per molecule is bound to the positively charged electrode surface. The remaining, protonated carboxyl groups (TMA, IA) are directed toward the electrolyte and act as structure-determining components of a hydrogen-bonded two-dimensional ladder-type network.

The second part of the work is focused on a systematic investigation of the assembly and the macroscopic redox properties of viologen derivatives (HS-nVn-SH and HS-nVn-H, n = 5-8, 10) on Au(111)-(1 x 1) in 0.05 M $KClO_4$, pH ~ 7. Three different adlayer phases were created for all viologen molecules: a low-coverage disordered and a low-coverage striped phase of flat oriented molecules, and a high-coverage phase of upright or slightly tilted molecules. Using the primitive gold lattice as a basis, one could represent the commensurate HS-5V5-SH striped phase in matrix notation by $\begin{pmatrix} a \\ b \end{pmatrix} = \begin{pmatrix} 8 & 1 \\ -1 & 2 \end{pmatrix} \begin{pmatrix} a_{Au} \\ b_{Au} \end{pmatrix}$. Supramolecular structures of the other viologens are similar, except that the length of the rectangular unit cell increases with increasing length of the alkyl chains with 0.2885 nm for each additional $(CH_2)_2$ unit.

In situ STM was then employed to explore electron transport properties of redox-active viologens at the nanoscale level. The single molecular conductances of tailored Au | viologen | Au junctions have been estimated on the basis of a statistical analysis of individual current–distance traces. Three types of conductance traces were observed, exponential ones, non-monotonous and noisy curves as well as monotonous step-like “stretching” curves. The latter were chosen for the statistical analysis to extract single junction conductance properties.

The single-junction conductance of N,N´-bis(n-thioalkyl)-4,4´-bipyridinium bromide in the reduced radical cation state is approximately 50 % larger than the oxidized dication state, which is attributed to electronic structure changes of the viologen moiety during the one-electron transfer process $V^{\bullet+} \leftrightarrow V^{2+}$. The

simultaneous recording of in situ STM images and successive current–distance traces revealed structural insight into the nature of the "stretching" experiment. The conductance decreases exponentially with the length of the CH_2 spacer units giving rise to a tunneling decay constant of β_{CH2} = 5.9 to 6.1 nm s^{-1}. The contact conductance was estimated as 10 μS.

Tunneling spectroscopy experiments in STM-based junctions Au(S)-S-6V6-H │Au(T) resulted in tunneling current–overpotential (i_T-E_S) curves with a well-defined maximum located at the equilibrium potential of the redox-process $V^{\bullet+} \leftrightarrow V^{2+}$. Variation of the bias voltage shows a diode-like tunneling response in i_T-E_{bias} curves with an on/off ratio ≥ 70. The tunneling resonance characteristics of the viologen-modified junction were tentatively attributed to a sequential two-step electron transfer mechanism.

A. List of Figures, Schemes, and Tables

List of Figures

List of Schemes and Tables

B. List of Symbols and Abbreviations

2D	two dimensional
3D	three dimensional
A	electrode area
AFM	atomic force microscopy
ATR	attenuated total reflection
BA	benzoic acid
C^b	bulk concentration
CE	counter electrode
CV	cyclic voltammogram, cyclic voltammetry
E_{bias}	bias voltage
EC	electrochemical, electrochemistry
EC-STM	electrochemical scanning tunneling microscopy
EDL	electrochemical double layer
E_M	tunneling resonance peak
E_{pa}	anodic peak potential
E_{pc}	cathodic peak potential
E_r	reference potential
E_S	substrate potential
E_T	tip potential
ET	electron transfer
F	the Faraday constant, 96485 C mol^{-1}
FePP	iron protoporphyrine
FWHM	full width at half maximum
G_0	quantum conductance
h	plank constant
HOMO	highest occupied molecular orbital
HOPG	highly oriented pyrolytic graphite
i_a	anodic current
IA	isophthalic acid
i_c	cathodic current
IHP	inner Helmholtz plane
i_{pa}	anodic peak current
i_{pc}	cathodic peak current
IR	infrared
K_a	acid dissociation constant
LEED	low energy electron diffraction
LSV	linear sweep voltammetry
LT-STM	low temperature scanning tunneling microscopy
LUMO	lowest unoccupied molecular orbital
m	mass weight
MCJ	mechanically controllable break junctions
MSE	mercury sulfate electrode
n	number of electrons
NHE	normal hydrogen electrode
nVn	viologens (n = 5-8, 10)

OHP	outer Helmholtz plane
Ox	the oxidized partner of a redox couple
PP	protoporphyrine
PZC	potential of zero charge
q	electron charge
QCM(EQCM)	(electrochemical) quartz crystal microbalance
RE	reference electrode
Red	the reduced partner of a redox couple
RHE	reversible hydrogen electrode
s	tunneling distance
SAM	self-assembled monolayer
SCE	saturated calomel electrode
SEIRAS	surface enhanced infrared absorption spectroscopy
SHG	second harmonic generation
SPM	scanning probe microscopy
STM	scanning tunneling microscopy
STS	scanning tunneling spectroscopy
T	temperature
t	time
TA	terephthalic acid
THE	trapped hydrogen electrode
TMA	trimesic acid
TOC	total organic carbon
UHV	ultra high vacuum
UPD	under-potential deposition
v	potential scan rate
V	applied voltage
$V^{\bullet+}$	viologen radical monocation
V^{0}	neutral form of viologen
V^{2+}	viologen dication
WE	working electrode
XPS	X-ray photoelectron spectroscopy
η	over potential
ΔE_p	voltage separation of anodic and cathodic current peaks
Δs	relative distance
Γ	surface coverage of adsorbed species
ρ	the density of electronic levels in metal
ω_{eff}	characteristic nuclear vibrational frequency
ξ	fractional potential drop of overpotential
Φ	barrier height
$\varnothing$	diameter
γ	fractional potential drops of bias
λ	reorganization free energy
ν	stretching vibration mode
θ	occupied sites fraction of surface

C. Acknowledgements

I cannot imagine that the achievements of this thesis could have become a reality without the constant support, encouragements and help from my advisor, colleagues and family through all these years. These people have become a precious memory during this unforgettable period of my Ph.D. studies in Jülich.

First of all, I would like to thank my thesis advisor PD Dr. habil. Thomas Wandlowski for his credible instructions, patient help and regular discussions from the design of the experiments to the writing of this thesis. His broad vision on electrochemistry and insight in the frontiers of nanoscience has impressed me deeply and given me the inspiration and courage to overcome the challenges on my research topics. Without his help and instructions I would not have made it through my Ph. D. studies! Even now, I still cannot forget how excited we were after the successful Cu UPD experiments with his hand-on instruction in 2003 when I first joined this group. I always felt appreciated through his care and help, especially at the beginning of my stay in Jülich, the first time for me in a foreign country.

I also would like to acknowledge Prof. Ulrich Simon from the RWTH-Aachen. It is my great pleasure to have him as referee of my dissertation. I also wish to thank Prof. Dr. Georgi Staikov for the questions, suggestions and discussions during my presentations in the IBN3, which made me think deeper about my research topics.

I thank Prof. Li-Jun Wan for bringing the nanoworld closer to me and giving me the initial training with EC-STM as well as recommending me to join the current group for diving deeper in my scientific fields. I am thankful to Prof. N. J. Tao for his inspiring lectures at the Wittenberg summer school and the elucidating discussions during his visits in Jülich.

Dr. Gabor Nagy is a person I should thank since he taught me the whole procedure to prepare a nice STM experiment, and helped me to have a good start here.

I also thank Bo, one of my best colleagues and friends in Jülich, for his cooperation in my Ph.D work as well as for the unforgettable time we spent together. As the chairman of the Chinese community in Jülich, he really helped me in many aspects.

The same thanks I give to Ilya, who is a master of the computer. With him in the office I don't have to worry about my computer and can really concentrate on science. He also helped me to finalize this thesis.

Special thanks must be given to Stijn for helping me with proof-reading my thesis. He is such a kind gentleman, not to mention the many valuable suggestions on the scientific topics, and his patience in correcting many typos without a single word of complaint!

I also thank Masanori for helping me with the final proof-reading. He is a good friend and always open to help whenever I asked.

Many thanks to my colleagues in the group of Dr. Wandlowski, previous and present, for their help and cooperation. Their names are: Sergey Pronkin, Guijin Su, Gabor Meszaros, I1-Cheol Jeon, Chen Li, Rocio Aguilar-Sanchez, Alex Putz and Renata Bujak.

I am thankful to Mr. Udo Linke from the IBN3 for the help with the preparation of gold single crystals. I also would like to acknowledge Prof. Tamas Tajmossy and Dr Gabriella Lendvay-Gyorik from the Institute of Chemistry, Hungarian Academy of Sciences, Budapest, for teaching me about electrochemical impedance during the 2006 summer school in Hungary. Prof. Macel Mayor and Dr. Alfred Blaszczyk are specially acknowleged for their effort in synthesizing the tailored viologen molecules. I thank Prof. Jens Ulstrup and Dr. Qijin Chi from Technical University of Denmark for their discussions with tunneling spectroscopy and electron transfer topics.

For their kind help and continuous support in many aspects, I would like to thank Ms. Sonja Körner, Ms. Marina Tödt, Ms. Mirjam Gruber, Mr. Friedhelm Schmitz, Mr. Wolfgang Rubner, Mr. Rainer Rausch, Mr. Norbert Tiefes and Mr. Sascha Thiele.

Last but not least, I thank Mrs. H. Acker-Mantel and Ms. Roswitha Bley from the international office for their patience and work.

The financial support from the Volkswagen Foundation, the HGF Project “Molecular Switches”, the Research Center Juelich, the Institute of Functional Molecular Systems for Information Technology (IFMIT), and the Center of Nanoelectronic Systems for Information Technology (CNI) are gratefully acknowleged.

D. Publications during PhD Work

Li, Z.; Han, B.; Meszaros, G.; Pobelov, I.; Wandlowski, Th.; Błaszczyk, A.; Mayor, M.
"Two-dimensional assembly and local redox-activity of molecular hybrid structures in an electrochemical environment"
FARADAY DISCUSSION, 131: 121-143, 2006.

Li, Z.; Han, B.; Wan, L. J.; Wandlowski, Th.
"Supramolecular nanostructures of 1,3,5-benzene-tricarboxylic acid at electrified Au(111)/0.05 M H_2SO_4 interfaces: an in situ scanning tunneling microscopy study"
LANGMUIR, 21 (15): 6915-6928, 2005.

Li, Z.; Pobelov, I.; Han, B. Wandlowski, Th.; Błaszczyk, A.; Mayor, M.
"Conductance of redox-active single molecular junctions: an electrochemical approach"
NANOTECHNOLOGY, 18: 044018, 2007.

Han, B.; **Li, Z**.; Pronkin, S.; Wandlowski, Th.
"In situ ATR-SEIRAS study of adsorption and phase formation of trimesic acid on Au(111-25 nm) film electrodes"
CANADIAN JOURNAL OF CHEMISTRY-REVUE CANADIENNE DE CHIMIE, 82 (10): 1481-1494, 2004.

Han, B.; **Li, Z**.; Wandlowski, Th.
"Adsorption and self-assembly of Aromatic carboxylic acids on Au/electrolyte interfaces"
ANALYTICAL & BIOANALYTICAL CHEMISTRY, in press, 01/2007.

Su, G. J.; Aguilar-Sanchez, R.; **Li, Z**.; Pobelov, I.; Homberger, M.; Simon, U.; Wandlowski, Th.
"Scanning tunneling microscopy and spectroscopy studies of ω–(4'-methyl-biphenyl-4-yl) alkanethiols on Au(111)-(1x1)"
Chem. Phys. Chem. In press, 2007.

Pobelov, I.; Li, C.; **Li, Z**.; Wandlowski, Th.
"Single molecule conductivity of alkanethiols at electrified solid/liqid interface-an in situ STM approach"
In preparations, 2007.

E. Curriculum Vitae

Zhihai Li

Born on 22 December, 1971, in Heilongjiang Province, China

Childhood and all school years in Heilongjiang Province, China

Nationality: Chinese

EDUCATION

09/87—07/90 Tangyuan Senior High School
Graduation: 07/90

09/90—07/94 Department of Chemistry, Jilin University
Major (specialty): Chemistry (Polymer materials and engineering)
Degree: B.S
Supervisor: Prof. Fenglan Bian

09/94—07/97 Department of Chemistry, Jilin University
Major (specialty): Chemistry (Inorganic Chemistry)
Degree: M.S
Supervisor: Prof. Yan Yan, Prof. Guodong Zheng

WORKING EXPERIENCE

09/91-07/96 Part-time tutor, Courses: Chemistry, Physics, Mathematics, and English, Department of Chemistry, Jilin University

09/95-07/96 Teaching assistant. Courses: inorganic chemistry and experiment Department of Chemistry, Jilin University

07/97-06/02 Engineer, China Youth Center For High-Technology, Beijing

07/02-02/03 Research assistant at the Key Laboratory of Molecular Nanostructures and Nanotechnology, Institute of Chemistry, Chinese Academy of Science (CAS).
Supervisor: Prof. Li-Jun Wan

02/03-present Ph. D candidate in Institute of Bio- and Nanosystems (IBN3), Research Center Jülich GmbH
Supervisor: PD Dr. habil. Thomas Wandlowski

F. List of References

1 Peercy, P. S. Nature 2000, 406, 1023.

2 Nitzan, T. in “Molecules: Building Blocks for Future Nanoelectronics”, Lectures of 5th International Wilhelm and Else Heraeus summer school; Wittenberg, 2004.

3 Meindel, J. D.; Chen, Q.; Davis, J. A. Science 2001, 293, 2044.

4 Klein, D. L.; Roth, R.; Lim, A. K. L.; Alivisatos, A. P.; McEuen, P. L. Nature 1997, 389, 699.

5 a) Barth, J. V.; Costantini, G.; Kern, K. Nature 2005, 437, 671; b) Barth, J. V. in “Molecules: Building Blocks for Future Nanoelectronics”, Lectures of 5th International Wilhelm and Else Heraeus summer school; Wittenberg, 2004.

6 Bernard, J. F.; Lopatin, S. D. Patent number: 6,465,567 B1, Oct. 15, 2002.

7 Kind, H.; Bonard, J.-M.; Emmenegger, C.; Nilsson, L.-O.; Hernadi, K.; Maillard-Schaller, E.; Schlapbach, L.; Forró, L.; Kern, K. Adv. Mater. 1999, 11, 1285.

8 Tans, S. J.; Devoret, M. H.; Groeneveld, R. J. A.; Dekker, C. Nature 1998, 394, 761.

9 Zhang, S. Materials Today 2003, 6, 20.

10 Whitesides, G. M.; Boncheva, M. PNAS 2002, 99, 4769.

11 Lehn, J.-M. Supramolecular Chemistry: Concepts and Perspectives; Wiley-VCH: Weinheim, 1995.

12 Desiraju, G. R. Nature 2001, 412, 397.

13 Gerber, C.; Lang, H. P. Nature Nanotechnology 2006, 1, 3.

14 Love, J. C.; Estroff, L. A.; Kriebel, J. K.; Nuzzo, R. G.; Whitesides, G. M. Chem. Rev. 2005, 105, 1103.

15 Schreiber, F. Progress in Surface Science 2000, 65, 151.

16 Ruben, M.; Payer, D.; Landa, A.; Comisso, A.; Gattinoni, C.; Lin, N.; Collin, J.-P.; Sauvage, J.-P.; de Vita, A.; Kern, K. J. Amer. Chem. Soc. 2006, 128, 15644.

17 Hoeben, F. J. M.; Jonkheijm, P.; Meijer, E. W.; Schenning, A. P. H. J. Chem. Rev. 2005, 105, 1491.

18 Whitesides, G. M. Science 2002, 295, 2418.

19 Yang, G.; Liu, G.-Y. J. Phys. Chem. B 2003, 107, 8746.

20 Poirier, G. E.; Pylant, E. D. Science 1996, 272, 1145.

21 Buck, M.; Grunze, M.; Eisert, F.; Fischer, J.; Träger, F. J. Vac. Sci. Technol. A 1992, 10, 926.

22 Hähner, G.; Wöll, C.; Buck, M.; Grunze, M. Langmuir 1993, 9, 1955.

23 Karpovich, D. S.; Blanchard, G. J. Langmuir 1994, 10, 3315.

24 Yokoyama, T.; Yokoyama, S.; Kamikado, T.; Okuno, Y.; Mashiko, S. Nature 2001, 413, 619.

25 a) Spillmann, H.; Kiebele, A.; Stöhr, M.; Jung, T. A.; Bonifazi, D.; Cheng, F.; Diedereich, F. Adv. Mater. 2006, 18, 275; b) Nath, K. G.; Ivasenko, O.; Miwa, J. A.; Dang, H.; Wuest, J. D.; Nanci, A.; Perepichika, D. F.; Rosei, F. J. Amer. Chem. Soc. 2006, 128, 4212; c) Wan, L.-J. Accounts of chemical research 2006, 39, 334.

26 Wandlowski, T. in "Fundamentals of Nanoelectronics", Lectures of the 34th IFF Spring School; Jülich, 2003.

27 "Teaching course from center for research in electrochemical science and technology", university of Cambridge.

http://www.cheng.cam.ac.uk/research/groups/electrochem/JAVA/electrochemistry/ELEC/l1html/intro01.html

28 Pronkin, S.; Wandlowski, T. J. Electroanal. Chem. 2003, 131, 550.

29 Wierzbinski, E.; Slowinski, K. Langmuir 2006, 22, 5205.

30 McCreery, R. L. Chem. Mater. 2004, 16, 4477.

31 Reed, M. A.; Zhou, C.; Muller, C. J.; Burgin, T. P.; Tour, J. M. Science 1997, 278, 252.

32 Van Ruitenbeek, J. M.; Alvarez, A.; Pineyro, I.; Grahmann, C.; Joyez, P.; Devorat, H. M.; Esteve, D.; Urbina, C. Rev. Sci. Instrum. 1996, 67, 108.

33 Gonzalez, M. T.; Wu, S.; Huber, R.; van der Molen, S. J.; Schönenberger, C.; Calame, M. Nano Lett. 2006, 6, 2238.

34 a) Xu, B.; Tao, N. J. Science 2003, 301, 1221; b) Tao, N. J. in "Molecules: Building Blocks for Future Nanoelectronics", Lectures of 5th International Wilhelm and Else Heraeus summer school; Wittenberg, 2004.

35 Slowinski, K.; Majda, M. J. Electroanal. Chem. 2000, 491, 139.

36 Nazin, G. V.; Qiu, X. H.; Ho, W. Science, 2003, 302, 77.

37 Ishizuka, K.; Suzuki, M.; Fujii, S.; Akiba, U.; Takayama, Y.; Sato, F.; Fujihira, M. Jpn. J. Appl. Phys. 2005, 44, 5382.

38 Cui, X. D.; Primak, A.; Zarate, X.; Lindsay, S. M. Science 2001, 294, 571.

39 Mujica, V.; Roitberg, A. E.; Ratner, M. A. J. Phys. Chem. 2000, 112, 6834.

 F. List of References

40 Mujica, V.; Ratner, M. A. Chem. Phys. 2001, 264, 365.

41 Gittins, D. I.; Bethell, D.; Schiffrin, D. J.; Nichols, R. J. Nature 2000, 408, 67.

42 Schmickler, W. Interfacial Electrochemistry; University Press: Oxford, 1996.

43 Scholz, F. Electroanalytical methods; Springer, 2002.

44 Finklea, H. O. Electroanal. Chem. 1996, *19*, 109.

45 Bard, A. J.; Faulkner, L. R. Electrochemical Methods: Fundamentals and Applications, 2 Ed.; John Wiley & Sons: New York, 2001.

46 Grahame, D. C. Chem. Revs. 1947, 41, 441.

47 Reinmuth, W. H. Anal. Chem. 1960, 32, 1509.

48 Qingmin Xu. Ph D thesis in Chinese academy of science, 2002, China.

49 Meyer, E.; Hug, H. J.; Bennewitz, R. Scanning Probe Microscopy, Springer, 2004.

50 http://w3.rz-berlin.mpg.de/ppb/info/mit/

51 Dretschkow, Th.; Wandlowski, Th. Topics Appl. Phys. 2003, 85, 259.

52 Nagy, G.; Wandlowski, Th. Langmuir 2003, 19, 10271.

53 Bonnell, D. A. Scanning Tunneling Microscopy and Spectroscopy: Theory, Techniques, and Applications. Wiley: New York, 2001.

54 Tao, N. J. Phys. Rev. Lett. 1996, 76, 4066.

55 Crommie, M. F.; Lutz, C. P.; Eigler, D. M. Science 1993, 262, 218.

56 Kolb, D. M. Electrochim. Acta 2000, 45, 2387.

57 Wandlowski, T.; Ataka, K.; Pronkin, S.; Diesing, D. Electrochim. Acta, 2004, 49, 1233.

58 Han, B. talk in the institute seminar of IBN, Research Center Juelich, 2003.

59 Osawa, M. Bull. Chem. Soc. Jpn. 1997, 70, 2861.

60 Han, B.; Li, Z.; Pronkin, S.; Wandlowski, Th. Can. J. Chem. 2004, 82, 1481.

61 Nagy, G. The preparation procedure for STM experiment in our lab.

62 Schultze, D.; Electrochim. Acta. 1977, 22, 117.

63 Ren, B.; Picardi, G.; Pettiger, B. Rev. Sci. Instrum. 2004, 75, 827.

64 Nagahara, L. A.; Thundat, T.; Lindsay, S. M. Rev. Sci. Instrum. 1989, 60, 3128.

65 Haiss, W.; van Zalinge, H.; Higgins, S. J.; Bethell, D.; Hörbenreich, H.; Schiffrin, D. J.; Nichols, R. J. J. Am. Chem. Soc. 2003, 125, 15294.

66 Dmitriev, A.; Lin, N.; Weckesser, J.; Barth, J. V.; Kern, K. J. Phys. Chem. B 2002, 106, 6907.

67 Griessl, S.; Lackinger, M.; Edelwirth, M.; Hietschold, M.; Heckel, W. Single Mol. 2002, 3, 25.

68 Ishikawa, Y.; Ohira, A.; Sakata, M.; Hirayama, C.; Kunitake, M. Chem. Commun. 2002, 2652.

69 Su, G. J.; Zhang, H. M.; Wan, L. J.; Bai, C. L.; Wandlowski, Th. J. Phys. Chem. B 2004, 108, 1931.

70 Spillmann, H.; Dmitriev, A.; Lin, N.; Messina, P.; Barth, J. V.; Kern, K.; J. Am. Chem. Soc. 2003, 125, 10725.

71 Li, Z.; Han, B.; Wan, L. J.; Wandlowski, Th. Langmuir 2005, 21, 6915.

72 Wandlowski, Th. in Encyclopedia of Electrochemistry, Gileadi, E.; Urbakh, M., eds, Wiley, 2003, p. 383.

73 Kolb, D. M.; Schneider, J. Electrochim. Acta 1986, 31, 929.

74 Wu, S.; Lipkowski, J.; Magnussen, O. M.; Ocko, B. M.; Wandlowski, Th. J. Electroanal. Chem. 1998, 446, 67.

75 Lange´s Handbook of Chemistry, J. A. Dean, Ed., Mc Grow-Hill, New York, 1985.

76 Hölzle, M. H.; Wandlowski, Th.; Kolb, D. M. J. Electroanal. Chem. 1995, 394, 271.

77 Duchamp, D. J.; March, R. E. Acta Cryst. B 1969, 25, 5.

78 Lippel, P. H.; Wilson, R. J.; Miller, M. D.; Wöll, C.; Chiang, S. Phys. Rev. Lett. 1989, 62, 171.

79 Chiang, S. Chem. Rev. 1997, 97, 1083.

80 Sautet, P. Chem. Rev. 1997, 97, 1097.

81 Böhringer, M.; Morgenstern, K.; Schneider, W. D.; Berndt, R.; Mauri, F.; de Vita, A.; Car, R. Phys. Rev. Lett. 1999, 83, 324.

82 Yuan, H. J.; Lu, J.; Wan, L. J.; Bai, C. L. J. Phys. Chem. 2004, 108, 11251.

83 Barth, J. V.; Weckesser, J.; Trimarchi, G.; Vladimirova, M.; de Vita, A.; Cai, Ch.; Brune, H.; Günter, P.; Kern, K. J. Am. Chem. Soc. 2002, 124, 7991.

84 Herbstein, F. H. in Comprehensive Supramolecular Chemistry, Atwood, J.L.; MacNicol, D. D.; Vögtle, F.; Lehn, J.-M. Eds.; Pergamon, New York, 1, 1996, Vol.6, p.61.

85 Griessl, S. J.; Lackinger, M.; Janitzky, F.; Markert, Th.; Hietschold, M.; Heckel, W. Langmuir 2004, 20, 9403.

86 Desiraju, G. R. Angew. Chem. Int. Ed. 1995, 34, 2311.

 F. List of References

87 Sumetskii, M.; Kornyshev, A. A. Phys Rev. B 1993, 48, 17493.

88 Kanter, J. A.; Roelofsen, G. Acta Cryst. B 1976, 32, 3328.

89 Lei, S. L.; Wang, C.; Yin, S. X.; Wang, Xi. F.; Liu, H. W.; Wan, L. J.; Bai, C. L. J. Phys. Chem. 2001, 105, 10838.

90 De Feyter, S.; de Schryver, F. C. Chem. Soc. Rev. 2003, 32, 139.

91 Herbstein, F. H.; Marsh, R. E. Acta Cryst. B 1977, 33, 2358.

92 Chatterjee, S.; Pecliredi, V. R.; Ranganathan, A.; Rao, C. N. R. J. Mol. Structure 2000, 520, 107.

93 Dale, S. H.; Elsegood, M. R. J.; Richards, S. J. Chem. Commun. 2004, 1278.

94 Ermer, O.; Neudörfl, J. Chem Eur. J. 2001, 7, 4961.

95 Arenas, J. F.; Marcos, J. I. Spectrochim. Acta A 1979, 35, 355.

96 Gonzalez Sanchez, F. Spectrochim. Acta 1957, 12, 17.

97 Osawa, M. Bull. Chem. Soc. Jpn. 1997, 70, 2861.

98 Ikezawa, Y.; Sekiguchi, R.; Kitazume, T. Electrochim. Acta 2000, 46, 731.

99 Noda, H.; Wan, L. J.; Osawa, M. Phys. Chem. Chem. Phys. 2001, 3, 3336.

100 Noda, H.; Ataka, K.; Wan, L. J.; Osawa, M. Surf. Sci. 1999, 427-428, 190.

101 Frederick, B. G.; Ashton, M. R.; Richardson, N. V. Surf. Sci. 1993, 292, 33.

102 Frederich, B. G.; Leibsle, F. M.; Haq, S.; Richardson, N. V. Surf. Sci. Lett. 1996, 3, 1523.

103 Casarin, M.; Granozzi, G.; Sambi, M.; Tondello, E. Surf. Sci. 1994, 307-309, 95.

104 Ortega-Lorenzo, M.; Baddeley, C. J.; Muryn, C.; Raval, R. Nature 2000, 204, 376.

105 Frederick, B. G.; Chen, Q.; Leibsle, F. M.; Lee, M. B.; Kitching, K. J.; Richards, N. V. Surf. Sci. 1997, 394, 1.

106 Meakin, P.; Cardy, J. L.; Loh, E.; Scalapino, D. J. J. Chem. Phys. 1987, 86, 2380.

107 De Feyter, S.; Gasquiere, A.; Klapper, M.; Müllen, K; de Schryver, F.C. Nano Lett. 2003, 3, 1485.

108 Kolotuchin, S. V.; Thiessen, P. A.; Fenton, E. E.; Wilson, S. R.; Loweth, C. J.; Zimmerman, S. C. Chem. Eur. J. 1999, 2537.

109 Meindel, J. D.; Chen, Q.; Davis, J. A. Science 2001, 293, 2044.

110 Joachim, C.; Gimzewski, J. K.; Aviram, A. Nature 2000, 408, 541.

111 Klein, D. L.; Roth, R.; Lim, A. K. L.; Alivisatos, A. P.; McEuen, P. L. Nature 1997, 389, 699.

112 Hu, J.; Odom, T. W.; Lieber, C. M. Acc. Chem. Res. 1999, 32, 435.

113 Aviram, A.; Ratner, M. Chem. Phys. Lett. 1974, 29, 277.

114 Metzger, R. J. Solid. State Chem. 2002, 168, 696; Acc. Chem. Res. 1999, 32, 950.

115 Molecular Electronics II, Aviram, A.; Ratner, M.; Mujica V. eds., Ann. N.Y. Acad. Sci., New York, 2002, p. 960.

116 Kergueris, C.; Bourgoin, J. P.; Palacin, S.; Esteve, D.; Urbina, C.; Magoga, M.; Joachim, C. Phys. Rev. B 1999, 59, 12505.

117 Reichert, J.; Ochs, R.; Beckmann, D.; Weber, H. B.; Mayor, M.; v. Löhneysen, H. Phys. Rev. Lett. 2002, 88, 176804.

118 Reichert, J.; Weber, H. B.; Mayor, M.; v. Löhneysen, H. Appl. Phys. Lett. 2003, 82, 4137.

119 Tran, E.; Rampi, M. A.; Whitesides, G. M.; Angew. Chem. Int. Ed. 2004, 43, 3835.

120 Donnhauser, Z.; Mantooth, B. A.; Kelley, K. F.; Bumm, L. A.; Monnell, J. D.; Stapleton, J. J.; Price, D. W.; Allara, D. L.; Tour, J. M.; Weis, P. S. Science 2001, 292, 2303.

121 Lemay, S. G.; Jansen, J. W.; van der Hout, M.; Mooij, M.; Bronikowski, M.; Willis, P. A.; Smalley, R. E.; Kouwenhoven, L. P.; Dekker, C. Nature 2001, 412, 6847.

122 a) Scudiero, L.; Barlow, D. E.; Hipps, K. W. J. Phys. Chem. B 2000, 104, 11899; b)

Scudiero, L.; Barlow, D. E.; Hipps, K. W. J. Am. Chem. Soc. 2001, 123, 4073; c)

Scudiero, L.; Barlow, D. E.; Hipps, K. W. J. Phys. Chem. B 2002, 106, 996.

123 Zhang, J.; Chi, Q.; Kuznetsov, A. M.; Hansen, A. G.; Wackerbarth, H.; Christensen, H. E. M.; Andersen, J. E. T.; Ulstrup, J. J. Phys. Chem. B 2002, 106, 1131.

124 a) Wold, D. J.; Frisbie, C. D. J. Am. Chem. Soc. 2001, 123, 5549; b) Wold, D. J.; Haag, R.; Rampi, M. A.; Frisbie, C. D. J. Phys. Chem. B 2002, 106, 2813.

125 Cui, X. D.; Zarate, X.; Tomfohr, J.; Sankey, O. F.; Primak, A.; Moore, A. L.; Moore, T. A.; Gust, D.; Harris, G.; Lindsay, S. M. Nanotechnology 2002, 13, 5.

126 Fan, F. R.; Yang, J.; Cai, L.; Price, D. W.; Dirk, S. M.; Kosynkin, D. V.; Yao, Y.; Rawlett, A. M.; Tour, J. M.; Bard, A. J. J. Am. Chem. Soc. 2002, 124, 5550.

127 Lu, X.; Hipps, K. W.; Wang, X. D.; Mazur, U. J. Am. Chem. Soc. 1996, 118, 7197.

128 (a) Haiss, W.; Nichols, R. J.; van Zalinge, H.; Higgins, S. J.; Bethell, D.; Schiffrin, D. J. Phys. Chem. Chem. Phys. 2004, 6, 4330; (b) Haiss, W.; van Zalinge, H.; Hoerbenreich, H.; Bethell, D.; Schiffrin, D. J.; Higgins, S. J.; Nichols, R. J. Langmuir, 2004, 20, 7694.

134 **F. List of References**

129 Chen, F.; He, J.; Nuckolls, C.; Roberts, T.; Klare, J. E.; Lindsay, S. Nano Lett. 2005, 5, 503.

130 Bird, C. L.; Kuhn, A. T. Chem. Soc. Rev. 1981, 10, 49.

131 Monk, P. M. S. The Viologens, John Wiley & Sons, Chichester, 1998.

132 De Long, H. C.; Buttry, D. A. Langmuir 1990, 6, 1319; 1992, 8, 2491.

133 Hiley, S. L.; Buttry, D. A. Colloids and Interfaces A 1994, 84, 129.

134 Li, J.; Chen, G.; Dong, S. Thin Solid Films 1997, 293, 200.

135 John, S. A.; Ohsaka, T. J. Electroanal. Chem. 1999, 477, 52.

136 Sagara, T.; Kaba, N.; Komatsu, M.; Uchida, M.; Nakashima, N. Electrochim. Acta 1998, 43, 2183.

137 Sagara, T.; Tsuruta, H.; Nakashima, N. J. Electroanal. Chem. 2001, 500, 255.

138 Sagara, T.; Maeda, H.; Yuan, Y.; Nakashima, N. Langmuir 1999, 15, 3823.

139 Alvarado, R. J.; Mukherjee, J.; Pacsial, E. J.; Alexander, D.; Raymo, F. M. J. Phys. Chem. B 2005, 109, 6164.

140 Raymo, F. M.; Alvarado, R. J.; Pacsial, E. J. J. Supramol. Chem. 2002, 2, 63.

141 Bard, A. J.; Faulkner, L. Electrochemical Methods, Wiley, New York, 1980.

142 Poirier, G. E. Langmuir 1997, 13, 2019.

143 Böhringer, M.; Morgenstern, K.; Schneider, W. D.; Berndt, R.; Mauri, F.; de Vita, A.; Car, R. Phys. Rev. Lett. 1999, 83, 324.

144 Li, Z.; Han, B.; Meszaros, G.; Pobelov, I.; Wandlowski, Th.; Błaszczyk, A.; Mayor, M. Faraday Discuss. 2006, 131, 121.

145 Poirier, G. E. Langmuir 1999, 15, 1167.

146 Staub, R.; Toerker, M.; Fritz, T.; Schmitz-Hübsch, T.; Sellam, F.; Leo, K. Langmuir 1998, 14, 6693.

147 Leung, T. Y. B.; Gerstenberg, M. C.; Lavrich, D. J.; Scoles, G.; Schreiber, F.; Poirier, G. E. Langmuir 2000, 16, 549.

148 Smith, D. P. E.; Hörber, J. K. H.; Binnig, G.; Nejoh, H. Nature 1990, 344, 641.

149 Dretschkow, Th.; Wandlowski, Th. Top. Appl. Phys. 2003, 85, 259.

150 De Feyter, S.; van Esch, J. H.; Ferringa, B. L.; de Schryver, F. C. Chem. Eur. J. 2004, 10, 1124.

151 Li. Z.; Pobelov, I.; Han B.; Wandlowski, Th.; Błaszczyk, A.; Mayor, M. Nanotechnology 2007, 18, 044018.

152 Marchenko, A.; Lukyanets, S.; Cousty, J. Phys. Rev. B 2002, 65, 45414.

153 Evan, S. D.; Urankar, E.; Ulman A.; Ferris, N. J. Am. Chem. Soc. 1991, 113, 4121.

154 Li, X.; He, J.; Hihath, J.; Xu, B.; Lindsay, S. M.; Tao, N. J. J. Am. Chem. Soc. 2006, 128, 2135.

155 Hester, R. E.; Suzuki, S. J. Phys. Chem. 1982, 86, 4626.

156 Pobelov, I.; Li, Z.; Wandlowski, Th. Octanedithiols paper, 2007, in preparation.

157 Fujihira, M.; Suzuki, M.; Fujii, S.; Nishikawa, A. Phys. Chem. Chem. Phys. 2006, 8, 3876.

158 Nitzan, A. Ann. Rev. Phys. Chem. 2001, 52, 681.

159 Salomon, A.; Cahen, D.; Lindsay, S. M.; Tomfohr, J.; Engelkes, V. B.; Frisbie, C. D. Adv. Mat. 2003, 15, 1881.

160 Marcus, R. A. J. Chem. Phys. 1956, 24, 979.

161 Gerischer, H. Z. Phys. Chem. NF 1960, 26, 223.

162 Newns, D. M. Phys. Rev. 1969, 178, 1123.

163 Kuznetsov, A. M.; Ulstrup, J. Electrochim. Acta 2000, 45, 2339.

164 Schmickler, W.; Tao, N. J. Electrochim. Acta 1997, 42, 2809.

165 Kuznetsov, A. M.; Ulstrup, J. J. Phys. Chem. 2000, 104, 11531; Probe Microscopy 2001, 2, 187.

166 Albrecht, T.; Guckian, A.; Ulstrup, J.; Vos, J. G. Nano Lett. 2005, 5, 1451.

167 Albrecht, T.; Moth-Poulsen, K.; Christensen, J. B.; Guckian, A.; Bjørnholm, Th.; Vos, J. G.; Ulstrup, J. Faraday Discuss. 2006, 131, 265.

Schriften des Forschungszentrums Jülich
Reihe Informationstechnik / Information Technology

1. **SAM - Untersuchung von Aushandlungen in Gruppen mittels Agentensimulation**
   von N. Lepperhoff (2002), VI, 278 Seiten
   ISBN: 978-3-89336-298-1

2. **Praxisbezogene IDL-Programmierung**
   von M. Busch, R. Bauer, H. Heer, M. Wagener (2002), XVI, 216 Seiten, 12 farb. Abb.
   ISBN: 978-3-89336-308-7

3. **Segmentierung von Volumendatensätzen mittels dreidimensionaler hierarchischer Inselstrukturen**
   von J.-F. Vogelbruch (2002), V, 191 Seiten, zahlr. farb. Abb.
   ISBN: 978-3-89336-309-4

4. **ComputerMathematik mit Maple**
   von J. Grotendorst (2003), VI, 274 Seiten mit beiliegender CD-ROM, zahlr. farb. Abb.
   ISBN: 978-3-89336-325-4

5. **ComputerMathematik mit Maple – Zweite überarbeitete und erweiterte Auflage**
   von J. Grotendorst (2004), VI, 294 Seiten mit beiliegender CD-ROM, zahlr. farb. Abb.
   ISBN: 978-3-89336-354-4

6. **The Internet in Germany: Atlas of Providers and Regions**
   by N. Lepperhoff, W. Fischer (2004), VIII, 103 pages, many coloured fig.
   ISBN: 978-3-89336-358-2

7. **Störstellen in Galliumnitrid-basierenden Transistoren**
   von M.J. Wolter (2004), V, 132 Seiten, 19 farb. Abb.
   ISBN: 978-3-89336-361-2

8. **Programming in C++: Audio-Visual Lecture of the course "Object-oriented programming in C++"**
   von B. Mohr, M. Boltes, R. Koschmieder (2004), DVD (18 hours, 22 minutes recorded in 15 sessions)
   ISBN: 978-3-89336-369-8

9. **Fabrication and characterization of planar Gunn diodes for Monolithic Microwave Integrated Circuits**
   by S. Montanari (2005), c. 150 pages, 26 col. fig.
   ISBN: 978-3-89336-396-4

10. **IDL Referenz der ICG-Daten-Struktur**
    von R. Bauer (2006), XIV, 130 Seiten
    ISBN: 978-3-89336-426-8

11. **Piezoresponse Force Microscopy and Surface Effects of Perovskite Ferroelectric Nanostructures**
    by F. Peter (2006), 106 pages
    ISBN: 978-3-89336-444-2

12. **Molecular Electronic Building Blocks Based on Self-Assembled Monolayers**
    by B. Lüssem (2006), 138 pages
    ISBN: 978-3-89336-454-1

13. **Josephson Tunnel Junctions with Ferromagnetic Interlayer**
    by M. Weides (2007), IX, 144 pages
    ISBN: 978-3-89336-472-5

14. **www.InfrastrukturInternet-Cyberterror.Netzwerk**
    Analyse und Simulation strategischer Angriffe auf die kritische Infrastruktur Internet
    von W. Fischer (2007), 213 Seiten
    ISBN: 978-3-89336-474-9

15. **Integration von Nanostrukturen durch alternative Methoden:**
    Mizellen-Deposition, Template-Wachstum und Nanogaps
    von S. Kronholz (2007), IX, 164 Seiten
    ISBN: 978-3-89336-478-7

16. **Self-assembly and Local Functionality at Au/Electrolyte Interfaces:**
    An in situ Scanning Tunneling Microscopy Approach
    by Z. Li (2007), VIII, 135 pages
    ISBN: 978-3-89336-482-4

As the miniaturization of electronic components approaches the nanometer scale, new concepts to tailor structure and functionality, as well as new fabrication strategies are essential to overcome the fundamental physical and economic limitations of conventional inorganic silicon technology. Bottom-up (self-)assembly of well-defined nanoscale building blocks, such as molecules, represents an attractive alternative.

In this dissertation, in situ scanning tunneling microscopy and spectroscopy are combined with cyclic voltammetry and ATR-SEIRAS to investigate the two-dimensional assembly and substrate-adsorbate coordination of aromatic carboxylic acids. In addition, structural and electron transfer properties of redox-active viologens at electrified gold/electrolyte interfaces are studied in detail.

Zhihai Li prepared for his PhD in the group of Dr. Thomas Wandlowski at the Research Center Jülich in Germany since February 2003, and concluded this work in February 2007. The contents of this book have been submitted to RWTH Aachen University in partial fulfillment of the requirements for the degree of Doctor of Philosophy.

Forschungszentrum Jülich
in der Helmholtz-Gemeinschaft

Band/Volume 16
ISBN 978-3-89336-482-4

Informationstechnik
Information Technology